Wayne State University Dissertations

8-1-2015

Dynamics Of Anisotropic Gold Nanopartilces In Synthetic And Biopolymer Solutions

Sharmine Alam
Wayne State University,

DYNAMICS OF ANISOTROPIC GOLD NANOPARTICLES IN SYNTHETIC AND BIOPOLYMER SOLUTIONS

by

SHARMINE ALAM

DISSERTATION

Submitted to the Graduate School

of Wayne State University

Detroit, Michigan

in partial fulfillment of the requirements

for the degree of

DOCTOR OF PHILOSHOPY

2015

MAJOR: PHYSICS

Approved by:

_____
Advisor   Date

_____

_____

_____

DEDICATION

To my parents and my brother, whose support motivated me to continue my academic and professional goals.

TABLE OF CONTENTS

LIST OF FIGURES

LIST OF TABLES

CHAPTER 1

INTRODUCTION

1.1 SOFT MATTER

Soft condensed matter or soft matter is a subfield of condensed matter physics consists of matter that are neither simple liquids nor crystalline solids. Many materials that are used in everyday life are soft matters such as - glues, paints, soaps, rubber etc. Variety of food we consume for example milk, mayonnaise, ketchup etc., can also be classified as soft matter. Human body primarily consists of soft materials such as blood, nucleic acids, proteins and polysaccharides. Soft materials also include colloidal dispersions, polymer melts and solutions, amphiphiles and liquid crystals.[1,2] The common similarity for all soft matter is that they all have intermediate length scale between atomic sizes (> 0.1 nm) and macroscopic scales (< 10 μm) which is also known as mesoscopic dimensions. Even though soft materials are larger than atomic sizes they are still small enough to possess thermal fluctuations caused by Brownian motion.[2,3] Soft matter can self-assemble. Many complex structures arise spontaneously in soft matter systems due to the rich phase behavior caused by subtle balances of energy and entropy.[2] The size and connectivity of the molecules in soft materials lead to strikingly new rheological properties. The mechanical response to shear stress is different for solid and liquid materials. If shear is applied to solids, solids resist deformation. On the other hand, liquids flow under shear. Soft materials exhibit a combination of time-dependent elastic and viscous response which is termed as viscoelastic behavior. If shear is applied for short time scale the response of viscoelastic material will be elastic. If shear is applied for a longer time than relaxation time, τ, the corresponding response will be a viscous one. The characteristic time scale, τ, for a viscoelastic system depends on the material. An example of viscoelastic material is "silly putty" which is a rubbery polymer and exhibits both types of mechanical response.

A brief description of the major classes of soft matter is discussed below:

Colloidal dispersions are heterogeneous systems in which particles (dimensions < 10 μm) of solids or droplet of liquids are evenly dispersed in a continuous medium. Examples of colloids are paints, inks, mayonnaise, biological fluids such as blood and milk. Colloidal dispersions have large surface-to-volume ratio because of their small size which means that with this high area of interface associated with a substantial amount of interfacial energy. Instead of this large energy, colloidal dispersions are characterized by their stability, that prevent the particles to combine and form larger aggregates in order to reduce the interfacial energy. The Brownian motion for smaller colloidal particles is particularly important as the gravitational force is subsides with decreasing size. If the thermal fluctuations of the colloidal particles overcome the gravitational force, then colloids remains dispersed in liquid. If colloidal particles come into contact, they could stick together irreversibly and larger assemblies of particles will be formed. This process is known as aggregation. Aggregation can be avoided by changing the forces acting between particles, which are normally attractive. By modifying the surfaces of colloidal particles, by exploiting electrostatic charge, or by attaching polymer chains to the particles it is possible to change the forces between them from attractive to repulsive.

Liquid crystals are soft materials that have degree of ordering intermediate between the molecular disorder of the liquid and the regular structure of a three dimensional crystal.[2] Unlike other soft materials liquid crystals have long-range orientational order which is possible if the molecules are anisotropic in shape such as rod-like or disc-like. The individual molecules that comprise a liquid crystal are commonly referred to as mesogen. Even for small temperature changes liquid crystals typically undergo multiple phase transitions. The most disordered liquid crystalline phase is the nematic phase. In nematic phase the molecules do not have any positional

order but they are oriented about a particular direction, called the director. Different nematic phases can occur in a system where the system is composed of chiral molecules, in which the molecule differs from its own mirror image. In these systems the neighbouring molecules have a slight tendency to align at a slight angle to one another, which leads the director to form a helix in space. These nematic phases are known as chiral nematics or more commonly cholesterics. The more ordered liquid crystal phase is known as smectic phase in which the molecules have orientational order as well as long-range positional order in one dimension. Liquid crystal phases with two-dimensional positional order can be formed by disc-like molecules which is termed as columnar (or discotic) phase.

Surfactant molecules or amphiphiles are another category of soft materials which have hydrophobic and hydrophilic components. If these molecules are immersed in liquids, they arrange themselves to form higher order structures such as micelles, which may be spherical or cylindrical in shape, bilayers or vesicles. These ordered structures allow the hydrophilic ends contact with the surrounding aqueous solution, while simultaneously limiting the interaction of the solution with the hydrophobic tails. Amphiphiles are relatively smaller molecules, but long polymer can also display the same behavior if they are composed of two or more chemically different blocks covalently attached together. Examples of amphiphiles include soaps and synthetic detergents which have a single hydrocarbon chain. Another very important category of amphiphiles have two hydrocarbon chains attached to its hydrophilic head groups, known as phospholipids. The phospholipids are major components of biological membranes. Different classes of soft matter are presented in Fig 1.1.1:
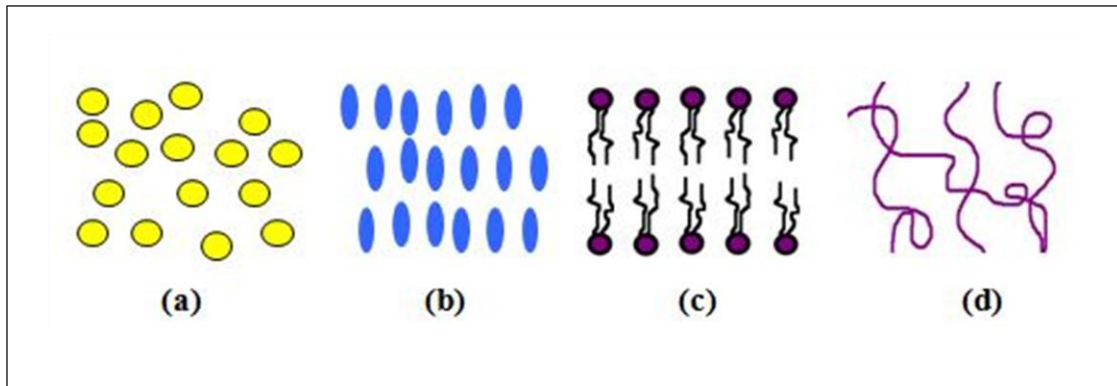
FIGURE 1.1.1: (a) colloidal particles, (b) liquid crystal, (c) amphiphiles, (d) polymer.

My research focus in soft matter is mainly on polymeric systems, which will be discussed below in detail.

1.2 POLYMERS

"Poly" means many and "mer" means part. Polymers are giant molecules made up of many small, simple repeating chemical units known as monomers. Monomers are connected to each other by covalent bonds and can be arranged in a variety of different architecture. The process in which monomers are covalently bonded together to form polymer is known as polymerization. The number of monomers, N, is called the degree of polymerization. Polymer properties vary with their degree of polymerization, microstructure and architecture. Molecular weight, M_w, of a polymer is the product of the degree of polymerization, N, and mass of each monomer unit (M_{mon}).[4]

$$M_w = NM_{mon} \qquad\qquad 1.2.1$$

Polymers can be either synthetic or biological in origin. For example plastics such as polystyrene and polyethylene are synthetic polymers and protein, nucleic acid such as DNA and polysaccharides are biopolymers. Polymers have varieties of different properties that arise from the different chemistry that makes them up. They also have numerous universal physical

properties such as, all of them are long, string-like molecules. The most fascinating property of polymers is that two molecules of a polymer cannot cross each other, which in turn leads to the effect of entanglement that produces dramatic viscoelastic effects in polymer melts and solutions.[2]

Depending on the arrangement of monomers in polymer chain, polymers can have different architecture such as linear or branched. Linear polymers are completely characterized by the degree of polymerization N. Example of a synthetic linear polymer is high-density polyethylene. Branched polymers, which possess side chains along with the main chain can be both synthetic and natural. One example of a branched polymer is low density polyethylene which contains many branches. A macroscopic volume network can be created if more and more branch points are introduced to a polymer system. Such networks include vulcanized rubber and cured epoxy resins.[2] Polymers can be classified as linear, ring, star-branched, H-branched, ladder, comb, dendrimer, randomly branched etc. (Fig. 1.2.1), depending on the arrangement of monomers in polymer chain. Dendrimers are three-dimensional polymer structures, which branch outwards from a common center; hence, the density of monomer units increases when moving closer to the center of the dendrimer.
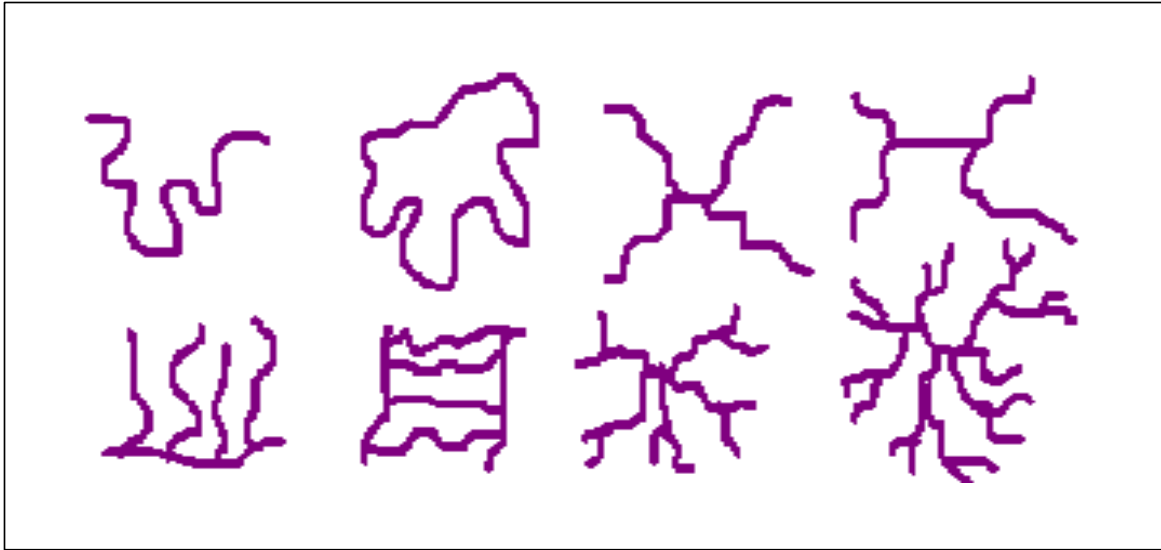
FIGURE 1.2.1: Examples of polymer architectures: linear, ring, star-branched, H-branched, comb, ladder, dendrimer, and randomely-branched.

Polymer microstructure, which is determined by the organization of monomers along the fixed chain plays important role in polymer's physical and chemical properties. Depending on the different type of monomers in a polymer, polymer can be classified as homo and heteropolymers. Homopolymers contain only one type of monomer while heteropolymers have more than one type of monomers. Copolymer is a heteropolymer, which has two different repeat units and they can exhibit different microstructures based on the sequence of monomers, including: block, random, alternating and graft copolymer (Fig. 1.2.2). If the two repeat units arranged in blocks, they are called block copolymers which can be diblock if they contain two blocks or triblock if they contain three blocks. Graft copolymers are produced by grafting chains on to the main backbone of polymer in which the side chain have different composition or configuration than the main chain. By grafting chains of polybutadiene on to a polystyrene backbone, a high-impact polystyrene (HIPS) can be produced in which the polystyrene gives the material strength, but the rubbery polybutadiene chains give it resilience to make it less brittle.

Sequenced copolymers are special class of copolymers in which synthesis of molecules produces only certain kind of arrangements that possesses specific properties and structure[2] such as DNA and proteins. Random polymers are opposite of sequenced copolymers where all arrangements of repeating unit are possible.
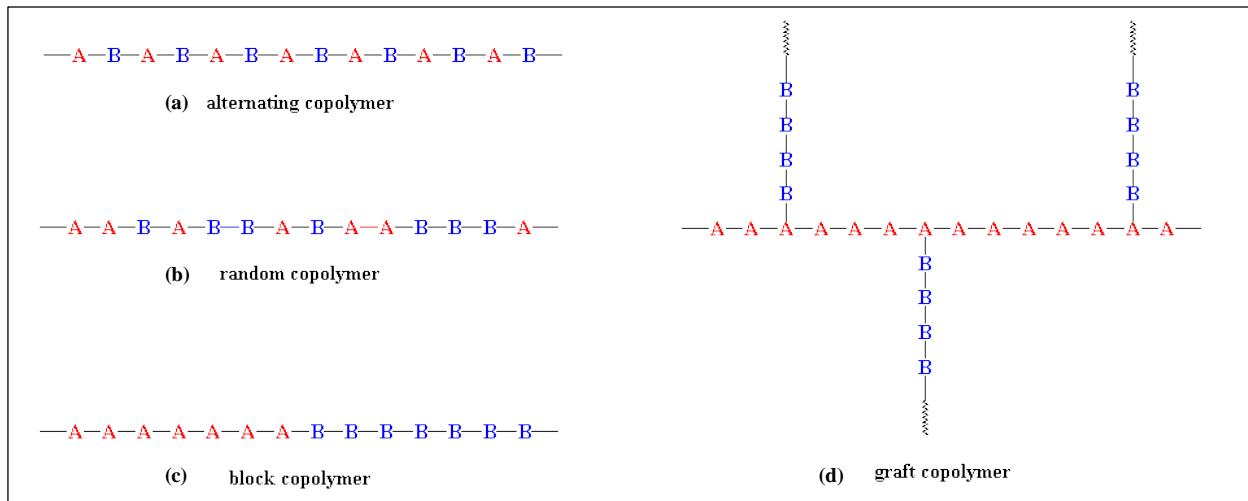
FIGURE 1.2.2: (a) alternating copolymer, (b) random copolymer, (c) block copolymer, and (d) graft copolymer.

Depending on the arrangements of atoms in a linear polymer chain, it can have different configurations. A given configuration can have different conformations. The conformations of polymer chain depends on the spatial structure of a polymer determined by the relative locations of its monomers in space that arise from the rotation of monomers about a single bonds. On the contrary, configuration of polymer is fixed by the chemical bonding of the molecule and it is necessary to break the chemical bond to achieve a different configuration of polymer. Some characteristics of polymer such as microstructure, architecture, degree of polymerization and chemical composition are fixed during polymerization. These characteristics of polymer cannot be changed without breaking covalent bonds. However, after polymerization, a polymer

molecule can adopt many different conformations, which depends on the orientation of monomers with respect to each other.

Conformation of polymer depends on the rotation about the bonds that make up the polymer backbone. For example, conformation of polymer chain can depends on the quality of the solvent in which it is dissolved. In dilute solution, the conformation of a polymer chains depends on the interaction between chain segments and solvent molecules.[3] Solvents can be divided in three categories: good, bad, and theta solvent. In good solvent, the solvent-monomer interaction is favored over the monomer-monomer interaction. Thus in good solvent, the polymer chain expands from its unperturbed (ideal) dimensions to maximize the number of polymer segment-solvent contacts and the polymer adopts a swollen coil conformation. In poor solvent the chain contracts to minimize interactions with solvent which means monomer-monomer interaction is favored in poor solvent. The polymer chains adopts a compact globule conformation in the presence of poor solvent. To counterbalance this effect the chain has a tendency to expand in order to reduce unfavorable segment-segment polymer interactions, which is known as excluded volume effect. The concept of excluded volume effect in polymer science refers that one part of a long polymer chain cannot occupy the space that is already occupied by another part of the same polymer chain. If these two effects are perfectly balanced then the polymer molecule will adopt unperturbed dimensions (random coil conformation) and this solvent is called theta solvent.[3]   Depending on the solvent, theta conditions are attained at the theta temperature as the solvent quality depends on temperature (higher temperature yield better quality).

According to Flory[4], the root mean square end-to-end distance of a chain in a good solvent is given by:

$$< r^2 >^{\frac{1}{2}} \sim N^\nu \qquad\qquad 1.2.2$$

where N is degree of polymerization and ν is an exponent known as Flory exponent. The value of ν = 3/5 for good solvent as the coil expanded compared to the Gaussian chain in good solvent. The exact value of Flory exponent, ν is actually 0.588 instead of 3/5 in good solvent. In theta solvent, for unperturbed chain ν = 1/2 and in case of poor solvent ν = 1/3. The value of Flory exponent in poor solvent implies that the attractive polymer-polymer interactions dominated the repulsive excluded volume effect and thus the chain collapses and forms a compact globule.[2] The solvent molecules can change the excluded volume for a polymer coil. The expansion factor, α, which is the ratio of perturbed and unperturbed dimensions has value α = 1 for theta or ideal solvent where the excluded volume is zero. In case of good solvent or Gaussian chain α > 1, whereas in a poor solvent α < 1.[3]

There are two types of polymeric liquids: polymer solutions and polymer melts. Polymer solutions can be obtained by dissolving polymer in solvent. Polymer melt is a bulk liquid state formed by macromolecules in the absence of a solvent, which means polymer melts are neat polymeric liquid above their glass transition and melting temperatures. Depending on concentration of polymer, polymer solutions can be divided into three classes: dilute, semidilute and concentrated solutions (Fig. 1.2.3). In polymer solutions, interaction between macromolecules strongly depends on concentration. In dilute solutions, the molecules are well separated and there is no significant interaction between them. Thus each molecule in a dilute solution can be considered as isolated chain. However, as the concentration is increased and reaches a particular concentration, the coils start to overlap. This concentration is termed as overlap concentration, c^*, where the coils are just in contact. The alternative measurement of concentration, c (g/ml) is volume fraction, ϕ (percentage by volume, vol%), where ϕ = 1 in the

absence of solvent. The overlap volume fraction, ϕ^*, is the ratio of the occupied volume of the polymer in the solution to the volume of the solution. The solution is called dilute below overlap volume fraction ($\phi < \phi^*$) and semidilute above overlap volume fraction ($\phi > \phi^*$). The properties of dilute solution are similar to pure solvent with slight modification due to the presence of polymer as the average distance between chains in dilute solutions is larger than their size. However, in semidilute solution presence of polymer controls most of the physical properties such as viscosity[4] as the polymer coils overlap in this regime.

$$\phi < \phi^*$$
(a) Dilute polymer solutions

$$\phi = \phi^*$$
(b) Overlap concentration

$$\phi^* < \phi < \phi^e$$
(c) Semidilute polymer solutions
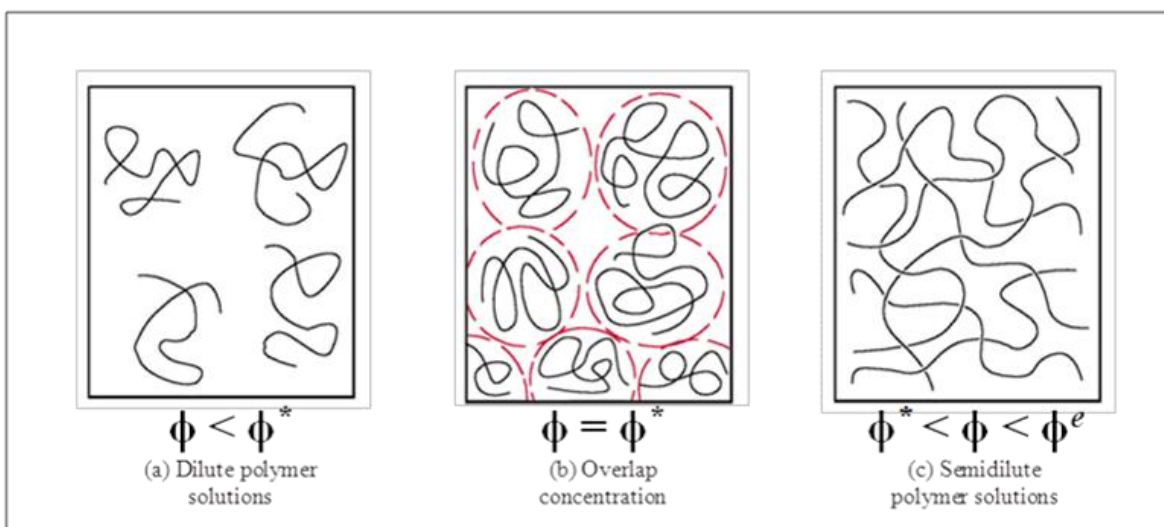
FIGURE 1.2.3: Different concentration regimes of flexible polymers.

The correlation length, ξ, is one of the most important concepts in semidilute solutions, which is the average distance between monomers on one chain to the nearest monomer on another chain. Entanglement concentration, c^e (corresponding entanglement volume fraction, ϕ^e) is an important crossover concentration for polymer solutions. At significantly higher concentration than ϕ^e, there is a strong overlap with neighboring chains, which lead to entanglement that greatly slows down the motion of polymers. A scaling representation of different concentration regions of polymer solutions is presented in Fig. 1.2.4:
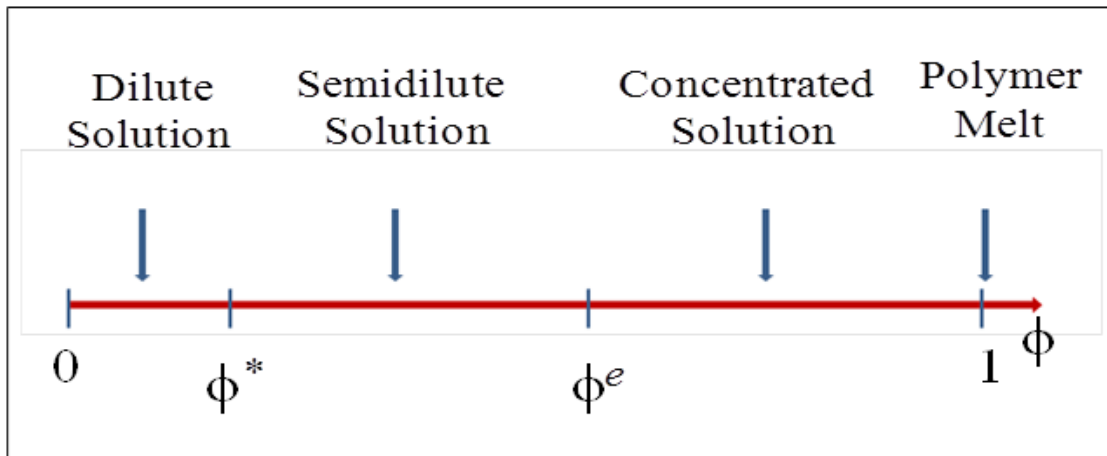
FIGURE 1.2.4: Different concentration regions of polymeric solution.

My research work is focused on studying polymer solution and colloidal particle mixture using anisotropic gold nanorods. In simple liquids, the translational diffusion coefficient, D_T of isolated spherical particles is given by the well known Stock-Einestein (SE) relation:

$$D_T = \frac{k_B T}{6\pi\eta R_o} \qquad 1.2.3$$

where k_B is Boltzmann constant, T is absolute temperature, η is solvent viscosity, R_o is the radius of the spherical particles. The rotational diffusion coefficient, D_R of spherical particle can be given by Einstein–Smoluchowski relation:

$$D_R = \frac{k_B T}{8\pi\eta R_o^3} \qquad 1.2.4$$

where $8\pi\eta R_o^3$ is the rotational frictional drag coefficient for a sphere of radius R_o. SE prediction is applicable for large particles in a solvent of much smaller molecules that acts as a continuum. Thus there are only two length scales involved in SE relation: size of probe particles and size of solvent molecules. In ternary mixtures, where, polymer, solvent, and probe particles are present, various length scales are involved depending on polymer concentration, size of probe particles, and polymer radius of gyration. The applicability of these relations become complicated in this situation.

Many biopolymers and macromolecules have anisotropic shape and their hydrodynamic properties such as translational and rotational dynamics depend on their shape. For anisotropic rod, both translational and rotational diffusion coefficients depend on their size (length, L and diameter, d) as well as aspect ratio (AR) which is the ratio of length to diameter of rod (L/d). There are three theoretical models to study translational and rotational diffusion coefficients of rod: hydrodynamic stick theory (HS theory),[5] Tirado and Garcia de la Torre's relations (TT theory)[6-8] and Broersma's relations.[9,10] The theories predict the following translational diffusion coefficients D_T:

Stick Theory:

$$D_T = (D_\parallel + 2D_\perp)/3 = \frac{k_B T}{3\pi\eta L} \ln\left(L/d\right) \qquad 1.2.5$$

where, $D_\parallel = \frac{k_B T}{2\pi\eta L} \ln\left(L/d\right), \quad D_\perp = \frac{k_B T}{4\pi\eta L} \ln\left(L/d\right)$

Tirado and Garcia de la Torre:

$$D_T = \frac{k_B T}{3\pi\eta L}\left[\ln\left(L/d\right) + \nu\right] \qquad 1.2.6$$

where, $\nu = 0.312 + 0.565\frac{d}{L} - 0.1\frac{d^2}{L^2}$

Broersma's Relations:

$$D_T = \frac{k_B T}{3\pi\eta L}\left[\ln(\delta) - \left(1/2\right)(\gamma_\parallel + \gamma_\perp)\right] \qquad 1.2.7$$

where, $\delta = \ln\left(2L/d\right),$

$\gamma_\parallel = 0.807 + 0.15/\delta + 13.5/\delta^2 - 37/\delta^3 + 22/\delta^4$

and $\gamma_\perp = -0.193 + 0.15/\delta + 8.1/\delta^2 - 18/\delta^3 + 9/\delta^4$

The theoretical predictions for the rotational diffusion constant by these three theories are as follows:

Stick Theory:

$$D_R = \frac{3}{2}\kappa[(2\kappa^2 - 1)S - \kappa]\frac{D_S}{(\kappa^4 - 1)} \tag{1.2.8}$$

where, $\kappa = \frac{L}{d}$, $S = (\kappa^2 - 1)^{-1/2}\ln[\kappa + (\kappa^2 - 1)^{1/2}$

$D_S = \frac{k_B T}{6V\eta}$ and $V = \left(\frac{4}{3}\right)\pi L\left(\frac{d}{2}\right)^2$

Tirado and Garcia de la Torre:

$$D_R = \frac{3k_B T}{\pi \eta L^3}\left[\ln\left(\frac{L}{d}\right) + \sigma\right] \tag{1.2.9}$$

where, $= -0.662 + 0.917\frac{d}{L} - 0.05\frac{d^2}{L^2}$

Broersma's Relations:

$$D_R = \frac{3k_B T}{\pi \eta L^3}(\delta - \xi) \tag{1.2.10}$$

where, $\delta = \ln\left(\frac{2L}{d}\right)$ and $= 1.14 + \frac{0.2}{\delta} + \frac{16}{\delta^2} - \frac{63}{\delta^3} + \frac{62}{\delta^4}$

TT theory and HS theory are valid for all aspect ratios of rods, whereas Broersma's relation is appropriate for long rods of aspect ratios > 3.5. TT theory that takes into account a rod-like shape instead of a prolate ellipsoid is more appropriate for our investigations which contains gold nanorods with aspect ratio ~ 3.5.

1.3 SIGNIFICANCE OF RESEARCH

Investigation of transport properties of metallic nanoparticles in synthetic and biopolymer is relevant for many interdisciplinary fields such as material sciences and nanobioengineering. Gold nanorods, specifically, have received a great deal of attention due to their unusual photophysical properties and their potential application in microelectronics and biomedical fields, such as sensing, imaging, delivery agents for drug and genes and localized hyperthermia. For instance, gold nanorods can be aligned into arrays in polymer film which can be used as optical filters, making them potential candidates for liquid crystalline displays (LCDs).

Gold nanorods are excellent candidates for biological sensing because the absorbance band of gold nanorods changes with the refractive index of local medium,[11] which is useful for extremely accurate sensing. In addition, plasmon-resonant gold nanorods are highly effective at transducing NIR light into heat and are promising for the selective thermal destruction of cancerous tissues based on localized hyperthermia.[12,13] So, it is important to study their dynamics in physiological environments as well as their interaction and conjugation with cytoplasmic fluids. Polymer solutions can imitate such crowded system and provide useful information about dynamics of anisotropic particles in complex fluids and biological systems. Effects of gold nanorods on cell viability via killing cancer cells is shown in Fig 1.3.1:
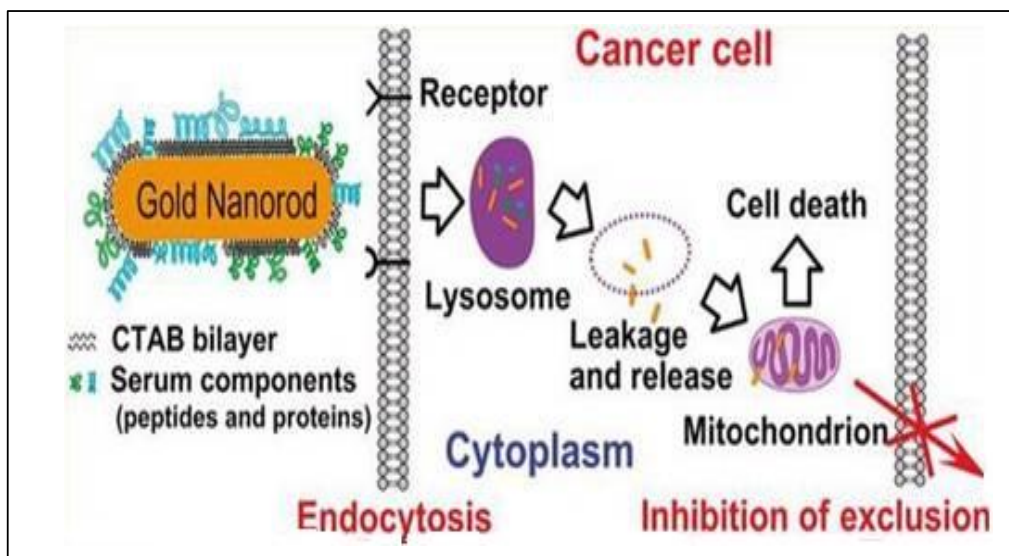
FIGURE 1.3.1: Trafficking of AuNRs in cancer cells.[14]

In this thesis we have investigated three important topics related to dynamics of nanoparticles in soft matter systems. First, investigation deals with how different length scales of a polymer solution affect the dynamics of anisotropic nanoparticles. Conjugation and interaction of anisotropic nanoparticles at the surface of biopolymers like proteins will be the second component of this thesis. The final section of this thesis involves the study of the effect of caging

on translational and rotational dynamics of anisotropic nanoparticles. Here, attention will be paid to solutions of rod/sphere mixture.

This dissertation is organized as follows. Chapter 2 will provide background information relevant to the thesis with some previous work pertinent to the projects. Chapter 3 outlines the experimental techniques used in the research projects. Specifically fluorescence correlation spectroscopy (FCS) employed to measure translational and rotational diffusion coefficient of anisotropic gold nanorods is described. Chapter 4-6 include the experimental results of my research. Particularly, the Chapter 4 covers the investigation of the effects of different polymer lengths on the translational and rotational diffusion of anisotropic nanoparticles in semidilute and entangled polymer solutions. Chapter 5 covers the conjugation and interaction of gold nanorods in protein solutions and Chapter 6 focuses on the translational and rotational diffusion of nanorods within a rod/sphere mixture. Chapter 7 will comprise the research project performed in collaboration with my colleague Dr. Kohli and will provide a glimpse of my future plans.

CHAPTER 2

BACKGROUND

2.1 INTRODUCTION

The investigation of nanoparticle dynamics in complex polymeric fluids such as polymer solutions and melts is important in several interdisciplinary fields. For example, these studies are important in soft matter physics and nanotechnology for proper interpretation of microrheology[15] experiments and development of novel composite systems that contain nanosized inclusions.[16] A lot of theoretical, experimental and computational studies have been done so far on probe diffusion in synthetic polymer. The following sections 2.1.1, 2.1.2 and 2.1.3 of this chapter will cover the theoretical, experimental and computational studies most relevant to this research and will provide necessary background in Chapter 4.

2.1.1 PREVIOUS THEORETICAL WORK

Theoretical studies developed so far considered mostly spherical particles. Cai *et al.*[17] described that probe diffusion in polymeric systems can be divided in two classes. The first class of theories was based on hydrodynamic interaction between particles and polymers[18], while the second class considered the polymer solutions as 'porous' system and the theory was based on the concept of 'obstruction effect'.[19-21]

With hydrodynamic theory in dilute polymer solutions with probe size $2R_o$ greater than the polymer chain size $2R_g$ (R_g is the radius of gyration), the chains are considered as 'hard spheres'. These 'hard spheres' have size equal to their hydrodynamic radii and the diffusing probes experience hydrodynamic interaction with these effective hard spheres in dilute polymer solutions. Within semidilute polymer solutions, the polymers are modeled as fixed friction centers of monomer beads[18] and due to this fixed monomer beads the hydrodynamic drag

experienced by the probe is screened at a length scale of the order of correlation length. In hydrodynamic theory the relaxation of polymer matrix is not considered. According to this theory the dependence of diffusion coefficient on probe size and polymer concentration obey a stretched exponential relation.

In the case of 'obstruction effect' theory, it was considered that the diffusion coefficient of probe particles will be linearly proportional to the fraction of relatively larger 'pores'. The 'pore size' is characterized by a distribution of distances from an arbitrary point in the system to the nearest polymer. For higher polymer concentration, probe particles could no longer diffuse through 'pores' created by overlapped polymer. Depending on the concentration of solutions, polymer can exhibit different 'pore size' as they are flexible and coil shaped. Also, if the particle size is larger than the correlation length (obstacles) then the particles are not permanently hindered by obstacles as the polymer dynamics affects the spacing between the obstacles.

Brochard and de Gennes[22] developed the scaling theory for probe diffusion in polymer solutions. They considered the concentrated polymer solution as a transient statistical network of mesh size, ξ (correlation length). The viscosity experienced by the probes follow a scaling form. They proposed that, if the probe size $R_0 < \xi$ the probe easily slip through the polymer mesh and only feels the solvent viscosity. In the opposite limit, i.e., if the probe size $R_0 >> \xi$ the particle should experience full solution viscosity or macroviscosity, which means that ξ can be considered as crossover length for the viscosity experienced by the probe particles. Many theoretical studies were done on the functional form for viscosity dependence on probe size and concentration of polymer solutions.[18,22-24]

To describe the dynamics of rigid probe particles, Phillies[23] demonstrated a hydrodynamic model. In this model the concentration dependence of diffusion coefficient is fitted to a stretched exponential relation, known as Phillies equation:

$$\frac{D}{D_0} = \exp\left(-\beta\phi^\nu\right)$$ 2.1.1

where D_0 is the diffusion coefficient in pure solvent, ν is a scaling parameter and β is a function of the probe size R_0. It was observed experimentally that for a wide range of polymer molecular weight $\beta \sim M_w^1$ and $\nu \sim M_w^{-1/4}$. Phillies generalized a simple scaling equation for the probes in polymer solutions as:

$$\frac{D}{D_0} = \exp\left(-ac^\nu M_w^\gamma R_o^\delta\right)$$ 2.1.2

where M_w is molecular weight of polymer and ν, γ, δ are scaling coefficients. Theoretically, $\gamma = 0$ and $\delta = 1$ for probe diffusion in open-coil polymer solutions, but these values are substantially inconsistent with experimental findings $\gamma = 0.8 \pm 0.1$, $\delta = 0.2$. The experimental value of $\nu = 0.5 - 1.0$. If the probe size (R_o) is of the same order of the correlation length ξ, the diffusion will be dominated by the fluctuation of the mesh size and according to scaling analysis the diffusion coefficient can be written as follows:

$$\frac{D}{D_0} = \exp\left(-\mu\left(\frac{R_o}{\xi}\right)^\delta\right)$$ 2.1.3

where $\xi = R_g\left(\frac{\phi}{\phi^*}\right)^{-0.75}$ and if we assume that $\delta = 1$ as in the theory then the Eq. (2.1.3) can be written as a stretched exponential function of polymer concentration and the value $\nu = 0.75$. Stretched exponential relation considers that there is no significant change in the nature of polymer motion in dilute or semidilute concentration regime, which is contrary to the predictions of scaling models for polymer self diffusion. In dilute polymer solutions, the scaling theories predict that single chains diffuse as isolated hydrodynamic ellipsoids as the distance between

polymer chains is much larger compared to the polymer radius of gyration R_g. The polymer chains overlap in semidilute concentration. In this regime, polymer dynamics were assumed to be controlled by chain "reptation", which means polymer chains move parallel to their own backbones. Phillies model considered that the hydrodynamic interactions are the dominant chain-chain interactions and this model does not consider reptation of polymer. It was assumed in Phillies model that interaction between pair of polymer chains was unaffected by the presence of intervening polymers.

Cukier[18] suggested a hydrodynamic model for Brownian diffusion of probes in semidilute concentration regimes by considering the screening effect:

$$D = D_0 \exp\left(-\kappa R_o\right) \qquad\qquad 2.1.4$$

where, κ is the hydrodynamic screening length that depends on polymer concentration c (g/ml) and $\kappa \sim c^{1/2}$. All the theories based on hydrodynamic interactions show exponential (or stretched exponential) dependence of probe diffusion coefficient on concentration of polymer. A recent scaling theory developed by Cai *et al.*[17] suggested a power law dependence of diffusion coefficient by considering coupling between particle motion and polymer dynamics. This theory extended the scaling theory for particle mobility in polymer liquids (both solutions and melts) which was developed by the Brochard-Wyart and de Gennes.[22] They considered three different cases for particle diffusion in polymer solutions. The diffusion will vary depending on the particle diameter d, correlation length, ξ and the tube diameter, a, which represents the topological confining effect of entanglements on a chain.

(a) Small size particles: The particle size is considered as small when b < d < ξ, where b is the length of Kuhn segment and the relation between b and ξ is given by:

$$\xi(\phi) \approx b\phi^{-\nu/(3\nu-1)} \qquad\qquad 2.1.5$$

where ν is the Flory exponent that depends on the solvent quality. Mobility of small particles does not affect strongly in the presence of polymer and their diffusion coefficient mainly depends on solvent viscosity, η_s:

$$D_S \approx \frac{k_B T}{\eta_s d} \qquad 2.1.6$$

$$\text{i.e. } D_S \propto d^{-1}$$

(b) Intermediate size particles: The particle size in the range ξ < d < a is defined as intermediate size and the motion of the particles in this size range is not affected by the entanglements of polymer chains, but is affected by the polymer dynamics. For intermediate size particles there are three regimes for the mean-square-displacement: at short time scale, $t < \tau_\xi$ the motion of such particles is diffusive and particles feel local solution viscosity comparable to the solvent. τ_ξ is known as the relaxation time of correlation blob with size ξ, and the expression for τ_ξ is given by:

$$\tau_\xi \approx \frac{\eta_s \xi^3}{k_B T} \qquad 2.1.7$$

At intermediate time scales, $\tau_\xi < t < \tau_d$, where τ_d is the relaxation time of a polymer section with size comparable to particle size, d the motion of the particles is subdiffusive. The effective diffusion coefficient of these particles decreases with time and can be written as:

$$D_{eff}(t) \approx \frac{k_B T}{\eta_{eff}(t) d} \qquad 2.1.8$$

where $\eta_{eff}(t)$ is the effective viscosity. The effective viscosity is the time dependent viscosity of a polymer solution that contains polymers of size equal to chain section size and this viscosity is higher than the solvent viscosity. The relation between effective viscosity and solvent viscosity is given by the following equation:

$$\eta_{eff}(t) \approx \eta_s \left(\frac{t}{\tau_\xi}\right)^{1/2} \qquad 2.1.9$$

At longer time scales, $t > \tau_d$ the motion of the intermediate size particles is diffusive. The effective viscosity felt by the particles is proportional to the number of correlated blobs in a chain section with size on the order of particle diameter and can be expressed as:

$$\eta_{eff} \approx \eta_s \left(\frac{d}{\xi}\right)^2 \qquad\qquad 2.1.10$$

The corresponding terminal diffusion coefficient can be written as:

$$D_t \approx \frac{k_B T}{\eta_{eff}(\tau_d)d} \approx \frac{k_B T \xi^2}{\eta_s d^3} \qquad\qquad 2.1.11$$

$$\text{i.e. } D_t \propto d^{-3}$$

(c) Large particles: The particles with size larger than entanglement length, $d > a$ are defined as large particles and the motion of such particles at time scales shorter than the relaxation time $t < \tau_e$ follows the same time-dependence as intermediate size particles. The relaxation time of an entanglement strand, τ_e is the time when the arrest of particle motion occurs:

$$\tau_e \approx \tau_\xi \left(\frac{a}{\xi}\right)^4 \qquad\qquad 2.1.12$$

The large particles are trapped by entanglements at time scale $t > \tau_e$ and in order to move further the probe particles have to wait for the polymer liquid to relax during reptation time τ_{rep}. The probe particles slightly larger than the tube diameter $d \geq a$ do not have to wait for the whole polymer liquid to relax. In this case, the particles can diffuse by hopping between neighboring entanglement cages.[25] The terminal diffusion coefficient of very large probe particles $d \gg a$ is determined by bulk viscosity, η of polymer liquids. At time scales shorter than τ_{rep}, large particles $d > a$ are trapped by entanglement and the diffusion coefficient for large probe particles due to chain reptation can be written as:

$$D_{rep} \approx \frac{k_B T}{\eta d} \qquad\qquad 2.1.13$$

$$\text{i.e. } D_{rep} \propto d^{-1}$$
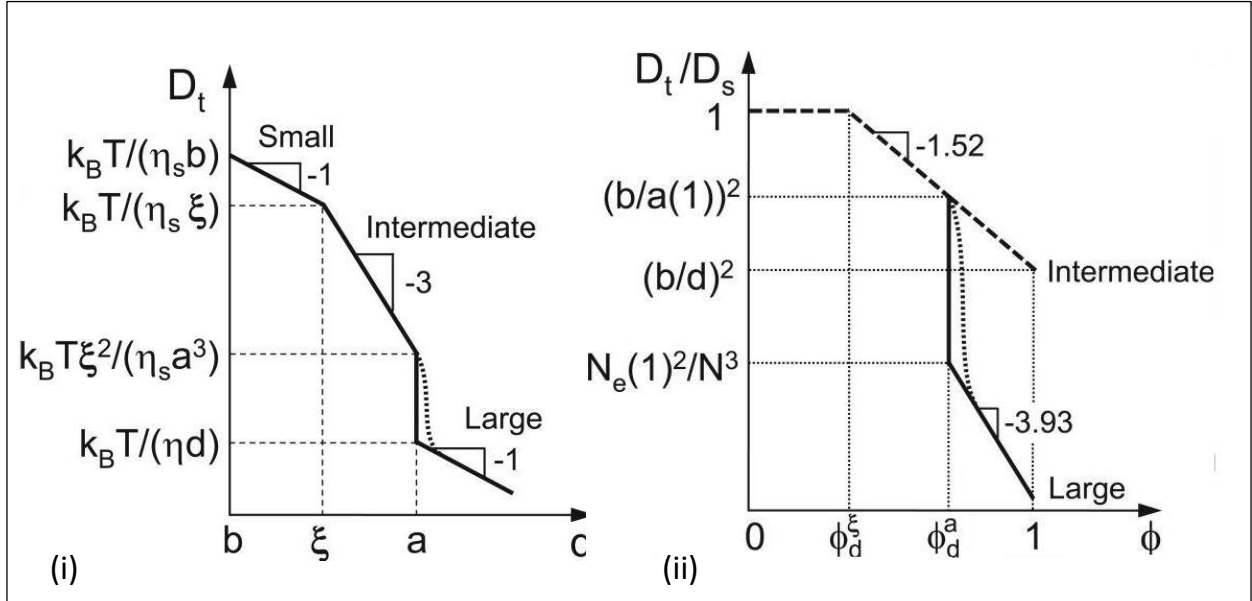
FIGURE 2.1.1: (i) Terminal particle diffusion coefficient D_t as a function of particles size d in entangled polymer solutions. (ii) Normalized terminal diffusion coefficient as a function of polymer concentration in entangled athermal polymer solutions.[17]

It is easier to vary concentration of polymer rather than size of particles systematically in many experiments. Correlation length, $\xi(\phi)$ and tube diameter $a(\phi)$ are two concentration-dependent length scales. Cai *et al.*[17] divided the concentration into three regimes by two cross-over solution concentrations ϕ_d^{ξ} and ϕ_d^a: I, II and III. If the volume fraction is below ϕ_d^{ξ} i.e. $\phi < \phi_d^{\xi}$ (II) the diffusion coefficient of particles is then concentration independent and is determined by the solvent viscosity, η_s. The probe particles feel segmental motions of polymer at volume fraction above ϕ_d^{ξ} (regime II). In this regime the diffusion coefficient of particles decreases with solution volume fraction as a power of -1.52 for athermal solvent (Fig. 2.1.1). In athermal solvent, Flory exponent, ν is independent of temperature and monomer-monomer contact is

energetically indistinguishable from monomer-solvent contact. For large size particles (d > a), the probe particles are expected to feel full solution viscosity above ϕ_d^a (regime III) . The terminal diffusion coefficient of probe particles in this regime decreases with solution volume fraction as power -3.93 for athermal solvent (Fig 2.1.1) .

2.1.2 COMPUTATIONAL STUDIES

Lui *et al.*[26] have used molecular dynamics (MD) simulations to investigate the diffusion of nanoparticles in polymer melts. The dependence of size, concentration, mass of probe particles, polymer chain length, and polymer-particle interaction on the diffusion of particles in polymer melts were studied. They observed that the radius of gyration of polymer chain is the most significant factor in determining the validity of Stokes-Einstein (SE) relation for particles diffusion. The SE relation can predict the diffusion correctly in polymer melts, when the particle size is larger than the radius of gyration of polymer chain. In contrast, when the particle size is smaller than the radius of gyration, the particle diffusion is related to nanoviscosity rather than macroviscosity. Furthermore, in this regime, particle diffusion is independent of the chain length or molecular weight of the polymer, but dependent on the particle mass. By increasing the chain length gradually, they have observed that the transition process of the particle experiencing macroviscosity to nanoviscosity.

Kremer *et al.*[27] had performed an extensive molecular dynamics (MD) simulation and reported that SE diffusion coefficient gradually approximates the MD data with the increase in R_o/R_g, and becomes same as the ratio approaches unity. Furthermore, for lower R_o/R_g, the SE prediction deviates from MD simulations and is an order magnitude lower than the simulations. They argued that macroviscosity of polymer is related to chain relaxation as small nanoparticles, do not necessarily have to wait for chain relaxation for diffusion. That is why small nanoparticles

experiences nanoviscosity rather than macroviscosity. As the ratio R_o/Rg increases with the increases of nanoparticles size, R_o, if the solvent behaved as a continuum on the length scale of chain size, R_g, which leads to the bigger particles to experience macroviscosity. They also investigated the dependence of diffusion coefficient on hydrodynamic radius of probe particles. In the regime $R_o/Rg < 1$, it was observed that the diffusion coefficient of nanoparticles decreases with the increase in particle's hydrodynamic radius as power of -3, which contradicts the SE prediction. They have suggested that for small probe particles, the friction between particle and polymer was caused by the monomer rubbing the probe particle surface. The friction due to this rubbing is proportional to particle surface, resulting in local viscosity scaling as R_o^2.

Ganesan *et al.*[28] proposed a continuum model for the dynamics of particles in polymer matrices. They presented analytical and computer simulation for the mobility of particles and the viscosity of suspension in case of unentangled polymer melts. For probe particles of size greater than the correlation length and smaller or comparable to the polymer radius of gyration, i.e., $\xi < R_o \leq R_g$, they suggested that the polymer radius of gyration, R_g is the length scale controlling the transition from nanoviscosity to macroviscosity. For smaller R_o/R_g, they claimed that the presence of polymer chain entanglements was not necessary to observe reduction in viscosity. However, the entangled polymer systems showed a much stronger effect on viscosity reduction.

2.1.3 PREVIOUS EXPERIMENTAL WORK

Along with the theoretical and computational studies, several experimental studies were done to understand the dynamics of particle in polymeric liquids, although most of the work was on spherical nanoparticles. Holyst *et al.*[29] performed experiments to investigate the dynamics of nanoscopic probes such as dye molecule and proteins of different diameters (from 1.7 to 114 nm) in different molecular weight polymers. They used capillary electrophoresis and fluorescence

correlation spectroscopy techniques. Using polyethylene glycol (PEG) with molecular weight ranging from 6 to 20 kg/mol they showed that for $R_o < R_g$, the probe particles experienced nanoviscosity which was an order of magnitude smaller than the macroviscosity of polymer solution. The nanoviscosity can be expressed as:

$$\frac{\eta_{nano}}{\eta_0} = \exp\left(b\left(\frac{R_o}{\xi}\right)^a\right) \qquad\qquad 2.1.14$$

where η_0 is the water viscosity, a and b are two constants close to unity. On the other hand, for $R_o > R_g$, macroviscosity experienced by the probe particles can be written as:

$$\frac{\eta_{macro}}{\eta_0} = exp\left(b\left(\frac{R_g}{\xi}\right)^a\right) \qquad\qquad 2.1.15$$

They concluded that the crossover length scale is polymer radius of gyration, R_g, as suggested by MD simulations rather than correlation length ξ of polymer blob size assumed by the theoretical prediction.

Ye *et al.*[30] reported deviation from SE relation while investigating the probe diffusion of small colloidal particles through a nonadsorbing polymer poly(ethylenepropylene) (PEP) solution. They conducted dynamic light scattering (DLS) and sedimentation experiments and argued that when the probe size was comparable to or smaller than the correlation length of the polymer solution, the particles experience a reduction of friction coefficient.

Kohli *et al.*[31] investigated the length scale dependency on dynamics of gold nanoparticles in poly(ethylene glycol) (PEG) solutions. They used fluctuation correlation spectroscopy to measure the diffusion coefficient of gold nanoparticles as a function of particles size, polymer volume fraction and molecular weight. They argued that for $R_o > R_g$, the diffusion coefficients obtained from experiments were similar to those expected from SE relation. However, for particles $R_o \leq R_g$, the diffusion is faster than the value estimated from SE relation. They concluded that the ratio D/D_{SE} increases with polymer concentration and as R_o/R_g becomes

smaller, where D_{SE} is the diffusion coefficient given by the Stokes-Einstein (SE) relation using stick boundary condition:

$$D_{SE} = \frac{k_B T}{6\pi\eta_0 R_o}$$ 2.1.16

For anisotropic particles, such as rods, the diffusion includes both translation and rotational motions. Translation occurs at longer time scale, while rotation of probe motion involves much faster time scale.[32] The combination of both dynamics can yield significant information about spatially varying global and local properties of the polymer matrix. The information will be helpful for understanding the dynamics of many viruses (e.g. tobacco mosaic virus) and biopolymers (e.g. segments of DNA, polypeptide) which can be model as short cylinders or rods.[7,33] This will be discussed further in Chapter 4.

2.2 PREVIOUS WORK ON BIOPOLYMERS

The information in this section is the background relevant to Chapter 5 and Chapter 7. Gold nanoparticles have diagnostic as well as therapeutic applications. For safe use of nanoparticles, it is important to understand how nanoparticles diffuse and interact with biomolecules in biological fluids.[34-36] For instance, recent studies have shown that nanoparticles commonly used for biological applications interact with blood plasma and can become coated with a number of biomolecules present in the medium.[37] These biomolecules shield the nanoparticles by forming a protein 'corona', which in turns screens their original properties.[38]

Gold nanorods (AuNRs), which have large absorption cross section in near-infrared (NIR) are being widely used for drug delivery and localized hyperthermia for cancer therapeutics.[39] Nanorods have the ability to absorb lights of different wavelength due to surface plasmon resonance (SPR). The intensity and wavelength of SPR can be highly shape and size dependent.[40,41] Gold nanorods display two separate SPR bands which correspond to their width

and aspect ratio due to their shape anisotropy. The two SPR bands are known as transverse (TSPR) and longitudinal surface plasmon resonance (LSPR) bands. The position of TSPR is just above 500 nm while the LSPR varies according to the nanorod's aspect ratio. NIR has deeper penetration ability through tissues compared to the visible light, which can be exploited for in vivo imaging. AuNRs are usually synthesized in the presence cetyltrimethylammonium bromide (CTAB), which is used as the structure guiding agent as well as capping agent. CTAB binds strongly on the surface of nanorods and complete removal of CTAB leads to aggregation of AuNRs. The properties of AuNRs can alter if the CTAB structure around the rod is disturbed, and this could alter the penetration ability of AuNRs through tisues as well as interaction with cytoplasmic fluids and can induce toxicity. Thus, it is important to have better understanding of AuNRs and protein interaction/conjugation to scrutinize the biocompatibility of AuNRs for safe applications.

There are a large number of different proteins, among them serum albumin is the most abundant protein in blood which is responsible for about 80% of the colloidal osmotic pressure.[42,43] Albumin acts as a carrier for fatty acids in the circulatory system[44] as well as responsible for regulating the blood pH.[45] Bovine serum albumin (BSA) has structural/functional similarity to human serum albumin (HSA) – almost 76% sequence homology.[46] BSA is the most extensively used serum protein because of its similarities with HSA as well as low cost and wide availability. Furthermore, BSA has nearly identical pH-dependent conformational transitions as HAS.[47] BSA is a water-soluble protein with isoelectric point at 4.6 and its native (N) state is found in the pH range from 4.5 to 8. The N state of BSA can be approximated as an equilateral triangular prism with sides 8 nm and height 3 nm.[48] In aqueous solution, the structure and behavior of BSA are dominated by multiple interactions, including electrostatic, hydrophobic,

hydrogen bonding, and van der Waals. Detailed information about adsorption and conformation of BSA onto Au nanoparticles are important for biological applications of Au nanoparticles. Also, after binding to Au nanoparticles BSA can undergo structural changes, which may affect its function and bioactivity as well as the reactivity, stability and transport properties of BSA-gold nanoparticle conjugate.

Rocker *et al.*[49] analyzed the adsorption of human serum albumin (HSA) on polymer-coated FePt and CdSe/ZnS nanoparticles (10-20 nm in diameter) and quantum dots by using fluorescence correlation spectroscopy (FCS). They concluded that HSA formed a monolayer at the surface of carboxy-functionalized negatively charged nanoparticles. The adsorption of protein was confirmed by measuring the change in the particle radius $\Delta R = 3.3$ nm and by a quantitative analysis. They demonstrated that the binding occurred with micromolar affinity which can be best described by an anti-cooperative binding model.

Medina *et al.*[50] investigated the adsorption of bovine serum albumin (BSA) on citrate-stabilized gold nanospheres using scattering correlation spectroscopy. They analyzed nanoparticle and protein interaction quantitatively by observing the diffusion parameters before and after protein adsorption. The change in diffusion coefficient was due to increase in hydrodynamic radius of nanoparticles corresponds to BSA monolayer formation. They demonstrated that the monolayer formation is independent of AuNPs size and the BSA monolayer retains its native charge. Furthermore, they demonstrated that the protein adsorption does not cause aggregation of AuNPs.

Kohli *et al.*[51] studied the interaction of BSA with small sized (2.5-10 nm radius) tannic acid- stabilized gold nanoparticles. They monitored the change in Brownian diffusion of AuNPs by using fluorescence correlation spectroscopy (FCS) and concluded that the thickness of

adsorbed layer of BSA on AuNPs is independent of the NP size. They also concluded that adsorption is due to ligand exchange reaction between protein and AuNPs, rather than electrostatic attraction.

Chkakraborty *et al.*[52] reported the interaction of BSA with gold nanospheres and nanorods. They concluded that the binding of AuNPs and BSA is exothermic in nature, while it is uniquely endothermic for gold nanorods (AuNRs) and BSA. Additionally, the interaction of AuNRs and BSA is entropy driven which is caused by release of large amount of water from the hydrophobic region of CTAB coated AuNRs. They also observed that the AuNRs form large aggregates on interaction with BSA, which could have adverse effect in the cellular uptake.

Systemic study of interaction and conjugation of gold nanoparticles and BSA would have potential application ranging from biophysics to drug delivery. The discussion about BSA and gold nanorod conjugate will be described in Chapter 5 and the investigation of BSA-gold nanospheres interaction will be discussed in Chapter 7.

2.3 PREVIOUS WORK ON ROD/SPHERE MIXTURES

2.3.1 THEORETICAL WORK

Particle motion through complex fluids is important in many commercial and natural processess, ranging from the drying of paints and inks to transport in living cells. The probe diffusion method, where a particle (the probe) is followed as it moves through a suspension of other particles (matrix), targets such behavior at a fundamental level.[53-55] We have investigated a system, containing rods (probe) suspended in spherical colloidal particles (matrix). The rotational relaxation of rods in concentrated sphere suspensions is a subject of long-standing interest, both from theoretical and experimental point of view. The theoretical analysis is derived from a caging model for restricted rotational diffusion of rigid rods in an isotropic solution of

similar rods[56,57] given by Doi-Edwards. According to the theory for a rod/sphere mixture the rod will be trapped by neighboring spheres and the rotational motion of the rod will be limited to a space between rods and nearest spheres. The rotational diffusion coefficient, D_r^{sph} of a rod with length L and diameter d in a mixture of rod and sphere solution is given by:

$$D_r^{sph} \propto \frac{(\Delta\theta)^2}{t}$$

2.2.1

where t is the time required for a rod to displace in between the nearest spheres and during this time the rod rotation takes place with an angular displacement, $\Delta\theta$. The expressions for t and $\Delta\theta$ are given by:

$$t = \frac{L^2}{D_s}$$

2.2.2

$$\Delta\theta = \frac{\Delta s}{L} \propto \frac{n^{-1/3}}{L}$$

2.2.3

where n is the number concentration of spheres and caging of rod is valid in the range $1/_{L^3} < n < 2\pi/_{dL^2}$, D_s is the translational self-diffusion coefficient of a sphere, Δs is an arc-length through which a rod rotates. This arc-length is approximately proportional to the average distance between spheres and is proportional to $n^{-1/3}$. Equation (2.2.1) can be written as:

$$D_r^{sph} \propto \frac{D_s}{L^4 n^{2/3}}$$

2.2.4

By using Stokes law for dilute solutions D_s can be described as:

$$D_s \propto \frac{k_B T}{\eta_s R}$$

2.2.5

where η_s is the solvent viscosity and R is the radius of spheres. Combining Eq. 2.2.4 and Eq. 2.2..5 the diffusion coefficient can be expressed as:

$$D_r^{sph} \propto \frac{k_B T}{\eta_s L^4 R n^{2/3}}$$

2.2.6

For higher concentrations, self-diffusion coefficient of spheres D_s depends on the sphere concentration and is inversely proportional to the suspension viscosity $\eta(\phi)$. Finally, the

restricted rotational diffusion coefficient of a test rod in a finite concentration of spheres can be described as:

$$D_r^{sph} \propto \frac{k_B T}{\eta(\phi) L^4 R n^{2/3}}$$ 2.2.7

The above argument is acceptable with the following restrictions: (a) the rods and spheres should have comparable size L~ R, though the size of spheres must be somewhat smaller than the size of rods; (b) The concentration of spheres should be high enough for some caging to occur i.e. $2\pi > (Ln^{1/3})^{-1}$ but the concentration should not be so high that the spheres will overlap each other i.e. $(R^3 n) < 1$.

The original Doi-Edwards (DE) theory predicts that the rotational motion of rods will be severely restricted in semidilute regime. DE theory gives the following expression for the concentration dependence of rotational diffusion coefficient:

$$D_r/D_{r0} = \beta(nL^3)^{-2}$$ 2.2.8

where D_{r0} is the value of rotational diffusion coefficient in the infinite dilution limit and β is a numerical factor expected to be of the order of unity. However, experimental value of β falls in the range between 10^2 and 10^4, which is much larger than 1.

Odijik *et al.*[58,59] have proposed the most insightful explanation of the discrepancies in DE theory by arguing that the caging effect becomes important when the confinement angle is smaller than the bending of rod which depends on its flexibility.

Keep and Pecora[60] divided the concentration scale for rod/sphere mixture in several regimes: (a) $0 < nL^3 < 1$ is considered as dilute concentration, where short-range interaction between rod and sphere can be ignored; (b) $1 < nL^3 < 10$, where Enskog-type binary collision theories for diffusion are valid; (c) $10 < nL^3 < 50$ in this concentration range the rods are not

completely caged, the cages appears and disappears with time; (d) $50 < nL^3 < 500$, caging theories are reasonable in this concentration range and Doi-Edwards dependence valid for infinitely thin rigid rods.

2.3.2 COMPUTATIONAL STUDIES

Simulations have in general agreed with the concentration and length dependences in DE theory. However, to agree quantitatively with theory they had to postulate a value of β of order 1000. The "Brownian" simulation of Doi, Yamamoto and Kano[61] confirms the DE theory, and was in agreement with tube theory and experimental results, which used electric birefringence and dynamic light scattering. From the simulation, it was found that at high concentrations, D_r is proportional to n^{-2}, which is interpreted on the basis of modified DE cage model.[62] On the contrary, Fixman *et al.*[63] by using Brownian simulation of rods with variable diameter, d, showed that the rotational coefficient of friction as well as diffusion coefficient is the same in the limit d → 0. The simulations of rods obeying Newtonian dynamics by Frenkel and Maguire[64] also confirmed DE scaling of rotational friction constant. However, their model deviates from DE theory at high concentrations. The rod can move along its length as well as perpendicular to its length. Frankel and Maguir model consider the concentration range $1 < nL^3 < 48$, that yields a divergence of the longitudinal diffusion coefficient of rod $D_{\parallel}$ at high concentrations, which along with other effects of elastic collisions can limit the equilibration of Δθ, the magnitude of angular rotation of rod.

Odell, Atkins and Keller[65] used computer simulation to conclude that the caging of rods was not complete unless a significant concentration is reached, which is way above the DE prediction. According to them the diffusing rods were presented with an inhomogeneous maze of baffles and is not completely caged, there is always some route available for 180^0 rotation of rod.

2.3.3 EXPERIMENTAL STUDIES

The simulations and the theoretical work mainly focused on simple models, which are, however, not very realistic for describing the rod-sphere system. The complexity arises from many degrees of freedom and multiple types of interactions among rods and spheres. Experimental investigations of modified DE theory by electric birefringence[66,67] and depolarized light scattering[68] have demonstrated considerable discrepancies both in the mechanism involved in DE theory and the concentration of the caging.

Lellig *et al.*[69] used dynamic light scattering (DLS), fluorescence recovery after photobleaching (FRAP), and fluorescence correlation spectroscopy (FCS) methods to investigate the dynamics of rod-shaped tobacco mosaic virus (TMV) particles in a suspensions of highly charged colloidal spheres. FCS is sensitive to both translational and rotational motions, whereas both DLS and FRAP probes the diffusion at much larger length scales and only sensitive to translational motion. Their experimental data indicated a slowing down of the rotational motion of TMV rod with increasing structural order of the matrix spheres.

Cush *et al.*[33,70] used depolarized dynamic light scattering to measure translational and rotational diffusion of TMV within extended and globular polymer solutions. They concluded that the apparent translational and rotational diffusion rates decreased with increasing in polymer concentration. Furthermore, they observed that the rotation is much more restrained than expected, while translational diffusion is faster than expected.

Koenderink *et al.*[71] investigated the short-time rotational diffusion of colloidal silica tracer spheres in a suspension of rigid silica rods by using time-resolved phosphorescence anisotropy (TPA). The reduced short time rotational diffusion coefficient of charged tracer sphere was studied as a function of tracer radius, rod volume fraction and salt concentration.

They noticed that for a particular rod volume fraction, a larger tracer size and a small screening length appear to maximize hydrodynamic hindrance of tracer diffusion. Additionally, except for small tracer size and larger screening length, Stokes-Einstein-Debye (SED) scaling of the rotational diffusion coefficient as a function of inverse viscosity of the rod suspension matches well with experiments.

The most relevant experimental study related to our work was done by Phalakornkul *et al.*[72] They performed transient electric birefringence (TEB) decay to study the rotation of rod-like polymers in solutions with spherical particles. In addition, they studied the sphere collective diffusion coefficient as a function of sphere volume fraction. Furthermore, they measured the rotational relaxation rate of rods in a suspension of spherical particles using several different lengths of rod-like polymers. The experimental results indicated that in the suspension of longer rods, the rotational relaxation rate decreases rapidly with the increase in sphere concentration. Moreover, in the suspension where the rods are shorter than the average sphere diameter, the rate of rotation changes slightly compared to rotation rate of rods in the same solvent. From the experiment, they also concluded that the viscosity of the sphere suspensions is not inversely proportional to the rotational diffusion coefficient as predicted by DE theory.

In semidilute concentration, which is our main interest, various types of molecular interactions have to be taken into account. The interactions involved in this region includes: (a) steric repulsion and van der Waals attraction between rods and sphere, and (b) the hydrodynamic interaction. Thus, the investigation of dynamics of rods in mixture of spheres in systematic manner remains challenging. The discussion will be continued in Chapter 6.

CHAPTER 3

FLUORESCENCE CORRELATION SPECTROSCOPY

3.1 INTRODUCTION

Fluorescence correlation spectroscopy (FCS) is an experimental technique to measure the dynamics of molecular process by observing spontaneous temporal-fluctuations in molecular position and number density. The fluctuations of fluorescence in the system can be due to Brownian motion such as translational and rotational diffusion, externally induced flow, chemical reactions, conformational fluctuations of biomolecules or some other processes.[73-76] FCS was first introduced by Magde *et. al.* in 1972 to measure the diffusion and binding of ethidium bromide onto double-stranded DNA.[75] Thermally induced diffusion is one of the fundamental properties exhibited by molecules within the solutions and it is very important to measure diffusion coefficient precisely. The measurements of fluctuation in fluorescence intensity requires very small sample volumes, which were not feasible to achieve by other means such as dynamic light scattering (DLS), pulsed field gradient NMR, or size exclusion electrophoresis.[77-79] High sample concentrations were used in these studies which is far away from infinite dilution and all these devices suffered from poor signal to noise ratio. In contrast to the above techniques, the high sensitivity of FCS has been used to monitor diffusion, concentration, chemical biochemical interactions/reactions of fluorescent or fluorescently labeled molecules at nanomolar concentrations in solution. Some recent applications of FCS include investigation of biological systems, as the noninvasive nature of FCS allowed study of the living biological cells such as enzymatic reactions etc[76]. FCS monitors tiny fluctuations of fluorescence molecules (fluorophores) and provides single molecules sensitivity. The number of fluorescent molecules changes continuously as the molecules diffuse in and out of a laser focus that

maintains a constant volume. The autocorrelation function (ACF), G(τ) of fluctuation in fluorescence intensity, δF(t) ≡ F(t)−< $F(t)$ > is given by:

$$G(\tau) = \frac{<\delta F(t).\delta F(t+\tau)>}{<F(t)>^2}$$

3.1.1

where τ represents time lag, < > denotes a time-average and F(t) is the observed fluorescence intensity. To acquire normalized ACF, it has been divide by the square of the average intensity.
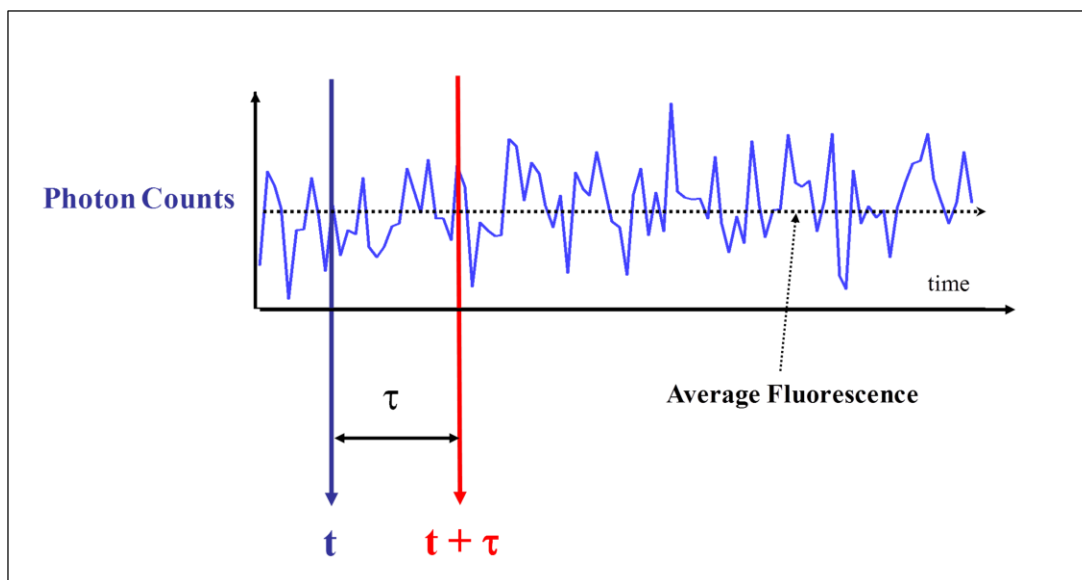
FIGURE 3.1.1: Fluctuation of fluorescence due to molecular motions and generation of autocorrelation function (ACF).

The ACF measures the self-similarity of a function with itself after a time lag (τ), which means autocorrelation measurements are sensitive only to signal variations within one channel (Fig. 3.1.1). On the contrary, in our experiments cross-correlation function (CCF) analysis was used, to compare the signals arising from two different channels, which is convenient to find common features in two independently measured signals. Cross-correlation functions arise due to temporally coordinated fluctuations in both channels (Fig. 3.1.2). The cross correlation function is defined as:

$$G_{ij}(\tau) = \frac{<\delta F_i(t).\delta F_j(t+\tau)>}{<F_i(t).F_j(t)>^2} \qquad 3.1.2$$

where i and j are two different measured signals of the fluorescent intensity.
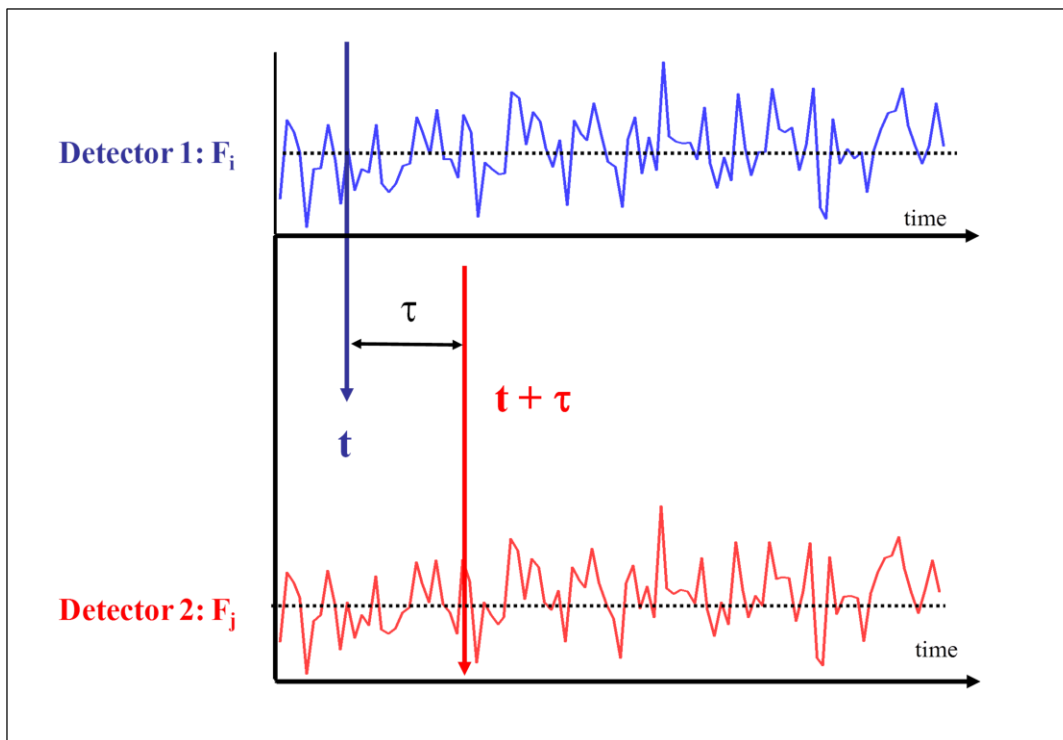
FIGURE 3.1.2: Fluctuation of fluorescence due to molecular motion and generation of cross-correlation function (CCF).

To obtain meaningful data from the ACF or CCF, they need to be fitted with a particular model.[73] The correlation functions provide information on the diffusion coefficient and fluorescent molecule concentration within the focal volume. 2D Gaussian, 3D Gaussian, and Gaussian-Lorentzian are three most common laser focus profiles used in FCS measurements. The dimensionality of the system under investigation, the nature of excitation, and the means by which the fluorophores move are required to consider, while developing the suitable model for the ACF. The model of autocorrelation curves for different kinds of particle motion is presented in Fig 3.1.3:
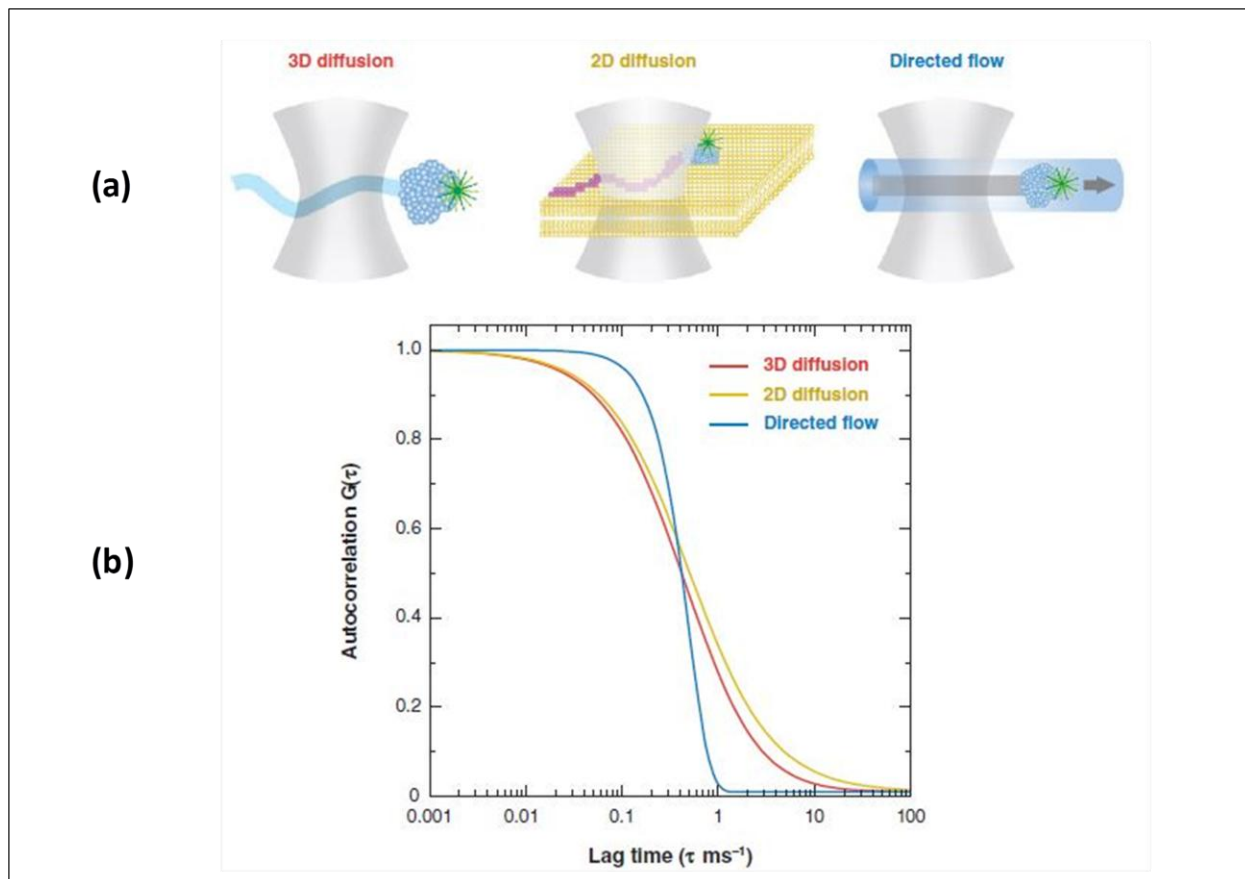
FIGURE 3.1.3: (a, b): Model autocorrelation curves for different kinds of particle motion: free diffusion in three dimensions (red), free diffusion in two dimensions, e.g., for membrane-bound molecules (yellow) and directed flow (Cyan).[80]

3.2 EXPERIMENTAL SET-UP FOR FCS:

All FCS setup measures the fluctuations of fluorophores, however depending on the experiments of interest construction of a particular set-up can vary. A laser, which is the main component of FCS set-up, provides necessary energy to excite the fluorophores. The laser source can either have continuous light (one-photon excitation) or pulsed light (two-photon excitation) source. A schematic diagram of an FCS setup utilizing two-photon excitation is presented in Fig. 3.2.1:
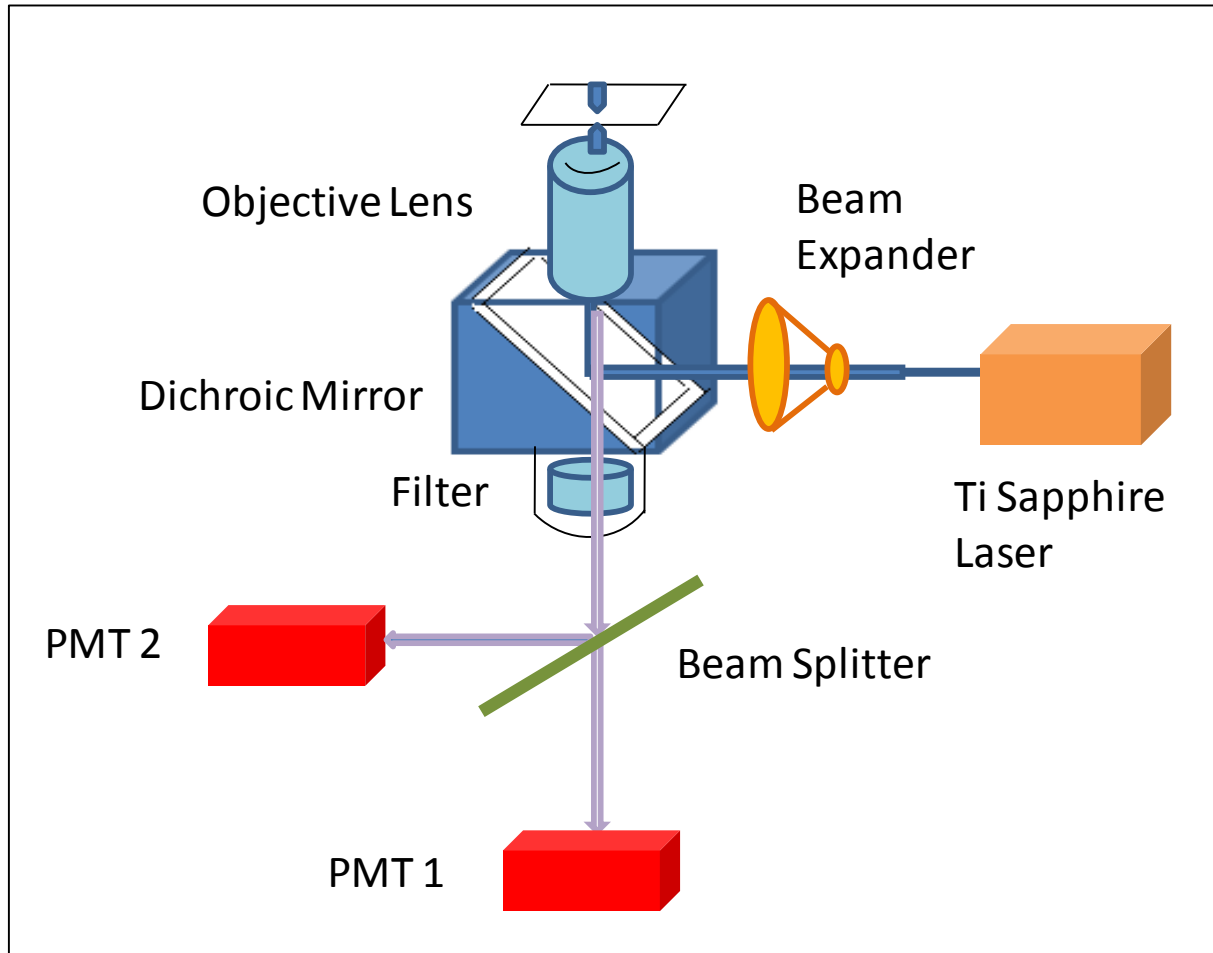
FIGURE 3.2.1: Two photon FCS set up for translational diffusion measurements.

In two-photon excitation the laser is pulsed at high frequency and the fluorophores within the excitation volume absorb two photons (Fig. 3.2.2). The absorption of two photon is a quasi-simultaneous (within 10^{-16} seconds) process and the excitation process requires the absorption of two photons with about double wavelength required for the actual transition.[81] The photon flux should be extremely high for such three particles event to happen. The probability of absorbing two photons per excitation is proportional to the square of the excitation energy and the light intensity decreases quadratically with the increase of distance from the focal plane.[73] The laser
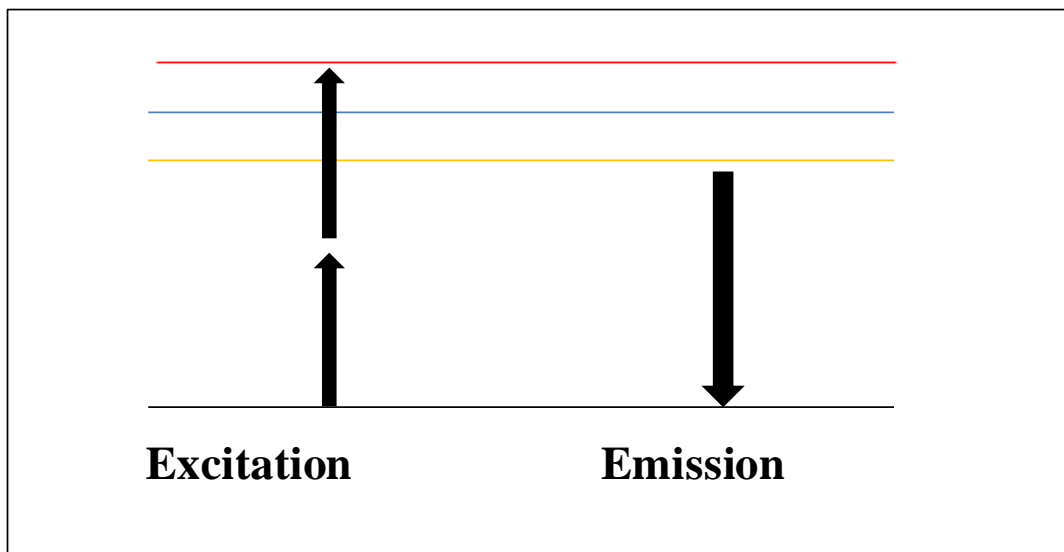
FIGURE 3.2.2: Diagram of two photon excitation.

excites a tiny volume in the immediate vicinity of the objective focal spot because of the above

two factors. Thus smaller excitation volume is attained without the use of pinholes in case of two

photon excitation. On the contrary, a one photon absorption set-up requires the introduction of a

pinhole at the image plane, which excites all fluorophores that lie within the double cone above

and below the focal spot. Thus two-photon excitation is more suitable for biological samples that

are relatively more sensitive to photo damage.[81]

The necessary energy to excite fluorophores is provided by an infrared femtosecond Ti-

sapphire laser (Mai Tai-Spectra physics) with 800 nm wavelength, 120 fs pulse width and 80

MHz repetition rate. A Zeiss inverted microscope (Axiovert S200TV, Carl Zeiss) served as the

operational platform for the experiment. After passing through a neutral density filter (NDF), to

adjust the power of the laser beam for specific experiment, the light is then passeed through a

beam expander. The beam expander, which consists of two achromatic lenses separated by a

distance equal to the sum of their focal lengths expands small laser beam (~ 2 mm). The laser

beam then reflects off a dichroic mirror, which is made of a special multilayer dielectric coating. The dichroic mirror reflects wavelength above a certain value (transition wavelength) and transmits under the same value. The transition wavelength should match with the fluorophores used in the experiment. The laser light is then collected by a high numerical aperture (N.A. = 1.25, 100x) objective. The objective excites a very small volume (~ 1 fL) inside the sample. If a fluorophore passes through the focal volume, it absorbs two photons and emits one photon. The emitted light follows the same route – first collected by the objective and then passes through the dichroic mirror. Finally, the fluorescent light is collected by a photomultiplier tube (PMT) detector, which has single photon sensitivity (Hamamatsu). A short pulse filter is introduced in between dichroic mirror and PMT to stop any leakage or scattered light from entering the PMT.

An integrated data acquisition system (ISS, IL) was used to record and analyze the fluctuations of fluorescent molecules in real time. The acquisition frequency can be controlled by a computer software. The software calculates and updates the autocorrelation function or cross-correlation function during the experiment. The ACF is then analyzed using suitable model to extract important information about the dynamics of the sample under investigation. The cross - correlation experiments involved two PMT's with single-photon sensitivity. To study nanosphere's dynamics, where only translational diffusion is involved, a beam splitter is placed between short pass filter and detectors. For anisotropic particles, rotational diffusion measurements require a polarized signal, which can arise from their shape anisotropy. In this case a polarized beam splitter is placed before the detectors to obtain polarization resolved signal.

3.3 FCS THEORY

FCS measures the fluctuations in the fluorescence emission to investigate the molecular dynamics. The light source is focused tightly onto the sample, which excites a small volume (~ femtoliter) in the solution. If the fluorescent molecules move into the focus volume, they absorb energy and emit fluorescent light, which is then collected by the PMT detector. The fluctuations in the fluorescence intensity, $\delta F(t)$ is given by,

$$\delta F(t) \equiv F(t) - < F(t) > \qquad 3.1.3$$

where F(t) is fluorescent intensity and <F(t)> is the average value of fluorescent intensity.

If only one fluorescent species is present then fluorescent intensity is given by the following equation in terms of the spatial profile of the excitation light E(r):

$$F(t) = kQ \int E(r)C(r,t)dr \qquad 3.1.4$$

where k is a constant, Q is a product of absorptivity, fluorescence quantum efficiency, and the detection efficiency of the optical system and C(r,t) is the dye concentration at position r and time t. Then the Eq. (3.1.3) can be written as:

$$\delta F(t) \equiv kQ \int E(r)\delta C(r,t)dr \qquad 3.1.5$$

where δC(r,t) is the change in fluorescent particle concentration and is given by,

$$\delta C(r,t) = C(r,t) - < C > \qquad 3.1.6$$

$$G(\tau) = \frac{<\delta F(t).\delta(F+\tau)>}{<F(t)>^2} \qquad 3.1.7$$

$$G(\tau) = \frac{\iint E(r)E(r')<\delta C(r,t).\delta C(r',t+\tau)>drdr\prime}{(<C>\int E(r)dr)^2} \qquad 3.1.8$$

The spatial intensity profile of the excitation light E(r) for the 3D Gaussian model with two-photon excitation is given by:

$$E(r) = E(x,y,z) = E_0 \exp\left(-\frac{4(x^2+y^2)}{\omega_0^2} - \frac{4z^2}{z_0^2}\right) \qquad 3.1.9$$

For Brownian diffusion the fluctuation of fluorescent concentration, δC(r,t) is related to the diffusion coefficient, D by Fick's second law:

$$\frac{\partial \delta C(r,t)}{\partial t} = D \nabla^2 \delta C(r,t) \qquad 3.1.10$$

The solution of above equation is given by:

$$\delta C(r,t) = \frac{<C>}{\sqrt{4\pi Dt}} \exp\left(-\frac{r^2}{4Dt}\right) \qquad 3.1.11$$

Assuming the sample is stationary, for translational diffusion in two dimensions the following

relation will be valid:

$$< \delta C(r,t).\delta C(r',t+\tau) > = \frac{<C>}{\sqrt{4\pi D\tau}} \exp\left(-\frac{(r-r')^2}{4D\tau}\right) \qquad 3.1.12$$

The translational diffusion coefficient of spherical particles is given by Stokes-Einstein equation:

$$D = \frac{k_B T}{6\pi \eta R_H} \qquad 3.1.13$$

where k_B is the Boltzmann constant, T is absolute temperature of the ambient, η is the viscosity

of the surrounding fluid and R_H is the hydrodynamic radius of the particle. The diffusion of the

particles as well as the average size for spherical particles can be determined by correlating the

change in concentration of particles through the sample volume. Substituting Eq. (3.1.12) in Eq.

(3.1.8):

$$G(\tau) = \left(\frac{2\sqrt{2}}{\pi\sqrt{\pi}\omega_0^2 z_0 <C>}\right) \frac{1}{\left(1+\frac{8D\tau}{\omega_0^2}\right)\sqrt{1+\frac{8D\tau}{z_0^2}}} = \frac{G(0)}{\left(1+\frac{8D\tau}{\omega_0^2}\right)\sqrt{1+\frac{8D\tau}{z_0^2}}} \qquad 3.1.14$$

where ω_0 is the beam waist, z_0 is the beam height, and the density of fluorescent particle is:

$$< C >= \frac{1}{2\sqrt{2}VG(0)} = \frac{2\sqrt{2}}{\pi\sqrt{\pi}\omega_0^2 z_0 G(0)} \qquad 3.1.15$$

and the excitation volume V is:

$$V = \frac{\pi\sqrt{\pi}\omega_0^2 z_0}{2^3} \qquad 3.1.16$$

The average number of molecules within the excitation volume is given by

$$< N >= V < C >= \frac{1}{2\sqrt{2}G(0)} \qquad 3.1.17$$

If both diffusion and flow V_f are present together, then for one species the autocorrelation function is given as below:

$$G(\tau) = \frac{G(0)}{\left(1+\frac{8D\tau}{\omega_0^2}\right)\sqrt{1+\frac{8D\tau}{z_0^2}}} \exp\left(\frac{-(V_{flow}(\tau))^3}{\omega_0^2 z_0\left(1+\frac{8D\tau}{\omega_0^2}\right)\sqrt{1+\frac{8D\tau}{z_0^2}}}\right) \qquad 3.1.18$$

CHAPTER 4

DYNAMICS OF ANISOTROPIC PARTTICLES IN SYNTHEIC POLYMER SOLUTIONS

4.1 TRANSLATIONAL AND ROTATIONAL DIFFUSIONS OF NANORODS WITHIN SEMIDILUTE AND ENTANGLED POLYMER SOLUTIONS

The following material was originally published in Macromolecules (2014).[82]

Understanding the diffusion of nanoparticles (NPs) in synthetic and biopolymer medium is important in fields as diverse as materials science[83,84] to nanobioengineering[85]. At the fundamental level, the research helps us to test various polymer theories and simulations, especially the effects of hydrodynamic forces, polymer segmental motion, and topological constraints on the NP transport properties.[17,86,87] From the application perspective, NPs are increasingly being used as drug and gene therapy vectors. The polymeric particles or liposomes have higher loading capacity, but they are of significantly larger in size (> 100 nm) and require labeling for visualization.[88] In contrast, intrinsically luminescent particles, such as quantum dots (QDs) or metallic NPs offer advantages of high photostability, brightness, and greater control over their size and shape at the length scale of 2-100 nm.[89] In addition, the use of smaller particles is advantageous in certain therapeutic applications, such as in many diseases, where the pore size of the physiological barrier that the particles must penetrate to reach their target is significantly reduced.[90]

We are interested in studying the Brownian motion of gold nanorods in synthetic polymer poly(ethylene) glycol (PEG) solutions. Gold nanoparticles (AuNPs) of size less than 40 nm were shown to transfect cells easily either through non-specific or receptor-mediated endocytosis.[91] Compared to gold nanospheres, gold nanorods (AuNRs) have the advantage that their localized surface plasmon resonance (LSPR) can be tuned by changing the aspect ratio

(length/diameter).[92-94] AuNRs having a moderate aspect ratio of ~3-4, which is used in this study, has LSPR at the near infrared (NIR) wavelength (λ~800 nm) as shown in Fig. 4.1.1. Because of deeper penetration ability of NIR through tissues compared to visible light, this opens up the possibility of *in vivo* imaging. But before many of the potentials of AuNRs could be realized, we need a better understanding of their interaction and transport through dense macromolecular network.
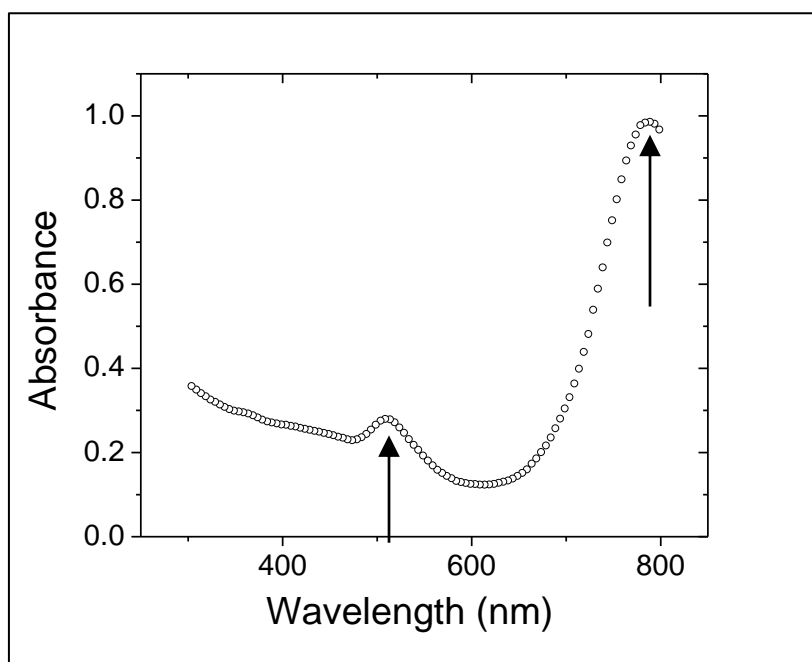
FIGURE 4.1.1: UV-vis spectra of AuNR in water (open circle) with two distinct peaks at 790 nm and 510 nm. The peak at 790 nm depends upon the aspect ratio of the rod.

For anisotropic objects, such as rods, the transport includes both translation and rotation. Translation involves probe motion at longer time scale, while rotation occurs at much faster time scale.[32] The combination of both can provide information about spatially varying global and local properties of the matrix. Moreover, many viruses (e.g, tobacco mosaic virus) and biopolymers, such as segments of DNA or polypeptide can be modeled as short cylinders.[7,33]

However, little is understood about their dynamics both theoretically and experimentally in macromolecular solutions.[95,96] The results presented here provide insight by using a model polymer system in conjunction with novel experimental technique with needed sensitivity as well as spatial and temporal resolution. We identified situations where the continuum hydrodynamic breaks down completely and instead microscopic friction solely determines the particle transport.

4.2 EXPERIMENTAL SECTION

We used a model polymer system, polyethylene glycol (PEG) prepared with different concentrations in deionized water. The advantage of this system is that the porosity of the network and the entanglement length scale can be tuned from a few nm to few tens of nm by changing the volume fraction of PEG (Table 4.3.1). PEG samples of three different molecular weights 5 kg/mol (M_w/M_n = 1.08), 35 kg/mol (M_w/M_n = 1.15), 150 kg/mol (M_w/M_n = 1.2) were purchased from Polymer Sources, Inc and gold nanorods were obtained from Sigma-Aldrich, Inc. The particle length, L and diameter d were determined to be 60 nm and 17 nm respectively, including the organic coating giving an aspect ratio of ≈3.5. The concentration of the gold particles and cetyltrimethylammonium bromide (CTAB) were ≈2 nM and < 0.1 wt% in the stock solution, which was diluted about a thousand times to prepare the solution used in our experiment. Many different concentrations of PEG with volume fraction, ϕ=0-0.32 in water-NR mixture as solvent were prepared.

We used the method of multiphoton fluctuation correlation spectroscopy (MP-FCS), which is particularly useful because it uses ultra dilute particle concentration (≈ nM or less). This eliminates possible complications arising from particle aggregation or change of polymer microstructure due to particles acting as a cross-linker. FCS outperforms the sensitivity of dynamic light scattering (DLS) experiments by few orders of magnitude and in contrast to DLS

experiments, scattering of the host media does not significantly complicate the experiment or its interpretation. Compared to conventional, single-photon excitation techniques, a number of significant advantages popularized two-photon or multi-photon spectroscopy. Their nonlinear nature of excitation when combined with a high numerical aperture (N.A) objective, limits signal generation to a tiny focal volume of on the order of 0.1 femtoliter. This significantly reduces background noise. Previously, we have shown that high luminescence efficiency of AuNPs upon multi-photon excitation can be used to probe their dynamics.[31] FCS is generally used to study the translational diffusion coefficient (D_T). The rotational diffusion (D_R) measurement of small molecules, such as dyes by FCS is problematic as the relevant time scale ($\approx$ ns) overlaps with triplet state kinetics.[32] For colloidal particles, rotational measurement requires an optically polarized signal, which can arise from their shape anisotropy. It had been demonstrated that gold nanorods behave like a dipole with absorption and emission occurring parallel to the major axis.[97,98] The rotational motion occurs at much smaller time ($\sim$ few μs) and sufficiently separated from translational motion ($\sim$few ms) so that both of them can be separated with little ambiguity.

To perform MP-FCS, we used a custom-built setup that utilized a Ti-Sapphire laser (Mai Tai, Spectra-Physics) at wavelength of 800 nm with pulse width of 100 femtoseconds at a repetition rate of 80 MHz. FCS measures the fluctuation of photon counts in very small volumes ($\sim 10^{-15}$ L) created by a diffraction limited laser focus with a high numerical aperture (N.A=1.25) oil-immersion objective. The emission is collected through the same objective and detected with two single photon counting modules (Hamamatsu, Inc). For polarization resolved experiments, a polarized beam splitter (Thorlabs, Inc) was placed before the detectors. By calculating the cross-correlation function, $G(\tau)$ of the intensity fluctuation and by choosing a suitable model, the rates of the dynamic processes are obtained.[31,32] The temperature during the experiment was the room

temperature ($\sim$23 ^{0}C). It is known that photothermal conversion by metallic NPs such as gold can generate local higher temperature, which can increase the particle mobility. Therefore, the laser power was kept below 1 mW and control experiments were performed to confirm that there is no systematic change of diffusion coefficients with power. In addition, we note that the two-photon excitation requires much lower average power compared to one-photon experiments.[98]

4.3 RESULTS AND DISCUSSION

A representative correlation function collected with linearly polarized excitation light and unpolarized detected light is shown in Fig 4.3.1. Using the convention used in Ref [32] we refer this correlation function as G_{XNP}. Experiments were also performed with [XXX] and [XXY] configurations, where the first letter denotes the excitation polarization and the next two letters represent detected polarizations. Z is the propagation direction of the incident light. We did not observe significant difference with respect to the measured rotational diffusion coefficients, though the amplitude of the rotational correlation function changes depending upon the incident and detected polarization states. Some experiments were also performed with circularly polarized excitation light by using a quarter-wave plate in the beam path, which results in autocorrelation functions with only the translational component. This was done to confirm that results were consistent with the curves when both components are present.
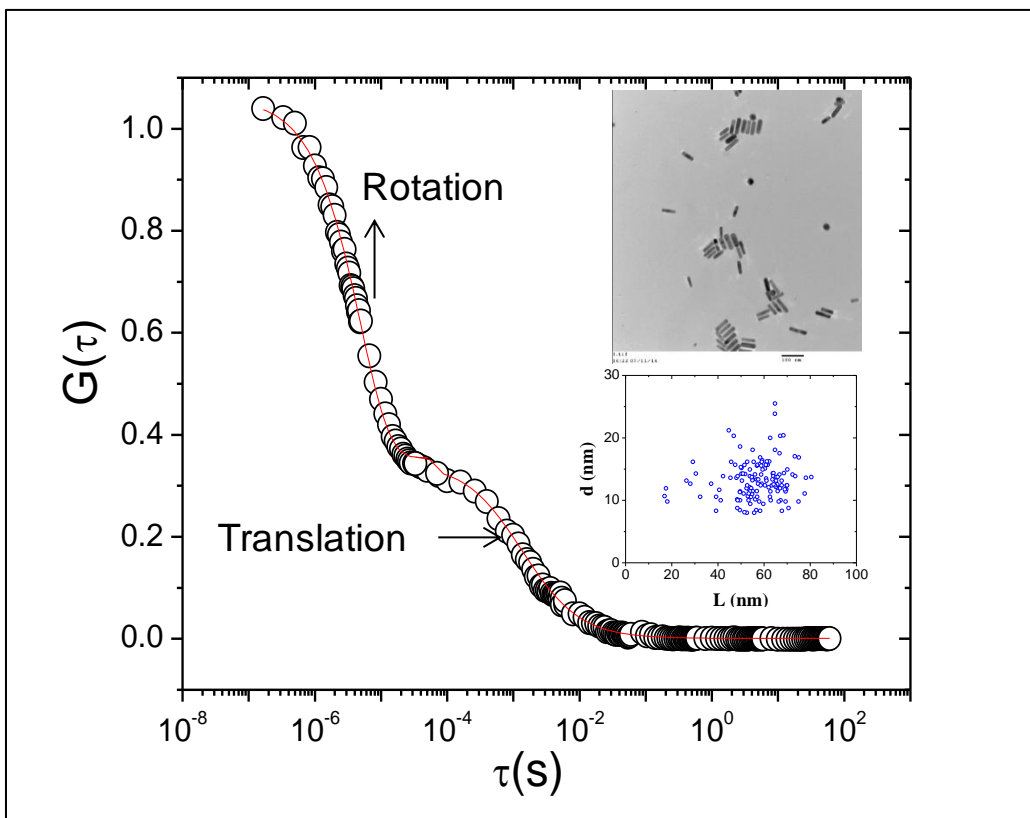
FIGURE 4.3.1: Autocorrelation function showing both the rotational and translational diffusion of the nanorods in water collected by using polarized MP-FCS. The solid line is fitting with the models described in the text giving D_R= 33556 $\pm$ 540 s^{-1} and D_T= 14.7 $\pm$ 0.3 μm^2/s. The measured D_R corresponds to rotation perpendicular to the long axis of the rod and D_T is the center-of-mass diffusion of the rod averaged over all orientations. (Inset) Transmission Electron Micrograph of gold colloids deposited on carbon film magnified 100 000x. A JEOL 2010 TEM with a LaB6 filament working at 200kV was employed to capture the image. The length and diameter of $\approx$150 such particles are shown, which gave the average L$\approx$56 nm and d$\approx$13 nm. The corresponding histograms are shown in Fig. 4.5.1.

The autocorrelation function in Fig. 4.3.1, $G(\tau)$ clearly showed two stage decays with the slower component at milliseconds time scale corresponds to the translational diffusion and the faster component at microseconds time scale is the rotational diffusion. As the translation and rotation are well separated in time scales, we used:

$$G_{tran}(\tau) = \frac{G(0)}{1 + (\frac{8D_T\tau}{\omega_0^2})\sqrt{1 + (\frac{8D_T\tau}{z_0^2})}}$$

4.1.1

$$\text{and, } G_{rot}(\tau) = R\exp(-6D_R\tau)$$

4.1.2

to fit the functions, which gives D_T and D_R, respectively.[31,32,97,98] Here, ω_o is the half-width of the laser focus ($\omega_o \approx 0.4$ μm) and z_o is the half-height of the laser focus ($z_o \approx 2$ μm) determined by a calibration experiment. As the size of the laser focus is much larger than the particle size and all relevant polymer length scales (Table 4.3.1), FCS measured the center of mass diffusion of the nanorods. The amplitude of the translation correlation function, $G_{tran}(\tau)$ depends upon the average number of the particles within the laser focus. The amplitude of the rotational correlation function, $G_{rot}(\tau)$ depends upon the polarization state of the excitation and emitted light as well as on the aspect ratio of the particle.

TABLE 4.3.1: Important parameters

PEG Molecular weight, M_w	5 kg/mol	35 kg/mol	150 kg/mol
Radius of Gyration $R_g = 0.02\, M_w^{0.58}$ (nm)	2.8	8.6	20
Volume fraction ϕ range	0.058 - 0.32	0.0037 – 0.32	0.003-0.14
Overlap volume fraction $\phi^* = M_w/(4/3*\rho*\pi*R_g^3*N_A)$ ($\rho_{PEG} = 1.126$ g/ml)	0.08	0.02	0.0067
Entanglement concentration $\phi_e = (M_e/M_w)^{0.76}$ ($M_e = 2$ kg/mol for PEG)[4]	N.A.	0.12	0.04
Correlation Length $\xi(\phi) \approx R_g\,(\phi/\phi^*)^{-0.76}$ (nm)	1 – 3.6	1 – 31	2- 34
Tube diameter $d_t(\phi) \approx d_t(1)\,\phi^{-0.76}$ (nm) $d_t(1) = 4$ nm[4]	N. A.	9.5 – 20	17.5 – 46

TABLE 4.3.2: Two crossover volume fractions ϕ^ξ and ϕ^d for AuNRs in PEG

AuNR effective radius R_o (nm)	$\phi^\xi \approx \phi^*\left(\dfrac{R_g}{2R_o}\right)^{1.32}$	$\phi^d \approx \left(\dfrac{2R_o}{a(1)}\right)^{-1.32}$
14.7 for translation	0.004	0.07
17 for rotation	0.003	0.06

TABLE 4.3.3: Theoretical and experimental diffusion coefficients of NRs in water

Diffusion coefficient	Experiment	HS theory (no CTAB)	HS theory (CTAB)	TT theory (no CTAB)	TT theory (CTAB)	BR theory (no CTAB)	BR theory (CTAB)
D_R (s^{-1})	33930	53283	29975	64002	34193	55310	N.A.
D_T (μm^2/s)	14.6	15.1	10.49	20.2	15.4	15.8	N.A.

Transmission electron microscopy (TEM) image of the nanorods was shown in Fig. 4.3.1 inset and the corresponding histograms of the length (L) and diameter (d) were plotted in Fig. 4.5.1. We determined that L=56 ± 11 nm and d= 13 ± 3 nm. The gold nanorods are coated with an organic ligand, cetyltrimethylammonium bromide (CTAB), which is needed for their anisotropic growth and prevents particle aggregation. From the closest separation among the rods we estimated that that the thickness of the CTAB layer is ≈2 nm, which is comparable to the reported value of ~1-3 nm.[97] A perfect bilayer of CTAB would correspond to ≈ 4 nm, therefore, the coating on the NRs used in our experiments is formed by a monolayer of CTAB. The concentration of CTAB in the polymer solution was estimated to be about 10^{-3} wt%, which is much less than the polymer concentration. Therefore, we expect that the presence of the CTAB in the solution does not significantly affects the results presented here. In a recent experiment, it was shown that the measured translation diffusion coefficient could depend upon the wavelength used for excitation due to the anisotropy presented by the parallel and perpendicular components.[93] The effect is more pronounced near the LSPR frequency of ≈800 nm, which is far from our excitation wavelength due to the two-photon nature of our set-up. The excitation in our

experiments is closer to the transverse SPR mode. The transverse mode is much less sensitive to the diffusional anisotropy and variation of particle size, aspect ratio, etc. Therefore, the complications arising from interpretation of the autocorrelation function can be avoided. There are three commonly used theories for rod diffusion in a neat solvent: hydrodynamic stick (HS) theory, Tirado and Garcia de la Torre's (TT) theory, and Broersma's relation (BR). All of them give relationships of the form: $D_T \sim L^{-1} \ln (L/d)$ and $D_R \sim L^{-3} \ln (L/d)$.[32,33] We determined that TT theory is most suitable for our NRs because it is valid for short cylinders, and hence we used it for all calculations. As shown in Table 4.3.3, D_T is closer to the theoretical estimate, though D_R deviates significantly. The limitations of the theories in accurately predicting D_T and D_R have been noted before.[32,98]

The theories, mentioned above, used Stokes-Einstein (SE) relation with stick boundary condition, which is valid if a large solute molecule diffuses in a medium composed of much smaller solvent molecules. A rod can move parallel to the long-axis ($D_\parallel$) or perpendicular to it ($D_\perp$) and hydrodynamically a ratio of $D_\parallel/D_\perp=2$ is expected.[22] If polymers are present in the medium microscopic friction can play much more significant role, as recent theories and simulations have predicted.[86,99] To understand this, it is useful to classify a polymer solution in few categories depending upon the concentration.[17,100] For dilute concentration of polymer, where the concentration is below certain threshold overlap concentration (ϕ^*), the chains are essentially isolated with no interactions among themselves. In the semi-dilute situation, $\phi^* < \phi < \phi^e$, where ϕ^e is the entanglement concentration, the macromolecules begin to overlap, but there is no effective entanglement. In the concentrated region ($\phi > \phi^e$), which extends up to melt ($\phi = 1$), if the chains are long enough they can entangle. Two new length scales are introduced depending

upon polymer concentration.[4] The first is correlation length, $\xi(\phi)$ in the semi-dilute region, defined as the average distance from a monomer on one chain to the nearest monomer on another chain. The second is entanglement length or tube diameter $d_t(\phi)$ for $\phi > \phi^e$. The crossover volume fractions between different regimes, ϕ^*, ϕ^e and the length scales, $\xi(\phi)$, $d_t(\phi)$ can be estimated using scaling theory as shown in Table 4.3.1.

Theoretic studies developed so far considered mostly spherical particles. de Gennes and his coworkers had proposed that in situations, sphere radius $R_o \ll \xi(\phi)$, the particles slip easily through the polymer mesh and only feel the solvent viscosity (η_o). In the opposite limit, they feel the macroscopic viscosity of the solution (η_b). In the transition region, the particles feel the local viscosity (η_c) such that $\eta_o < \eta_c(\phi) < \eta_b$. It has been argued that the local viscosity is governed by a scaling function, which depends upon the polymer concentration only through correlation length and independent of polymer molecular weight. Various hydrodynamic theories have been developed to describe the dependence of the scaling function, $\eta_c(R_o/\xi)$.[18,23,101]

In Figure 4.3.2, we have shown measured $D_T(\phi)$ and $D_R(\phi)$ as a function of ϕ for three different molecular weights, 5 kg/mol (5K), 35 kg/mol (35K), 150 kg/mol (150K). The 5K polymer is too short for entanglement, though 35K and 150K can entangle at high enough volume fractions, $\phi > \phi^e$. The two crossover concentrations, ϕ^* and ϕ^e were also shown in Fig. 4.3.2. The solid line is fitting with the hydrodynamic model, which treats the polymer mesh as statistical network and assumed that the hydrodynamic interaction between the particles and polymer dominates over topological constraints for all concentrations. The Phillies model provided an empirical equation of a stretched exponential function for diffusion:

$$D \sim \exp(-\beta\phi^\nu) \qquad\qquad 4.1.3$$

where β and ν are phenomenological parameters.[23] Cuckier argued that hydrodynamic interaction is screened at the correlation length scale, which yields $\nu = 0.76$.[18] In Fig. 4.3.2, the fitting with this model was shown for all three molecular weights. The comparison indicated that in 5K solution, the hydrodynamic theory predicts the diffusion of the nanorods very well for all polymer concentrations. Within 35K and 150K solutions, the diffusion of NRs cannot be predicted by Cuckier model in particular at concentrations above ϕ^e. In this situation, the particle diffusion is much faster compared to the prediction of the model.
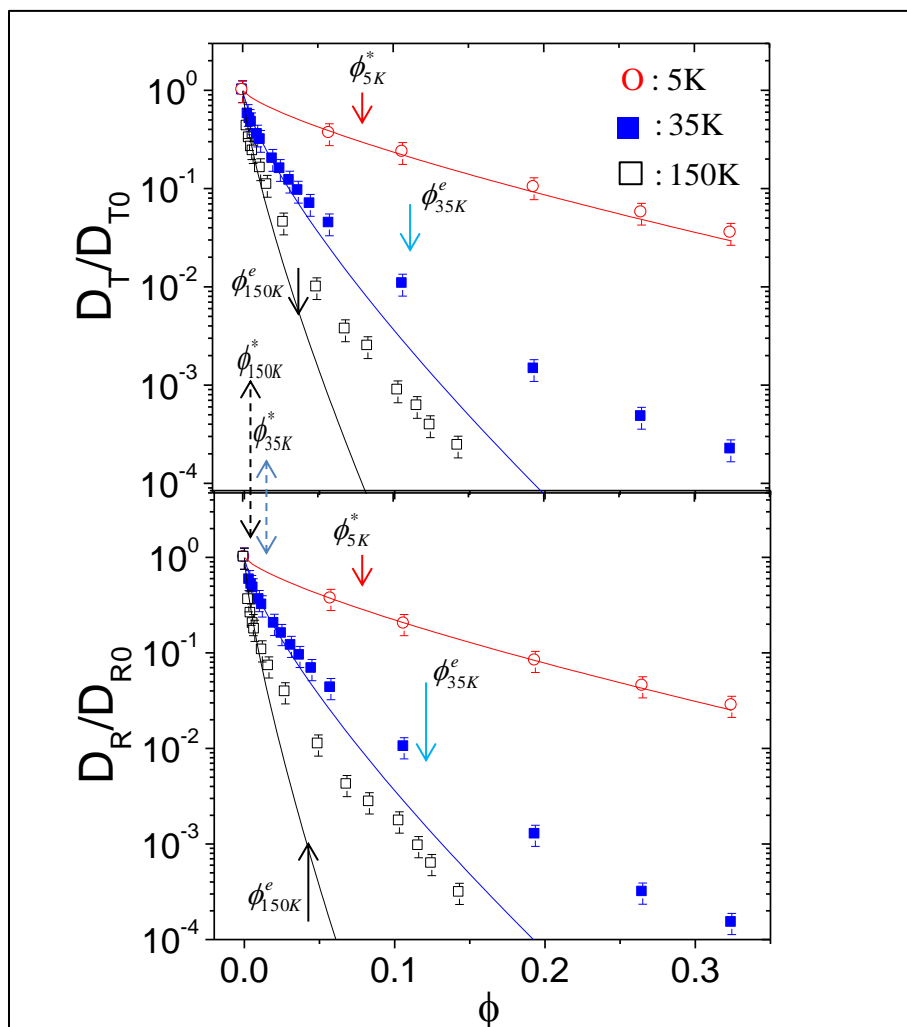
FIGURE 4.3.2: Translation (top) and rotation (bottom) diffusion coefficients as a function of polymer volume fraction. The data has been normalized with respect to the diffusion coefficients in water. The solid lines show fits according to Cuckier model. The caption indicates the polymer molecular weight. The crossover volume fractions (ϕ^* and ϕ^e) are also shown. The data indicates that diffusion of nanorods is faster compared to hydrodynamic prediction for higher molecular weights.

For a rod-like object in polymer melt, the scaling analysis has shown that friction force along the long axis of the rod ("easy" direction) can be very different compared to perpendicular

to it ("hard" direction).[22] For $d_t < d$ the ratio $D_{\parallel}/D_{\perp} \sim L/d \approx 3\text{-}4$ for the NRs used in this study ($L \approx 60$ nm, $d \approx 17$ nm with CTAB coating). For situations, when $d < d_t$, the ratio $D_{\parallel}/D_{\perp} \sim \eta_b a/\eta_1 d_t$, where 'a' is the size of a monomer and η_1 is the viscosity of the polymer liquid consisting of monomers only. For typical values of these parameters, the diffusion anisotropy can be extremely large. Our experiments are sensitive only to rotation perpendicular to the long axis as the rotation along the major axis of the rod does not change the directions of absorption and emission diploes. The rotation occurs at the time scale of few μs in water as shown in Fig. 4.3.1. The translation diffusion involves the center-of-mass motion and it takes about a $\sim$ms for the particles to cross the laser focal volume. Therefore, translation averages over a thousand rotations and our experiments cannot distinguish between diffusions along the long axis of the rods or perpendicular to it (Fig. 4.3.1 inset). Therefore, in the following we used an effective sphere approximation for the rods and compare the results with the theories developed for nanospheres. In addition, the aspect ratio of the particles used in our experiment is moderate ($\approx$3) so that this approximation is acceptable.

From the measured translational and rotational diffusion coefficients in water, D_{T0}=14.6 $\mu m^2/s$ and D_{R0}=33556 s^{-1}, we determined that effective hydrodynamic radii for the particles $R_o \approx$ 16 nm. The diffusion coefficient is slightly higher for rotation compared to translation (Table 4.3.3) because the differences in friction coefficients (ζ), which for translation is given by, $\zeta_T = 6\pi\eta_b R_o$ and for rotation, $\zeta_R = 8\pi\eta_b R_o^3$ using stick boundary condition.[32] The diffusion coefficient is related to friction coefficient via well-known Einstein relation:

$$D = k_B T/\zeta \qquad\qquad 4.1.4$$

where k_B is the Boltzmann constant, T is the absolute temperature. The approximation helps us to analyze our data beyond hydrodynamic models.

For 5K polymer, the size of the chain has been estimated as $R_g \approx 3$ nm and the correlation length, $\xi(\phi)$ is varied between 1-4 nm in the measured concentration range. Therefore, the particle is bigger compared to all length scales in the matrix and the effect of the polymer is to simply increase the viscous drag. Both rotation and translational diffusions are determined by hydrodynamic contribution and microscopic friction plays negligible role. To understand the deviation for longer chains, we need to use more sophisticated theories that have been developed in the recent years. Cai, *et. al.* have developed a scaling theory, which considered the roles of segmental motion and entanglement dynamics on nanosphere mobility.[17] Their theory is applicable in both polymer solutions and melt. The scaling theory considered three different size regimes all of which depend upon the particle size: (i) Below a certain volume fraction, $\phi^\xi \approx \phi^*(R_g/2R_o)^{1.32}$, the probe does not feel the presence of the polymer and diffusion is determined by the solvent viscosity (η_o). (ii) For $\phi^\xi < \phi < \phi^d$, the segmental motion of the chains affect the sphere motion, and $D \propto \xi^2 \propto \phi^{-1.52}$. The crossover volume fraction, $\phi^d \approx (2R_o/d(1))^{-1.32}$, where d(1) is the entanglement tube diameter in the melt and (iii) for $\phi > \phi^d$, the particles are trapped. The probe motion is determined by the reptation time scale of the surrounding polymer chains, which gives $D \propto \phi^{-3.93}$. In Fig. 4.3.3, we showed the crossover concentrations, ϕ^ξ, ϕ^d and the corresponding power laws in log-log plot. One issue of the scaling theory is that transition regions are not sharply defined and it cannot provide numerical prefactors. In spite of these limitations, we found good agreement with our assumptions.
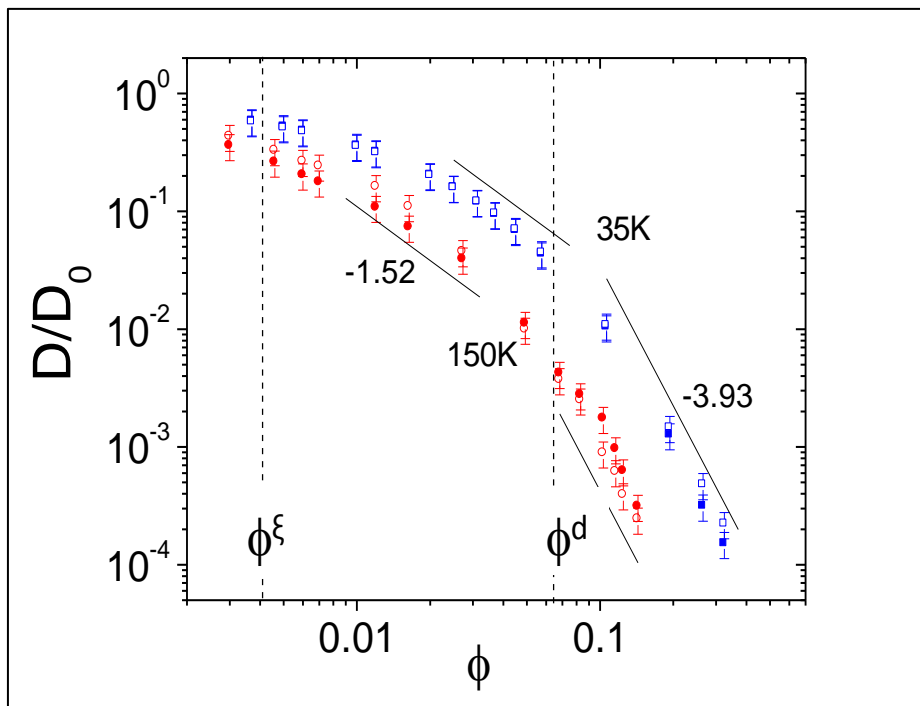
FIGURE 4.3.3: In log-log plot, the comparison of $D(\phi)$ with scaling theory (Ref.17) is shown. The scaling predictions are solid line. The open symbols are translational diffusion and filled symbols are rotational diffusion. The two crossover volume fractions, ϕ^{ξ} and ϕ^{d} are also shown by the dashed lines. All the relevant parameters are listed in Table 4.3.2. The data for 5K was not plotted as they agree with hydrodynamic theory.

However, some differences were also observed. In the intermediate size regime, $\phi^{\xi} < \phi < \phi^{d}$, the diffusion coefficient is expected to be independent of polymer molecular weight and determined by the local viscosity of a polymer liquid with chain size equal to the particle diameter. In our experiments, a clear dependence of D on the molecular weight was observed with $D_{35K} > D_{150K}$. This is because for 35K polymer, $R_o > R_g$ and in this situation the polymers feel the full solution viscosity (η_b). Also, according to the theory, in the large size regime: $\phi > \phi^{d}$,

the Brownian diffusion is expected to be governed by the full solution viscosity, $\eta_b \sim M_w^3$.[17] This would indicate, $D_{35K}/D_{150K} = 80$, however, the analysis of our data indicated the ratio to be smaller.

An understanding of these discrepancies required comparison of the solution viscosity (η_b) with the nanoviscosity, η_c (ϕ) determined from measured diffusion coefficients. We used Tirado and Garcia de la Torre's (TT) theory with stick boundary condition to calculate η_c.[32] Using slip boundary condition will decrease η_c (ϕ) by a factor of ⅔ although will not change qualitatively any conclusion. A multiplication factor to the TT theory has been applied so that at $\eta_c(0) = 0.9$ cP is obtained, which is the viscosity of water at the room temperature. The bulk viscosity information of PEG-water solutions at different volume fractions and PEG molecular weights were obtained from the rheology data.[102] From Fig. 4.3.4, we concluded that both translation and rotation of the rod experience similar nanoviscosity.
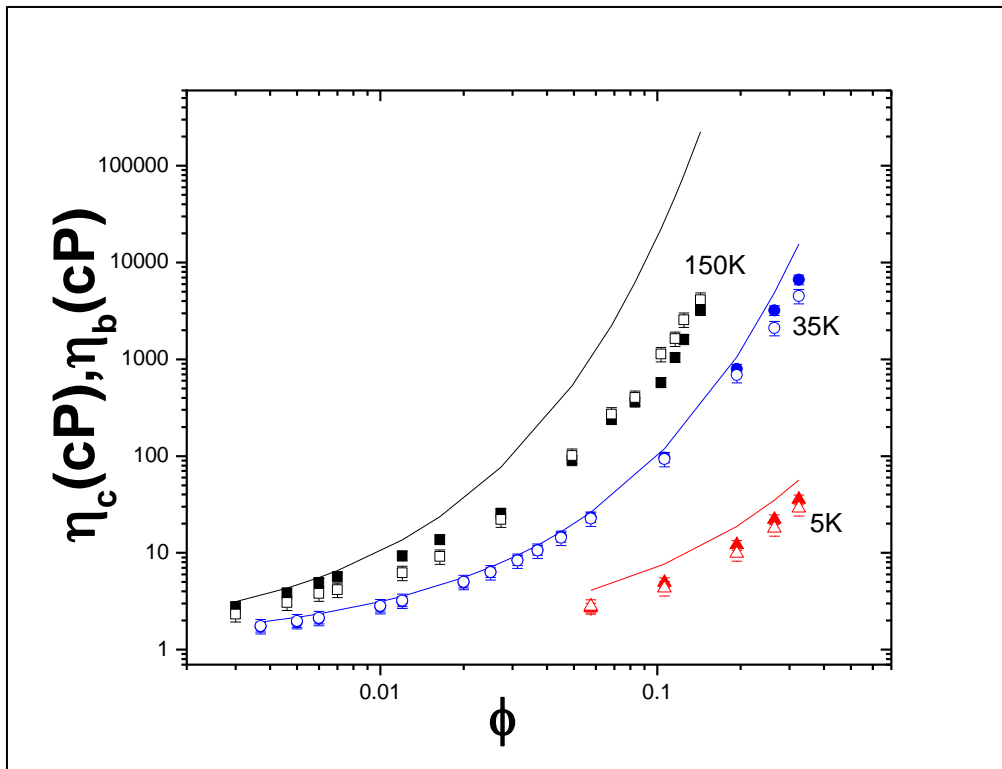
FIGURE 4.3.4: The nanoviscosity, η_c (ϕ) is compared with the bulk viscosity, η_b (ϕ) for three different molecular weights as a function of polymer volume fraction, ϕ. Both translation and rotation are governed by the same nanoviscosity for the AuNR studied. The solid symbols are rotational and open symbols are translational nanoviscosity. The solid line is the bulk viscosity. In 5K and 35K PEG solutions, η_c (ϕ) $\approx \eta_b$ (ϕ), but deviations were observed in 150K solution.
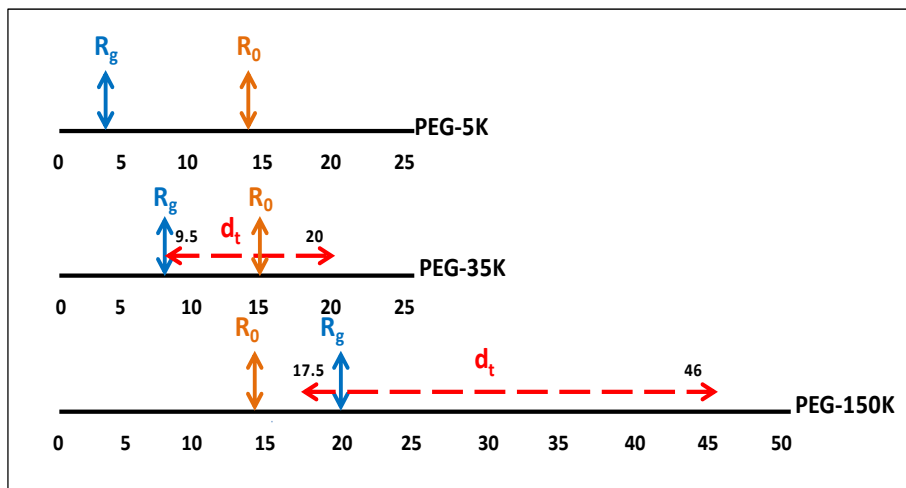
FIGURE 4.3.5: Shows the relevant length scales for the three different systems. The scale is in nm.

In both 5K and 35K solutions the rods experience the macroviscosity for all concentrations. A difference of factor of ~2 in the ratio η_c/η_b can originate from the uncertainties in determining the bulk viscosity. But in 150K solution the particles experience a much smaller nanoviscosity and the ratio η_c/η_b increases with increasing ϕ. This is consistent with our earlier results of nanosphere diffusion in polymer solutions[31] and experiments of Holyst *et. al.*[102], who used various sized proteins and dye molecules in polymer solutions. Those results were interpreted as the radius of gyration (R_g) of the chain being the crossover length scale from nanoviscosity to macroviscosity.[31,102] We estimated that for NRs, R_o/R_g=5-6 for 5K, R_o/R_g = 1.5-2 for 35K, R_o/R_g = 0.5-1 for 150K. Therefore, if R_g is the crossover length scale, then nanorods in 5K and 35K solution will experience very close to the bulk viscosity, while in 150K it will experience a smaller nanoviscosity.

Using force based microscopic theory Yamamoto *et. al.* have shown that for nanosphere diffusion $\eta_c/\eta_b = 1$ would require the probe size, $R_o > \frac{3}{2} R_g$ in unentangled liquid and $R_o > 3\text{-}5\ d_t$ for entangled liquids.[86] According to this theory, $D = D_{SE} + D_m$, where D_{SE} is the hydrodynamic contribution determined by η_b and D_m is a microscopic contribution originating from nanoparticle-polymer forces and structural relaxation. Their theory is applicable for melts, and therefore it ignores the transient pore-like structures in semi-dilute solutions. But recent microrheology experiments in DNA solutions had confirmed the cross-over length scale in entangled solution.[103] Those experiments were performed at a fixed concentration of DNA and the effect of length scale was inferred by changing DNA molecular weights. A comparison of microscopic theory with our results in Fig. 4.3.4 showed that in unentangled polymer the crossover length scale $\sim R_g$ is confirmed. In entangled solution the situation is more interesting. In 35K, tube diameter (d_t) was varied from $\sim$10-20 nm in our experiments, so $R_o/d_t(\phi) \approx 1\text{-}1.6$ and $\eta_c/\eta_b = 1$ is obeyed closely. However, in 150K solutions, the tube diameter $d_t(\phi) \sim$18-46 nm, which gives $R_o/d_t \approx 0.4\text{-}1$ and deviation from η_b was observed. These features are consistent with the microscopic theory. The theory predicts that as the concentration is increased in the entangled regime, the ratio η_c/η_b should decrease as the tube diameter $d_t \sim \phi^{-0.76}$. It is expected that at high enough concentrations of polymer as R_o/d_t is increased much beyond 1, eventually η_c/η_b should approach unity. At present, we could not confirm this prediction because the NP dynamics becomes extremely slow to be measured by MP-FCS.

Egorov had used mode coupling theory (MCT) to study NP diffusion in both solutions and melts.[99] The results, which were confirmed with molecular dynamics (MD) simulations for shorter chains also demonstrated the importance of the microscopic diffusion, D_m. The results showed that at a fixed polymer volume fraction and for $R_o/R_g < 1$, the microscopic friction can

completely dominate over the hydrodynamic friction. However, for $R_o/R_g > 1$, the hydrodynamic term will dominate. The theory also predicts a larger contribution of the microscopic term at a higher polymer concentration for fixed R_o/R_g. The theory did not explicitly consider the effect of chain entanglement and the solvent is implicit. Even though, it can qualitatively explain some features of Fig. 4.3.4. The deviation from $\eta_c/\eta_b=1$ for the rods in 150K, where $R_o/R_g < 1$ is much stronger at higher concentrations, where D_m determines the total diffusion. MCT theory also predicts that for higher molecular weight polymer, the deviation from hydrodynamics start at even lower volume fraction. This is also observed for both 35K and 150K solutions. A more quantitative understanding of our results, however, will require expansion of these theories to more realistic polymer solutions or large scale computer simulations.

4.4 CONCLUSIONS

We showed that polarized MP-FCS can be used to determine both translation and rotational diffusions of nanorods in a polymer matrix. We have used an effective sphere model for the NRs to compare our results with the available theories. Within measurement uncertainties, both translation and rotation of the rod experience the same frictional force. Our results showed that the scaling theory, which takes into account the polymer segmental motion and entanglement dynamics, can explain some features of our experiments. For longer chains, deviation from continuum hydrodynamics was observed. This showed the importance of microscopic friction in determining the particle dynamics. The results presented here shed light on the dependence of this friction force on polymer molecular weight and volume fraction. This will stimulate development of more sophisticated theories as well as simulations with aim towards better understanding of the transport behavior of asymmetric shaped particles in complex fluids.

4.5 SUPPORTING INFORMATION:

(a)

(b)
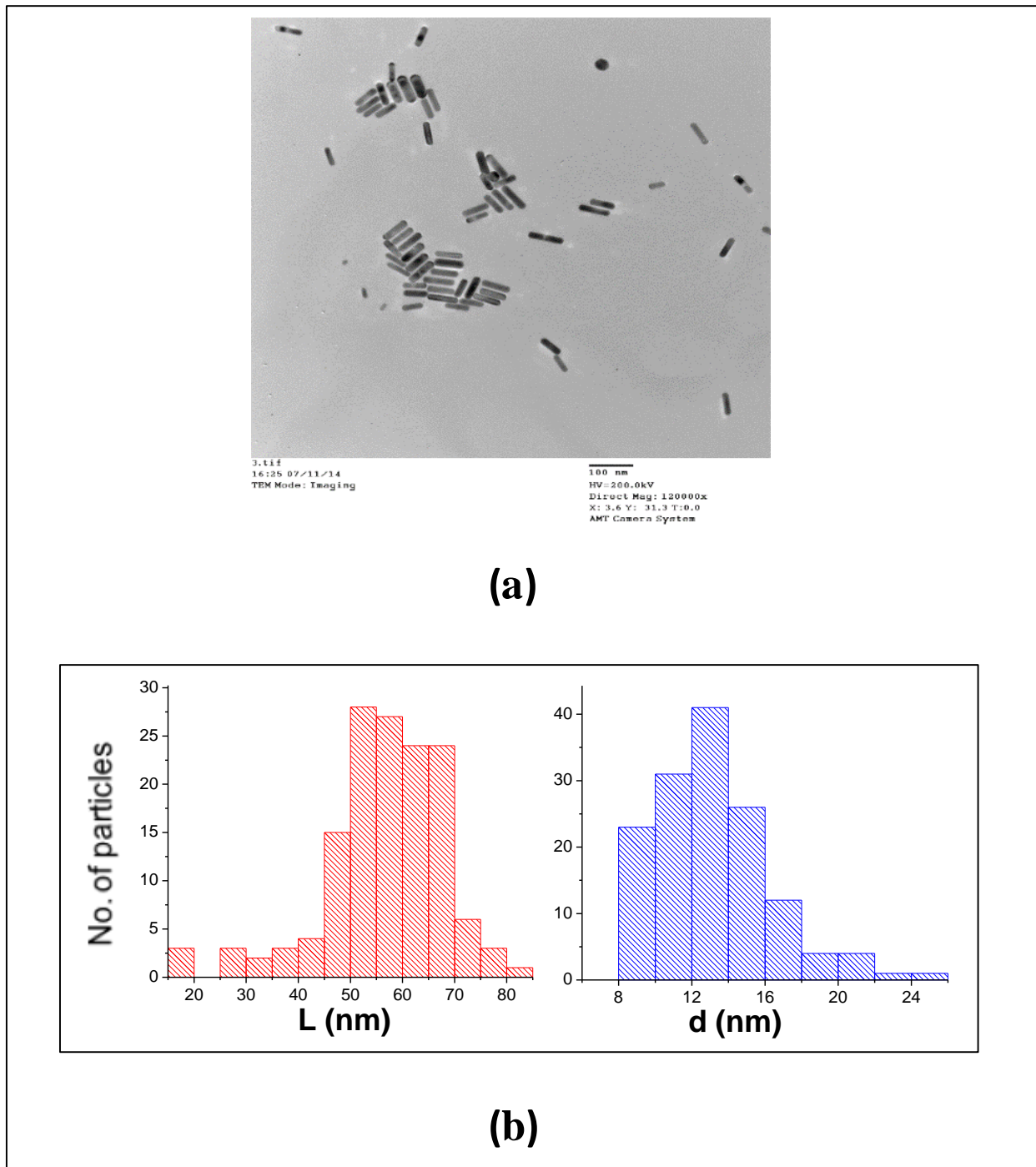
FIGURE 4.5.1: (a) TEM image of AuNPs deposited on carbon film magnified 800000×.JEOL-

2010 FasTEM Transmission Electron Microscope (TEM) with a LaB6 filament working at 200

kV was employed for imaging. (b)The histograms of length (L) and diameter (d) of the

nanorods. The analysis gives L=56 $\pm$ 11 nm and d=13 $\pm$ 3 nm.

CHAPTER 5

DYNAMICS OF ANISOTROPIC PARTICLES IN BIOPOLYMER SOLUTIONS

5.1 CONJUGATION OF GOLD NANORODS WITH BOVINE SERUM ALBUMIN PROTEIN

The following material was originally published in Journal of Physical Chemistry C (2014).[104]

Anisotropic shaped particles are being widely used for applications ranging from self-assembly[105] to drug delivery.[106] The gold nanorods (AuNRs), in particular, have received a lot of attention because of their unique photo-physical properties.[93,94,106] We are interested here to understand the interaction of AuNR with protein solutions. The motivation for this study is that these particles have found numerous biomedical applications, such as sensing, imaging, delivery agents for drugs or genes, and localized hyperthermia for cancer therapy.[91,92,107] They are biocompatible and non-toxic, giving them advantages compared to semiconductor quantum dots.[32] One specific benefit for using rod-shaped gold particles, instead of spheres is that localized surface plasmon resonance (LSPR) frequency can be tuned by changing the aspect ratio (length/diameter).[92] In particular, AuNRs with an aspect ratio $\approx$ 3-4 showed a longitudinal LSPR near the infrared region (~800 nm), which has higher penetration depth through tissues (Fig. 4.1.1).

For the safe applications of NRs, as well as other nanostructures, their interaction with various proteins needs to be understood. Due to the large surface-to-volume ratio, even a small amount of NP provides a large area for protein binding. As soon as NPs are exposed to biological fluids, they become coated with various proteins, which form a surrounding layer called 'protein corona'.[50,108] The protein corona shields the original surface of the NP and consequently, the interaction of the corona with other biofluids governs many properties of NP-based drug delivery

systems.[49,52] If the protein retains its native conformation, it can facilitate cellular uptake. But if the structure of the protein molecules in the corona is modified, it could potentially give rise to toxicity effect. As a model protein we used bovine serum albumin (BSA), which is similar in composition and structure to human serum albumin (HSA).[109] This protein is abundant in the circulatory system and constitutes the majority of the plasma fluid in variety of organisms.[52] The NP-protein interaction and the characteristics of the protein corona depend upon size, shape, and surface chemistry of the particles. The interaction of BSA with differently functionalized gold nanospheres (AuNS),[50,51,109] quantum dots (QDs),[49] and FePt NP[49] was studied before. Recent research, however, have shown that protein corona composition, cellular uptake as well as toxicity of anisotropic particles can be very different compared to spherical particles,[108,110-112] This needs to be properly understood for safe applications of NPs possessing different shapes.

We took advantage of the two-photon excitation of the metallic nanorods to measure the change of the diffusion coefficients *in situ* as a function of protein concentration. Due to their shape anisotropy both translational (D_T) and rotational diffusion (D_R) of the NR can be measured by using polarized optics. But the rotation diffusion is much more sensitive to protein adsorption compared to translation diffusion as $D_R \sim (1/L^3) \ln(L/d)$, while for $D_T \sim (1/L) \ln(L/d)$, where L is the length and d is the diameter of the rod.[32] We measured the increase of the hydrodynamic size of the particles as a result of BSA absorption and compared them with Langmuir and non-cooperative binding models. In contrast to gold nanospheres, our results showed incomplete coverage of proteins on the nanorods. We believe that the results presented here will be important in fields ranging from biophysics to drug delivery, where surface interaction and diffusion of nanoscale objects in complex macromolecular fluids are important.

5.2 EXPERIMENTAL SECTION

Bovine serum albumin (BSA) (fraction $\geq$ 96% lyophilized powder, M_w = 66463) was purchased from Sigma-Aldrich Inc. and used without further purification. Cetyltrimethylammonium bromide (CTAB) stabilized gold NRs was also obtained from Sigma-Aldrich, Inc. The concentration of NRs in the solution was $\approx$2-3 nM, which was diluted by a thousand times to prepare the sample for p-FCS experiments. The protein powder was diluted using phosphate buffer (pH 7.0) as a solvent to prepare many different concentrations of BSA solutions (1 μM to 10 mM). A home-built cylindrical glass cell with the bottom plate made of borosilicate cover glass of thickness ~0.17 mm was used as a liquid cell. The cell was thoroughly cleaned using a base bath and rinsed with distilled water before use. An inverted microscope was used as an experimental platform and the cell was mounted at the mechanical stage attached with the microscope (Axiovert 200, Zeiss). Ti:sapphire laser (Mai Tai, Spectra-Physics) of near infrared light (wavelength 800 nm) with pulse-width of 150 femtoseconds at a repetition rate of 80 MHz was focused on the sample through a high numerical aperture (N.A. = 1.25, 100x) oil immersion objective. The objective excites a tiny volume of ~10^{-15} L inside the sample. Emitted light was passed back through the same objective, transmitted by a dichroic mirror that transmits light of wavelength below 600 nm. This arrangement blocks scattered light from the particles, which can complicate interpretation of the diffusion data.[93] Finally the emitted light was detected by two single photon counting modules (Hamamatsu, Inc.). A polarized beam splitter was placed before the detectors for polarization resolved experiments. A commercial integrated data acquisition system (ISS, IL) was used to record and analyze the output photon counts. The photon counts fluctuate as a function of time due to rotational diffusion and as the particles diffuse in and out of the laser focus. The fluctuation (δF) of the NRs is quantitatively studied

through the autocorrelation function (ACF), $G(\tau)$ which is analyzed to determine the translational

(D_T) and rotational (D_R) diffusion coefficients.[32] Each correlation function was collected for

about 10 min and a minimum of five different FCS trials were performed for each

concentrations. To calibrate the focal volume we used a common dye Rhodamine 6G, whose

diffusion coefficient of water is well known.[113] We determined that the half-width (ω_o) and half-

length (z_o) of the focus are 0.4 μm and 2 μm, respectively. As the particle size is much smaller

than the focal dimension, we can use point particle approximation to analyze FCS data. FCS has

a great advantage of using extremely low particle concentrations of much less than a nanomolar,

which are ~3-5 orders of magnitude smaller compared to common spectroscopy or dynamical

methods. This helps to prevent particle aggregation during experiments, which simplifies

analysis of the data and comparison with theoretical models.[51] In addition, two-photon

luminescence of gold NPs offer advantage of using very low laser power compared to scattering

correlation spectroscopy or one-photon technique, which were used to study dynamics of

metallic NPs in the recent years.[50,93]

5.3 RESULTS AND DISCUSSION

The transmission electron microscopy (TEM) image of the rod was shown in Fig. 5.3.1

inset. From ≈150 such particles, we determined that L=56 ± 11 nm and d=13 ± 3 nm (Fig. 4.5.1).

To estimate the CTAB thickness, we used the minimum separation of the rods in a side-to-side

arrangement. This yields approximately twice the thickness of CTAB layer, which we estimated

to be δ =2.2 ± 0.4 nm. As the current theories of determining the length and the diameter of the

rods from the measured translation and rotational diffusion coefficients are not very accurate, we

feel that this is a better approach at this time. It also yields CTAB thickness, which is comparable

to the reported values between 1-3 nm.[52] In Fig. 5.3.1, we showed the autocorrelation function (ACF) of CTAB functionalized AuNRs in buffer. We used a configuration of [YXY], where the first letter corresponds to excitation polarization and the next two letters correspond to detected polarization using the convention used in Ref. [32]. Z is the propagation direction of the incident light. The clear two-step decay in the ACF indicates the translation and rotation diffusion of the rods and the fitting gives $D_T \approx 13.4 \pm 0.5 \ \mu m^2/s$ and $D_R \approx 29574 \pm 433 \ s^{-1}$. The translational part of the correlation function, $G_{tran}(\tau)$ and the rotational part, $G_{rot}(\tau)$ were fitted with using:

$$G_{tran}(\tau) = \frac{G(0)}{1+(\dfrac{8D_T\tau}{\omega_0^2})\sqrt{1+(\dfrac{8D_T\tau}{z_0^2})}} \qquad \qquad 5.1.1$$

$$G_{rot}(\tau) = R \exp(-6D_R\tau) \qquad \qquad 5.1.2$$

to fit the functions, which gives D_T and D_R, respectively.[32]
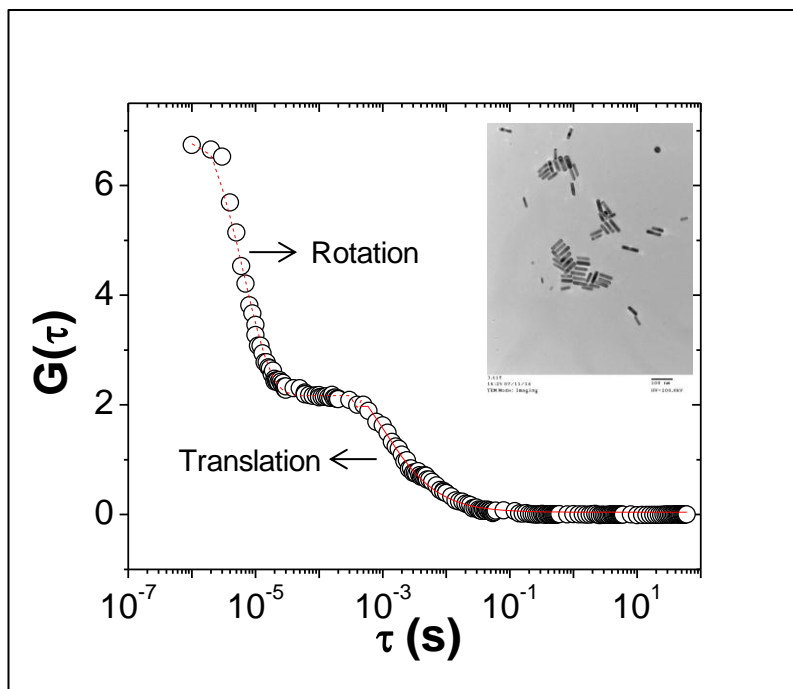
FIGURE 5.3.1: The cross-correlation function with fitting showing both the translational and rotational diffusions of the gold nanorods in phosphate buffer of pH 7.0. (Inset) Transmission Electron Micrograph of gold colloids collected using a JEOL 2010 TEM. The length and diameter of ≈150 such particles are shown giving the average L≈56 ± 4 nm and d ≈13 ± 4 nm.

We used Tirado and Garcia de la Torre's theory (TT) for rod diffusion in solvents, because it is valid for shorter cylinder, i.e., lower aspect ratio. The nanorods with the CTAB layer has average length, L≈60 nm and d≈17 nm. Using these values, TT theory gives $D_T=11$ μm^2/s and $D_R= 13792$ s^{-1}. The measured translational diffusion is in good agreement to the experimental value, but the rotational diffusion differs significantly. We believe that this is due to the limitation of these theories and note that similar discrepancy has been found before.[32] In Figure 5.3.2 we have shown some representative ACFs within different BSA concentrations plotted versus logarithmic time lag (τ). The curves clearly showed the characteristic diffusion time for both translation and rotational motion increase with BSA concentration. This is due to

combined effects of protein adsorption on the NR surface and increase of the solution viscosity. To obtain better quality curves with BSA in solution, we first ran FCS experiments with higher sampling frequency (~5 MHz) to capture the rotational part of the correlation functions, which occurs at a shorter time scale. Thereafter, translation component was obtained by using lower sampling frequency (~10 kHz). In Fig. 5.3.2, we have shown the rotational and translation curves separately with the fitting. We also performed controlled experiments using circularly polarized light, where only the translation component present. This was compared with the translation diffusion coefficient measured by cross-correlation curves obtained using [YXY] configuration. These two measurements gave similar results giving confidence in the measurements. It is known that BSA can induce aggregation of nanoparticles above certain concentration.[52] Therefore we carefully examined the intensity vs. time, I(t) traces to find any signature of aggregation, such as longer, brighter peaks. But we did not observe any aggregation. One reason could be that concentration of NPs used in our experiments (~pM) is more than three orders of magnitude lower compared to previous studies. This reduces the chance of particle aggregation significantly.
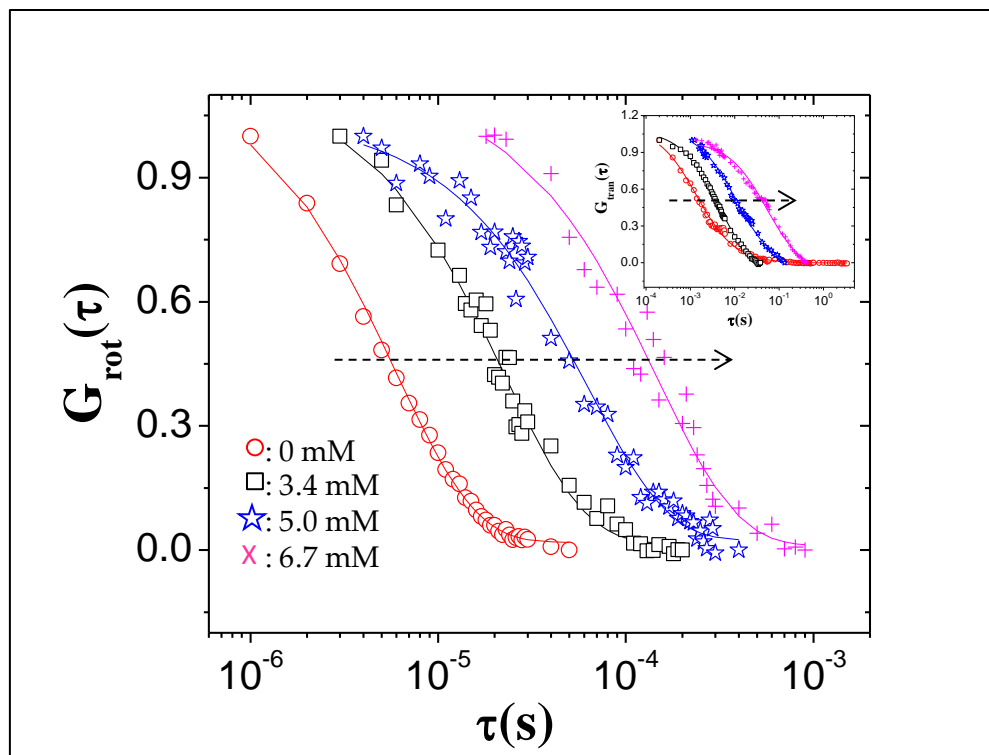
FIGURE 5.3.2: The rotational (main figure) and translational (inset) cross-correlation curves are shown separately for different concentrations of BSA. The arrow indicates direction of increasing concentration. Not all concentrations are shown because of clarity. The fitting functions are described in the text.

Figure 5.3.2 summarizes the data and the fitting corresponds to a stretched exponential function:

$$D=D_o exp(-\beta\phi^{\upsilon})$$ 5.1.3

which is known as Phillies' equation. It is widely used to empirically describe the diffusion of particles in semi-dilute polymer solutions.[31] Here, D_o is the diffusion coefficient in the low protein concentration, ϕ is the concentration of BSA, β and υ are adjustable parameters, where, $0 < \upsilon < 1$ is expected. The stretched exponential fitting gives $\upsilon = 0.97$ for translational diffusion, and $\upsilon = 0.95$ for rotational diffusion which are in marginal agreement with value close to 1.[23,100]

[114] But as shown in Fig. 5.3.3 residual plots, the fitting deviates systematically from the data, therefore, Phillie's fit is not appropriate to describe the anisotropic particle diffusion. Phillies equation is valid in the absence of interactions between the particle and the polymer, which is not the situation in the present study. We also noted that understanding diffusion of particles other than the spherical shapes in macromolecular solution is still a matter of theoretical challenge. But this is not the focus of the present work.
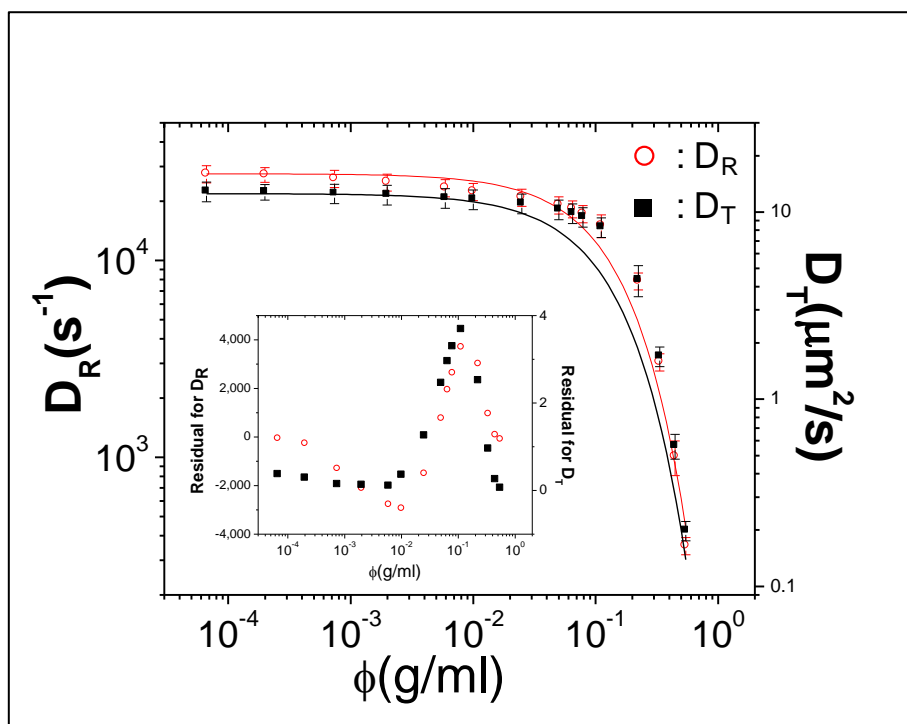
FIGURE 5.3.3: Rotational (D_R) and translational (D_T) diffusion coefficients of the nanorods are shown as a function of BSA concentration (ϕ). The error bars correspond to a minimum of five independent trials. The fitting is according to stretched exponential function. (Inset) The residual showed that systematic deviation from the fitting at all concentrations.

The conformation of BSA exhibits pH dependency with its native state (N) found between pH 4 and 8. The phosphate buffer (pH 7.0) used in our experiments thus corresponds to

the N state, which can be approximated as an equilateral prism with sides of 8 x 8 nm^2 and height 3 nm as determined by x-ray diffraction.[48] The equivalent hydrodynamic radius is estimated to be $\approx$3.7 nm.[115] To determine the thickness of adsorbed protein film onto nanospheres, one can directly use the Stokes-Einstein (SE) relation, which relates the diffusion coefficient with the hydrodynamic radius (R_h) of the sphere. Similar approach for rod-shaped particles is problematic as the analytical results are not very accurate, as mentioned earlier. But we may assume that the rotating rods behave hydrodynamically as spheres with an equivalent radius, R_h. As the translational diffusion time through the focus is much longer compared to rotational diffusion time, translation averages over thousands of rotations. Therefore, the difference between diffusion along the rod and perpendicular to it is not detectable. This assumption also helped us to compare the results with previous experiments of nanosphere interaction with BSA.

Using this, we can use theoretical values of $D_T = k_B T/6\pi\eta R_h$ and $D_R = k_B T/8\pi\eta R_h^3$ to calculate R_h, where k_B is the Boltzmann constant and T is the absolute temperature. We measured the viscosity (η) of the solution as a function of BSA concentration (ϕ) in the relevant range using a falling ball viscometer and use it to determine R_h as a function of BSA concentration (Fig 5.5.1). By assuming that the thickness ($\Delta\delta_R$) of the BSA is same on all sides, the average change at saturation has been found to be $\Delta\delta_R \approx 2.3\pm0.3$ nm for rotational diffusion and $\Delta\delta_T \approx 2.5\pm0.3$ nm for translational diffusion as shown in Fig. 5.3.4. Both measurements, therefore, gave consistent results, which is reassuring and justify our assumption. The saturation happens at $\approx$1 mM concentration of BSA, which is comparable to the serum albumin concentration in human blood ($\approx$0.75 mM).[50] The measured $\Delta\delta_T$ and $\Delta\delta_R$ are significantly less compared to previous observations of BSA monolayer adsorption onto different nanospheres' surfaces with thicknesses $\approx$3.5-4 nm.[49-51] Those results were interpreted by assuming that the protein retained its' native

three dimensional structure with the triangular base seated on the top of the gold surface (Fig. 5.3.4 inset).[50] The lesser thickness of BSA on CTAB coated gold nanorods, therefore can be explained either by incomplete coverage and/or by the loss of native conformation of the protein.
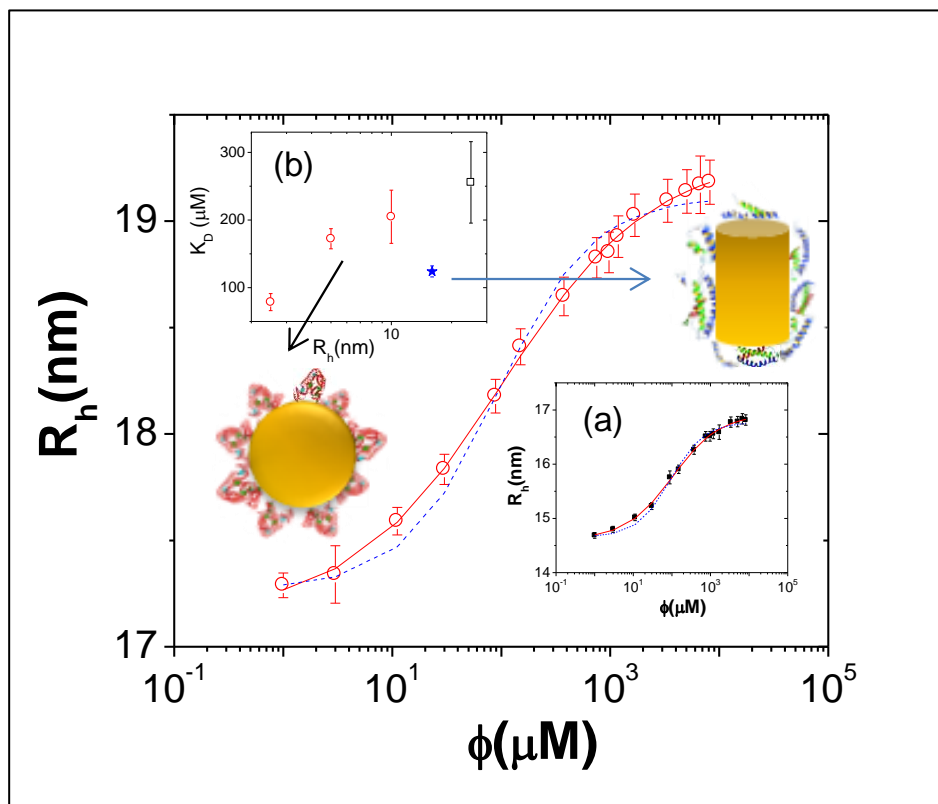
FIGURE 5.3.4: The change of the effective hydrodynamic radius of the particles obtained from rotational (main figure) and translational (inset a) diffusion measurements. The solid line is fitting according to anti-cooperative binding model and the dashed line corresponds to Langmuir fit. The BSA concentration ϕ (g/mol) (Fig. 5.3.3) has been converted to ϕ (μM) by using the relation ϕ(g/mol) = ϕ (μM)*M_w*10^{-9}, where M_w is BSA molecular weight. This was done to get the dissociation constant in the unit of μM, which is traditionally done. The schematic showed the difference of BSA adsorption on nanospheres and nanorods. (Inset b) The dissociation constant is shown as a function of particle radii. The square is citrate stabilized AuNS[50], circles

are tannic acid stabilized AuNS,[51] and the star is gold nanorods with an effective hydrodynamic radius and coated with CTAB.

To determine the maximum number of BSA adsorbed, we used the concept of Rocker *et.al.*, which expressed the hydrodynamic radii of protein-coated NRs as:

$$R_h([BSA]) = R_h(0) \sqrt[3]{1 + \frac{cN_{max}}{1 + (\frac{K_D}{[BSA]})^n}}$$

5.1.4

where N_{max} is the maximum number of bound proteins to the NR, K_D represents dissociation constant, and n is the Hill coefficient, which measures the degree of binding cooperativity.[49] The n=1 corresponds to Langmuir isotherm, where the adsorption of one protein does not influence the subsequent adsorption. In anti-cooperative binding model, where n < 1, previously adsorbed proteins sterically hinder subsequent adsorption. This would indicate repulsion between the free and bound BSA molecules as more sites get occupied, which would prevent formation of multilayer. The experimental data in Fig. 5.3.4 was fitted with this equation using R_h ([BSA]) from both translation and rotational motions. For rotational motion we obtained n = 0.63, N_{max}= 55, K_D = 121 μM and for translational diffusion n = 0.71, N_{max}= 59, K_D = 127 μM. Again comparable values were obtained with both sets of measurements. The Langmuir isotherm is also shown, which gives somewhat lower quality fitting compared to ant-cooperative binding model. The cross-section of folded BSA is ~32 nm^2 and the total surface area of the NR is ≈3660 nm^2, which gives the theoretical value for the maximum number of protein molecules absorbed is N_{max} = 115. This is significantly higher compared to fitting estimate, but consistent with the observation of less than a monolayer coverage.

Previously, citrate stabilized[50] or tannic acid stabilized[51] AuNS of different sizes were investigated. It was found that the thickness of the BSA layer was ≈3.5-4 nm, which indicated a complete coverage of the particle surface with a single layer of protein in its native state. The maximum number of BSA adsorbed, N_{max} obtained from fitting also agreed very well with theoretical calculation based upon particle area. The ligand coating makes the particle surfaces negatively charged with carboxyl group (COO^-) exposed outside. The isoelectric point of BSA is 4.6, so BSA in phosphate buffer (pH 7.0) is overall negatively charged. But BSA can still bind to negatively charged surfaces. This is due to several positively charged lysine amino acids at the protein surface, which can interact electrostatically with anionic particles.[50] In this scenario, there is no direct interaction between gold and BSA. An alternative ligand exchange mechanism has been suggested by Tsai *et. al.*[109] It hypothesized that the coating might be displaced by the BSA upon adsorption and it interacts directly with gold through the thiol bond with the unpaired cysteine residue. This can explain the increasing dissociation constant (K_D) with the increase of the particle size (R_h) as shown in Fig 5.3.4 inset (b) for gold nanospheres. The smaller nanoparticles will have better access to the sole surface amino acid compared to larger particle, indicating stronger interaction with the protein.

In Fig. 5.3.4 inset (b) we have compared K_D for nanospheres and the rod by assuming for latter an equivalent hydrodynamic sphere model. The data indicated that the interaction between the rod and BSA is much stronger (i.e. lower K_D) compared to an equivalent sized sphere. Therefore, a different mechanism of interaction needs to be sought. In contrast to citrate or tannic acid stabilized particles, CTAB is a cationic surfactant with the trimethylammonium $[N^+(CH_3)_3]$ head group of the first monolayer faces the surface of particles and the absorbed second layer

extended outside with hydrophobic tails hidden inside.[52] Therefore, both the shape of particle and the surface interaction can affect the protein layer structure.

The adsorption of BSA on planar self-assembled monolayer terminated with various end groups were studied using quartz crystal microbalance (QCM) technique.[116] The results showed that non-specific adsorption is highest on hydrophobic surfaces, followed by carboxyl (COO$^-$) and amine (H$_3$N$^+$) group. A perfect bilayer of CTAB would expose the trimethyl amino group [N$^+$(CH$_3$)$_3$] group at the surface. But such a layer would have a thickness of $\approx$4 nm, whereas our experiments have determined an average thickness of $\approx$2.2 nm. This indicates an imperfect bilayer surrounding the rods with many exposed hydrophobic tails. Therefore, hydrophobic interaction can play important role in the adsorption mechanism. The protein can unfold and the buried hydrophobic region can interact with the CTAB. In contrast to COO$^-$ terminated particles, in this situation interaction with CTAB results in a loss of protein native structure giving a thickness of less than $\approx$ 3.5-4 nm. This interpretation is consistent with previous study by Chakraborty *et. al.,* who also studied BSA interaction with CTAB coated AuNRs using absorption spectroscopy.[52] They concluded that the interaction is entropy driven with release of significant amount of bound hydrated water molecules. In their experiments, a large number of particle aggregates were observed, which is driven by BSA adsorption. But we did not observe any trace of aggregates, which can be explained by the fact that the particle concentration in our experiments was about $\approx$ 1-2 pM, which is thousand times lower compared to previous experiments. Therefore, our results are consistent with entropy-driven hydrophobic interaction between BSA and CTAB coated AuNR, which denatures the protein.

However, our results could also be interpreted through a different scenario. It is possible that CTAB coating on the rods is patchy and heterogeneous in thickness. TEM measurements do not have the necessary resolution to identify and characterize such layer. Therefore, it is possible that coating consists of a mixed bilayer and monolayer of CTAB. In this situation, the exposed surface of the rods becomes positively charged which can interact electrostatically with negatively charged BSA in the buffer. This can also explain sub-monolayer coverage of BSA found in our experiments.

5.4 CONCLUSIONS

In summary, we have demonstrated *in situ* evidence of BSA adsorption onto CTAB stabilized AuNRs by performing FCS experiments with single-particle sensitivity. The absorbed thickness reached saturation at ≈ 1 mM BSA concentration. The average change in thickness is $\approx 2.4 \pm 0.3$ nm which is less than if a BSA monolayer is formed around the particles. The estimated number of binding sites indicated surface coverage is about $\approx 50\%$. The results are significantly different compared to BSA adsorption on gold nanospheres, where the results could be interpreted in terms of a fully covered single layer of protein in its native conformation. From the observed data, we hypothesize that BSA interaction AuNR is determined by hydrophobic interaction, which results in loss of protein's conformation. A future goal is to isolate the effects of surface interaction from the shape of the particles. The results will be important to understand how anisotropic particles interact with and internalized into cell, which has not yet been explored in detail and understood clearly.

5.5 SUPPORTING INFORMATION
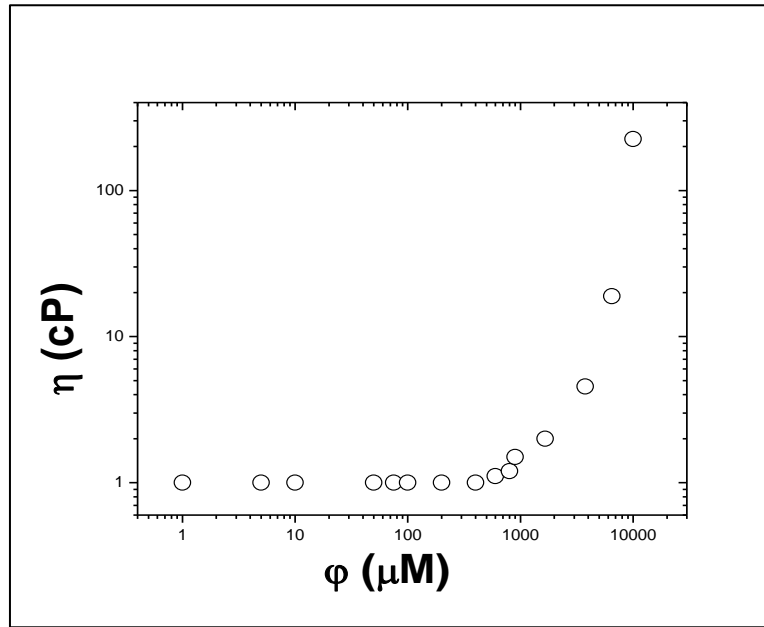
FIGURE 5.5.1: Viscosity vs. volume fraction plot for BSA in buffer (pH 7.0).

CHAPTER 6

DYNAMICS OF ANISOTROPIC PARTICLES IN SPHERE MIXTURE

6.1 TRANSLATIONAL ANISOTROPY AND ROTATIONAL DIFFUSION OF GOLD NANORODS IN COLLOIDAL SPHERE SOLUTIONS.

The following material was originally published in Langmuir (2015).[117]

The dynamics of non-spherical colloidal particles through complex fluids is a subject of great interest in diverse areas. For example, anisotropic particles such as gold nanorods (AuNRs) have shown promise to be used as diagnostic and therapeutic purposes.[106,118] The bottom-up approach of fabricating nanostructures using self-assembly can make use of anisotropic building blocks, which can provide a wider range of possibilities. Understanding the dynamics of such objects is important as the thermal energy which dictates the motion of the particles is comparable to the interaction energy at the nanoscale in many situations. One common approach to study the dynamics is the probe diffusion method, where a particle (the probe) is monitored as it diffuses through a suspension of other particles (the matrix). Many combinations of probe and matrix had been studied using both hard (e.g., silica, gold, etc.) and soft (e.g., polymer, proteins, etc.) objects.[119-121] Here, our interest is the study of gold nanorods within a matrix of Ludox spheres in the semi-dilute concentration regime, which is very relevant for the above mentioned applications.

The initial theoretical interest to study these systems originated in understanding the entanglement and caging in polymers, where rod-like molecules can behave as one of the model systems. Doi and Edwards (DE) provided the basis of understanding the dynamical behavior of rigid rods within semi-dilute or concentrated solutions of similar rods.[56,57,62] In the semi-dilute solutions, cages are transient, appearing and disappearing with time. As a result, theoretically it

is a very challenging problem. DE theory considered the concentration range of $1 << nL^3 << L/d$, where n is the number concentration of the particles, which has unit $(meter)^{-3}$, L & d are the length and diameter of the rod, respectively and both have unit meter, thus nL^3 is a unit less quantity. Within a highly concentrated solution, they argued that the neighbors create a "cage" which surrounds the probe and completely restricts its rotational motion. The rotation can happen only after the cage is 'dissolved' due to the translational diffusion of the rod along its axis ($D_{T\parallel}$). For ultrathin rods, $L >> d$, they derived[122]:

$$D_R = D_{R0}\beta\ (nL^3)^{-2} \qquad\qquad 6.1.1$$

where D_{R0} is the rotational diffusion coefficient in neat solvent and β is a numerical factor, whose value is predicted to be ≈ 1.

The subsequent experiments, however, showed significant discrepancies with the DE theory.[123-125] By using rod-like polymers, poly-γ-benzyl-L-glutamate (PBLG) the experiments have shown that rotational diffusion coefficient (D_R) to be much higher so that $\beta \approx 1000$ is needed to match with the DE theory.[124] There is also a concentration off-set effect and the inverse-square dependence is not obtained until a much higher value of nL^3. Eventually, sophisticated advances were made to refine the DE theory. According to Fixman,[63,126] the rod rotation can be due to two mechanisms: cage renewal as described by the DE theory and slight transverse translation and rotation of both the caging particles and the confined rod. The model showed angular jump, $\sqrt{\langle\theta^2\rangle}$, of the rods is proportional to $n^{-1/2}$, which yielded $D_R \sim n^{-1}$ and, thus in qualitative disagreement with DE theory. Keep and Pecora developed a geometric model,[60] which argued that predicted $D_R \sim (nL^3)^{-2}$ dependence will be obtained for $nL^3 > 500$ and significant caging is not expected unless $nL^3 > 50$. Farther improvements of the DE theories were made by

considering that only a part of the rod needs to be translated for cage renewal,[123,124] smaller rods can relax away faster for a polydisperse system,[127] etc.

We found only one experimental study on the diffusion of rod-like molecules within a sphere mixture. Phalakornkul *et. al.*[72] have studied PBLG molecules of three different molecular weights of aspect ratios (L/d) varying $\approx$30-90. The experiments probed the bulk anisotropy of the sample using transient electric birefringence (TEB) decay method. The matrix consisted of silica spheres with diameter $(2R_o) \approx 124$ nm with volume fractions between 0-0.08. For $L > 2R_o$ they found that $D_R \sim L^{-2.52}$ and not according to scaling prediction of L^{-4}. The diffusion is also decoupled from the matrix viscosity as D_R decreased much faster compared to the increase of the matrix viscosity. According to their analysis, the rotational relaxation of the rods is dominated by the collective diffusion of the spheres at the length scale of L, instead of the self-diffusion coefficient. It modified the concentration (ϕ) dependence, showing that $D_R \sim \phi^{-1}$ instead of $\phi^{-2/3}$. But, the shortest rod (L=68 nm) did not show any concentration dependence of D_R, so the results are not conclusive.

TEB decay method, which they used had few issues. As it is a bulk technique, a high concentration of rods (10 rods/L^3) is needed, so the caging can be affected by the spheres and by the rods as well. The method is also perturbative. As the silica particles are charged, the external electric field can affect the sphere motion and their ordering around the rods. The bending mode of the polymer can complicate interpretation of the data as Odjik[58,59] have shown that even slight flexibility can have a drastic effect on the rod confinement. In addition, the measurements cannot provide the absolute values of the rotational diffusion coefficients, but give only the ratio D_R/D_{R0}. So a quantitative comparison with theories is not possible.

In this study, we used gold nanorods (AuNRs), which is truly a rigid rod within a semidilute concentration of spheres using a non-perturbative optical technique of fluctuation correlation spectroscopy (FCS). By using polarized light, we were able to determine both the translational and rotational diffusion coefficients from the same experiment. We kept the rod concentration at $nL^3 \approx 10^{-7}$ so that any correlations among them is negligible and true self-diffusion coefficient is measured. The rod has an aspect ratio ≈ 4, which is at least an order of magnitude smaller compared to polymer molecules. The size of the crowding spheres is comparable to the dimensions of the rods and their concentration is varied up to volume fraction (ϕ) of 0.3 or approximately 7 spheres/L^3. These size and concentration regimes are appropriate for understanding the effects of crowding on rod diffusion in biological systems, where gold NRs with aspect ratio ~3-4 have shown promise for diagnostic and therapeutic applications.[128] Our results will also be important for self-assembly of a mixture of spherical and non-spherical particles, where depletion interaction among the non-spherical particles due to the presence of similar sized spheres could create structures with anisotropic photonic or electrical properties.

6.2 EXPERIMENTAL SECTION

Colloidal silica (Ludox TM-50, 50 wt% suspension in water) sphere was purchased from Sigma-Aldrich, Inc. Both dynamic light scattering (DLS) and transmission electron microscopy (TEM) measurements showed the diameter of the particles, $2R_o \approx 26 \pm 3$ nm (Fig. 6.5.1). The particles are negatively charged with a zeta-potential of -35 $\pm$ 5 mV. Cetyltrimethyl ammonium bromide (CTAB) stabilized AuNRs with length 60 nm and diameter 17 nm were also obtained from Sigma-Aldrich, Inc (Fig. 4.5.1). The concentration of NRs in the stock solution was $\approx$ 2-3 nM, which was diluted thousand times to prepare the solution used in our experiments. Distilled

deionized water was used as a solvent for all experiments. Ludox solution with volume fraction ϕ = 0-0.3 and nanorods in water were prepared in a home built cylindrical glass cell with the top and bottom plate made with borosilicate cover glass of thickness ~0.17 mm. The cell was sealed to prevent evaporation during measurements. Freshly prepared samples were used in all experiments. The viscosity (η_b) of solutions as a function of volume fraction was measured using a falling ball viscometer (Fish-Schurman Corp., NY). All measurements were performed at 20 ^{0}C.

A major obstacle in determining the rod dynamics within a rod/sphere mixture is the strong scattering from the spheres, which can easily overwhelm the signal arising from rods. We took advantage of the two-photon excitation of the gold nanorods. Experiments were performed on a Zeiss inverted microscope (Axiovert S200TV, Carl Zeiss, Inc.) and the sample cell was placed on the mechanical stage attached with the microscope. Near-infrared light from a femtosecond Ti:sapphire laser (Mai Tai, Spectra Physics) of wavelength 800 nm with pulses of width 150 fs at a repetition rate of 80 MHz was focused through a long working distance oil immersion objective (100x, numerical aperture, N.A.=1.25) into the sample. The laser power was kept below 1 mW to avoid photothermal conversion, which can induce heating effect in sample. The fluctuations in photon counts as the gold NPs rotate and move into or out of the laser focus is detected by two single photon counting modulus (Hamamatsu, Inc.). A polarized beam splitter (Thorlabs, Inc.) is placed in front of the detectors. The digital output is recorded and analyzed by an integrated FCS data acquisition system (ISS, Champaign, IL). The cross-correlation function (CCF), $G(\tau)$ of the fluctuation is measured for ~10 mins. The CCF showed clear two stage decays well-separated in time indicating both translational and rotational diffusion of the rods (Fig. 6.2.1). We used:

$$G_{tran}(\tau) = \frac{G(0)}{1+(\frac{8D_T\tau}{\omega_0^2})\sqrt{1+\frac{8D_T\tau}{z_0^2}}}$$ 6.1.2

$$\text{and, } G_{rot}(\tau) = G_r exp(-6D_R\tau)$$ 6.1.3

to fit the CCFs, which give translation (D_T) and rotation (D_R) diffusion coefficients, respectively.[32,97] Here, G(0) is the cross-correlation magnitude at time lag $\tau = 0$ and is inversely proportional to the number of particles within the laser focus. The amplitude of the translational correlation function G_{tran} (τ) depends upon the average number of the particles within the laser focus. The amplitude of rotational correlation function G_{rot} (τ) of the rod depends upon the aspect ratio as well as the excitation and detected polarization state. As the observation volume is a three dimensional Gaussian intensity profile, the $1/e^2$ radius is given by ω_0, whereas it is z_0 in the axial direction. The value of $\omega_0 \approx 0.4$ µm and $z_0 \approx 2$ µm were determined through calibration experiments. Parak *et al.*[129] have used a rough approximation for measuring the focus radius in solution which has different refractive index compared to the solution used for the calibration experiment. According to the approximation: $\omega_{ludox} = \omega_{water}\frac{\eta_{water}}{\eta_{ludox}}$. In our experiment: ω_{water} = 0.4 µm, η_{water} = 1.33 and η_{ludox} = 1.45, which gives ω_{ludox} = 0.37. The maximum error determining the beam width is about 7.5%. So, the change in D is ~15% as D ~ ω_0^2. The statistical deviation in measuring diffusion coefficient is around 20%. So the change in calibration volume can be neglected.
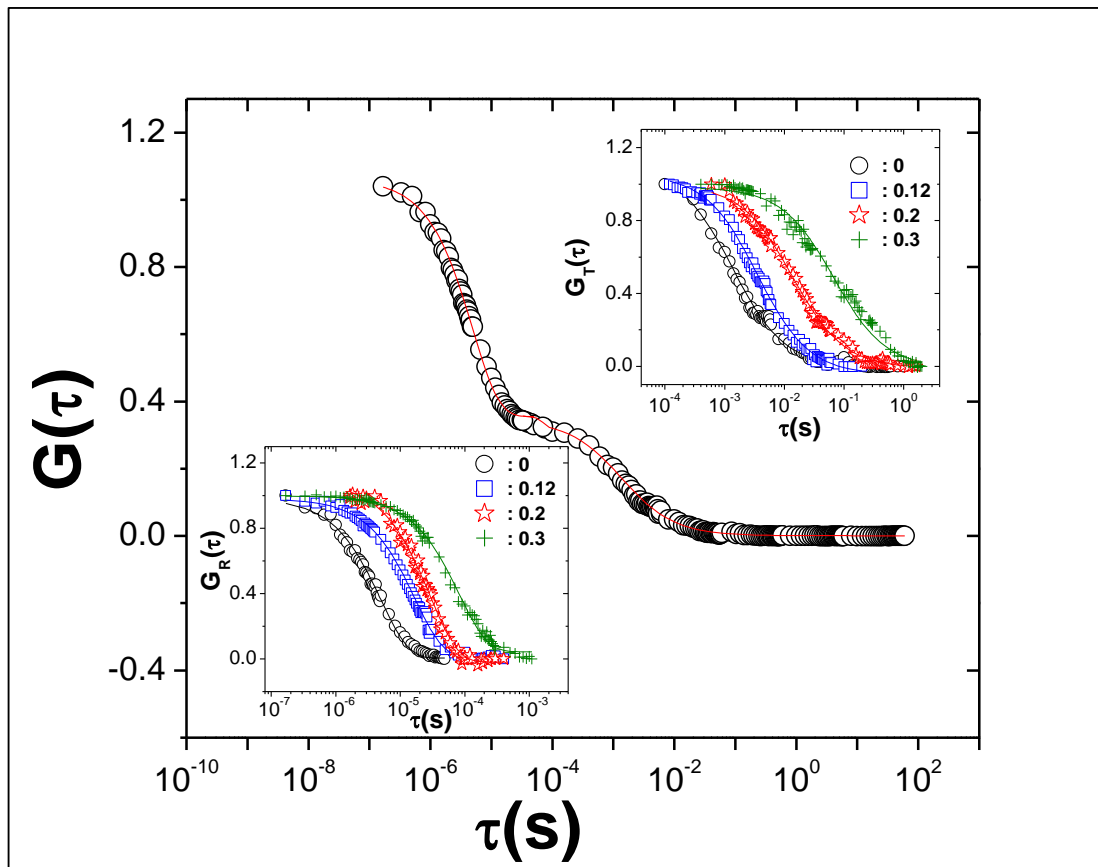
FIGURE 6.2.1: Cross-correlation function, G(τ) with fitting as described in the text showing both the translational and rotational diffusion of the gold nanorods in water (main figure). Rotational (inset bottom) and translational (inset top) cross-correlation curves were shown separately for different volume fractions of Ludox as indicated in the caption. The nanorods concentration was kept at about ~ 1 pM. The imperfect fit of the translation curves are described later.

6.3. RESULTS AND DISCUSSION

Figure 6.2.1 shows a typical cross-correlation function of AuNRs in water. Following the convention used in Ref [32], we used a configuration of [YXY], where the first letter corresponds to excitation polarization and the next two letters correspond to detected

polarizations. Z is the propagation direction of the incident light. From the analysis as described earlier, we obtained D_{T0}=14.6 μm^2/s and D_{R0}=33556 s^{-1}, where the subscript '0' indicates that the measurements were performed in neat solvent. According to various theories of rod diffusion, D_T ~ L^{-1} log (L/d) and D_R ~ L^{-3} log (L/d),[32,33] which indicates extreme sensitivity of D_R on the length (L) of the rod. We used Tirado and Garcia de la Torre's (TT) theory,[6,130] which is most appropriate for shorter rods (i.e., low aspect ratio) to calculate the expected values for rod diffusion from the measured L and d respectively by using TEM. It gave D_{R0}≈ 17900-26000 s^{-1} and D_{T0}≈14-16.5 μm^2/s depending upon the assumed thickness of the CTAB coating (~1-3 nm).[52] In the insets of Fig. 6.2.1 we showed CCFs for translational and rotational diffusion separately for few different concentrations of Ludox spheres. As shown, clearly the time-scale of diffusion increases with the increase of volume fraction consistent with the overall increase of the viscosity of the solution.

6.3.1 TRANSLATIONAL DIFFUSION

A rod can translate along its axis (∥ or 'easy' direction) or perpendicular to it (⊥ or 'hard' direction). In neat solvent an isotropic diffusion is expected, i.e., $D_{T\parallel}/D_{T\perp}$=1,[22] but diffusion anisotropy can be extremely large within a semidilute or concentrated solution.[82] DE theory assumed an extreme situation, where diffusion along the 'hard' direction is completely quenched ($D_{T\perp}$≈0). Along the 'easy' direction, $D_{T\parallel}$ is unaffected by the presence of the other particles. Therefore, $D_{T\parallel}$≈ $D_{T\parallel 0}$. These results, however, are strictly valid for ultrathin rods and within highly concentrated solution. The analysis of our data in neat solvent did not reveal any significant difference between fitting with one-component diffusion or two-component diffusion:

$$G_{tran}(\tau) = \frac{G(0)}{1+(\frac{8D_{Tavg}\tau}{\omega_0^2})} \qquad\qquad 6.1.4$$

$$G_{tran}(\tau) = \frac{G_1(0)}{1+(\frac{8D_{T\parallel}\tau}{\omega_0^2})} + \frac{G_2(0)}{1+(\frac{8D_{T\perp}\tau}{\omega_0^2})} \qquad\qquad 6.1.5$$

as shown in Fig. 6.3.1.1 inset. But, clearly one component fitting is not satisfactory with the increase of concentration as shown by the systematic variation of the residuals (Fig. 6.3.1.1). The CCF can be fitted very well with two-component diffusion, giving a fast ($D_{T\parallel}$) and slow component ($D_{T\perp}$).
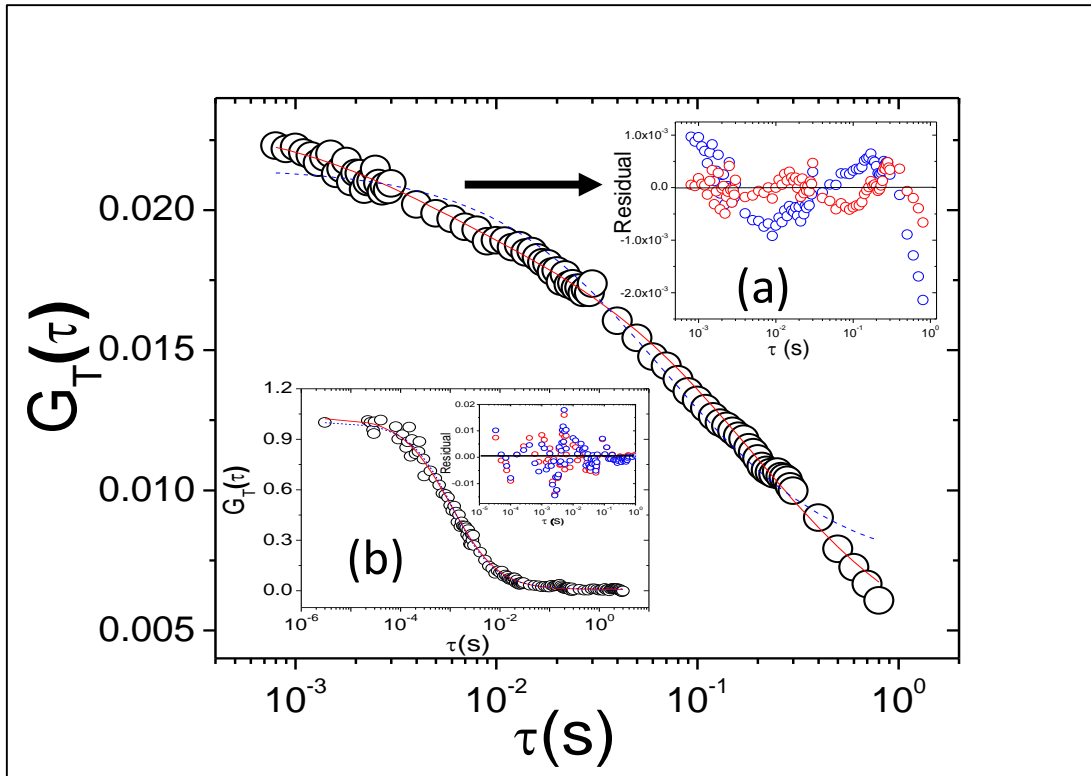
FIGURE 6.3.1.1: The imperfect fit with one-component translation diffusion coefficient is demonstrated. The solution is with Ludox volume fraction $\approx$ 0.3. The dashed line through the points is one component fit ($D_T \approx$ 0.3 μm^2/s) and the solid line is two-component fit ($D_{T\parallel} \approx$ 5 μm^2/s and $D_{T\perp} \approx$ 0.1 μm^2/s). The corresponding residuals are shown in inset (a). Inset (b) showed

one-component (dashed) and two-component (solid) fit of correlation function with residuals in water, which showed no significant differences.

In Figure 6.3.1.2 (top) we plot the two components as a function of the Ludox volume fraction. Both $D_{T\perp}$ and $D_{T\parallel}$ decreases strongly beyond a concentration of ϕ=0.1. Over the whole concentration regime, $D_{T\parallel}$ decreases by a factor of 10, while $D_{T\perp}$ decreases by a factor of ~100. So both components of diffusion showed strong concentration dependence with the diffusion along the 'hard' direction affected more dramatically. The diffusion anisotropy, the ratio of the fast component to slow component ($D_{T\parallel}$/ $D_{T\perp}$) increased by a factor of ~10 as the volume fraction of the spheres is increased from 0 to ~7 spheres/L^3. These results can be compared with Brownian dynamics simulation of rigid rods (aspect ratio =50) within a mixture of similar rods.[131] For a concentration change between 5-50 rods/L^3, observed $D_{T\parallel}$ decreases by about 20%, while $D_{T\perp}$ decreases by a factor of ~5. Obviously, our results showed much significant dependence of $D_{T\parallel}$ and $D_{T\perp}$ on volume fraction. The average value of translational diffusion coefficients, D_{Tavg} was calculated by fitting the CCF's with 2D Gaussian model with two photon excitation: $G_{tran}(\tau) = \dfrac{G(0)}{1+(\frac{8D_{Tavg}\tau}{\omega_0^2})}$, these coefficients are comparable with theoretical value of average translational diffusion coefficients obtained from Stick theory: $D_{Tavg} = \frac{1}{3}\left(D_{T\parallel} + 2D_{T\perp}\right)$ (Fig. 6.5.3).
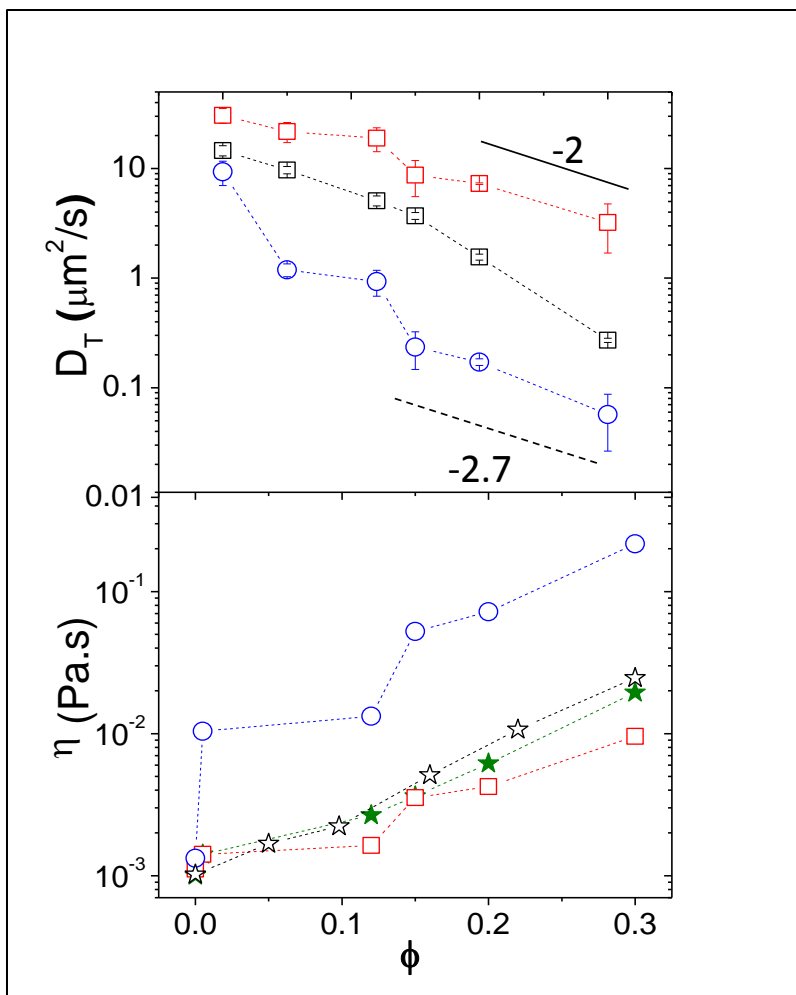
FIGURE 6.3.1.2: (Top) Translational diffusion coefficients along the 'easy' axis ($D_{T\parallel}$, open square) and 'hard' axis ($D_{T\perp}$, open circle) are plotted as a function of Ludox volume fraction (ϕ). The graph also showed the average translation diffusion coefficient of the rods (closed square). The solid and the dashed line have slopes of -2.0 and -2.7, respectively showing the different concentration dependence of $D_{T\parallel}$ and $D_{T\perp}$. (Bottom) The viscosity (η) extracted from translation diffusion showed rod motion along the easy direction (open square) followed closely the bulk viscosity, η_b (closed star) while the motion along the 'hard' direction (open circle) followed much higher nanoviscosity. The nanoviscosity experienced by spherical gold NPs of the similar

size of the diameter of the rod also experienced the same nanoviscosity (open star) as in the 'easy' direction.

We can determine the nanoviscosity which is also known as nanofriction, $\eta_c(\phi)$ the particles experienced from the measured diffusion coefficients.[29,129] We used TT theory as described earlier because it provided good agreement with the measured D_T in the neat solvent. Using this theory, we calculated $\eta_c(\phi)$ experienced by the rods along the 'easy' and 'hard' directions. A small numerical factor is included in the analysis to match the nanoviscosity with the bulk water viscosity at $\phi=0$ and to get isotropic diffusion in neat solvent. The comparison with the bulk viscosity, $\eta_b(\phi)$ is shown in 6.3.1.2 (bottom). It is clear that the diffusion along the 'easy' direction closely followed the bulk viscosity, while the nanoviscosity experienced by the rod in the 'hard' direction is much higher compared to the bulk viscosity. The diameter of the rod (≈ 17 nm) is slightly smaller compared to the Ludox spheres size (≈ 26 nm). The motion along this direction, therefore, involves rearrangement of particles at the length scale of about 20 nm. To verify this statement, we conducted experiments with gold nanospheres (AuNS) of size ~20 nm within the matrix of same Ludox spheres, which was used for nanorod experiments. Our results showed that the AuNS experience the nanoviscosity very close to the viscosity experienced by the AuNRs in the 'easy' direction, supporting this scenario. The long-time diffusion along the 'hard' direction, however, is much slower as observed in Fig. 6.3.1.2. The motion along this direction requires collective diffusion of few particles at the length scale of L. It depends both upon hydrodynamic and interparticle interaction. The hydrodynamic interaction generally slow down the particle mobility with increase of sphere concentration at most length scales. This is also manifested in the concentration dependence of nanoviscosity that we showed in Fig. 6.3.1.2. A power-law fitting indicated that for $\phi > 0.1$, $D_{T\parallel} \sim \phi^{-2}$ and $D_{T\perp} \sim \phi^{-2.7}$. The

significance of these exponents is not clear at present, but it supports the general picture that rod motion is affected by different mechanisms in 'easy' and 'hard' directions.

6.3.2 ROTATIONAL DIFFUSION

The rotation of the rod along its' own axis does not change the relative orientation of the absorption and emission dipoles. So, the experiments are sensitive only to the rotation perpendicular to the major axis and only one rotational diffusion coefficient is measured (D_R). The measured diffusion coefficients as a function of sphere concentration is shown in Fig. 6.3.2.1. The most appropriate for the theoretical analysis is the study by Pecora and Deutch,[132] who extended the DE theory to a semidilute solution of rod (probe)/sphere (matrix) mixture. In their simplified theory, which is an extension of DE theory, the rod is trapped by neighboring spheres and its rotational motion is limited to a space between the rod and the nearest spheres. It naturally gives $D_R \sim n^{-2/3.}$ The restricted rotational diffusion of the confined rods is relaxed by the translation diffusion of the spheres away from the cage, giving the results:

$$D_R^{sphr} \propto \frac{k_B T}{\eta_b(\phi) L^4 R_o\, n^{2/3}}$$

6.1.6

where k_B is Boltzmann constant, T is absolute temperature, $\eta_b(\phi)$ is the solution viscosity, and R_o is the radius of a sphere. Their result is valid in the concentration range such that the sphere concentration is high enough to restrict the rod relaxation to $2\pi\ (Ln^{1/3}) > 1$, but not so high that there is a notable overlap among the spheres, $nR_o^3 < 1$. This theory is also valid for a system where, $R_o \leq L$, so that the cage relaxation is dominated by the motion of the spheres.

We estimated that in our experiments $2\pi(Ln^{1/3}) \approx$ 3-6 and $nR_o^3 \approx$ 0.01-0.07, so we expect the caging idea should be valid. In our experiments, $L \approx 3R_o$, so the rod rotation is dominated by the translational diffusion of the spheres away from the rod. A comparison with this theory is

shown in Fig. 6.3.2.1 with a numerical prefactor = 1, which showed a stronger dependence on ϕ and higher disagreement at lower concentration compared to the expectation from caging theory. The theory assumed that the rotational relaxation is dominated by the bulk viscosity of the matrix, which governs the self-diffusion of the spheres. A better agreement with theory is obtained if we assume that the translational diffusion of the rods along the 'easy' direction breaks up the cage. This is justified as this motion is the fastest as shown in Fig. 6.3.2.1 and will, therefore, be the most dominant mechanism of cage relaxation. Substituting the corresponding nanoviscosity gives a better agreement with the rotational diffusion.

The two lowest volume fractions still showed significant deviation from the theory. In fact, diffusion is found to be much slower compared to the expectation from either the bulk viscosity or nanoviscosity. For these two lowest concentrations studied, there are expected to be only 1-3 particles/L^3 present. So caging is not expected to be significant. But we have not considered yet the ordering of the Ludox spheres around the rods. The spheres are negatively charged as the zeta-potential measurements showed. The bare gold nanorods are negatively charged as well, but there is a CTAB coating on the top of the particles, which formed during their synthesis.
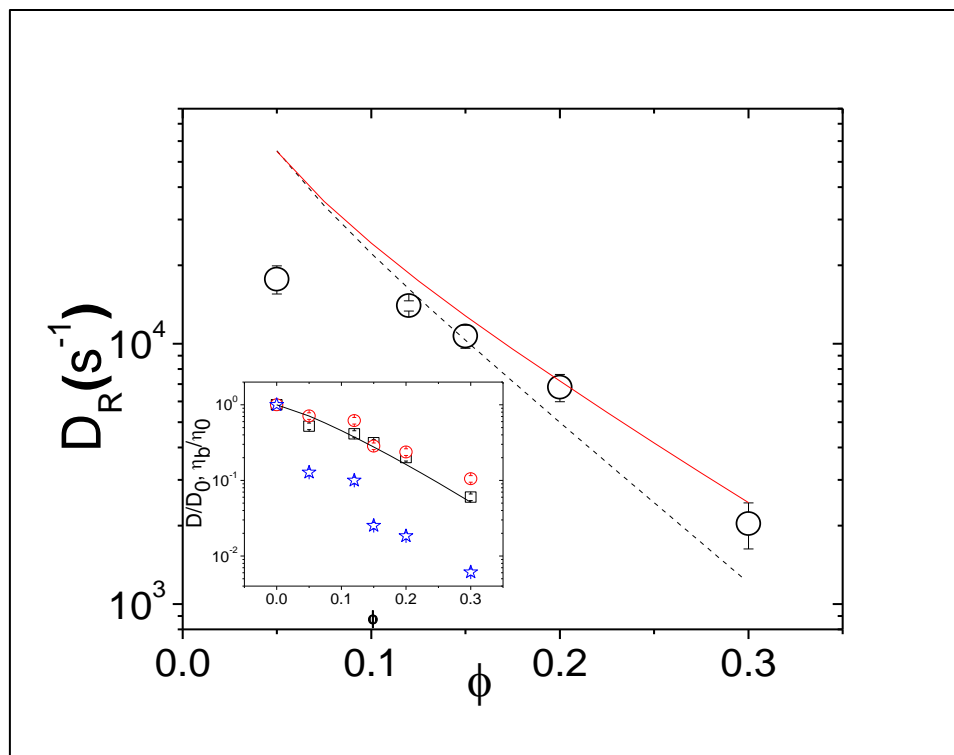
FIGURE 6.3.2.1: The rotational diffusion coefficient vs. volume fraction of Ludox. The dashed line is fit with using Pecora-Deutch theory with bulk viscosity η_b (ϕ). The solid line is using the same theory, but with nanoviscosity that the rods experienced along the 'easy' direction ($\eta_{T\parallel}$). (Inset) Normalized diffusion coefficients and normalized bulk viscosity showing that both $D_{T\parallel}$ (circles), D_R (square) followed the bulk viscosity (—), while $D_{T\perp}$ (stars) decreased much sharply with respect to the volume fraction of Ludox.

It is believed that the coating consisted of a bilayer, which if perfect, will expose positively charged amino groups at the surface.[133] Even if the bilayer is not perfect,[104] it will have patches of positively charged regions with some exposed hydrophobic groups at the surface. The presence of positively charged regions can enhance the ordering of the spheres around the rods and increase the effective sphere density near the particles. Because of the local nature of the rotational motion, this might cause a slowdown of the rotational diffusion compared

to the expectation from caging theory. In spite of caging there is no aggregation between the spheres and rods because that would have caused much dramatic slowdown in diffusions (Fig. 6.5.2 and Fig. 6.5.4). The Fig. 6.3.2.1 (inset) summarizes the data, which showed normalized plot of diffusion coefficients and viscosity vs. volume fraction. The ratio $D_{T\parallel}/ D_{T\parallel 0}$ followed the same concentration dependence of normalized bulk viscosity, η_{b0}/η_b. The diffusion along the 'hard' axis has stronger concentration dependence than the bulk viscosity, while the ratio D_R/D_{R0} can be best explained by considering that cage relaxation occurs through the rod motion along the 'easy' axis.

6.4 CONCLUSIONS

We investigated a poorly understood problem of anisotropic particle diffusion within a mixture of spherical particles. This situation arises in diverse areas ranging from self-assembly to bioengineering. For anisotropic particles we used short gold nanorods of aspect ratio ~4 and two-photon excitation to study their dynamics within a crowded solution of Ludox spheres. We found significant diffusional anisotropy for translational motion of the rod. Though the motion along the rod axis followed closely to the bulk viscosity, the motion perpendicular to the rod axis is significantly retarded. These features have been predicted for ultrathin rods both in theories and simulations. Our experimental results provided a direct quantitative test of these predictions. The rotation of the rods closely followed the modified Doi-Edward caging theory as developed by Pecora and Deutch, but by taking into the fastest relaxation mechanism that breaks the cage.

6.5 SUPPORTING INFORMATION
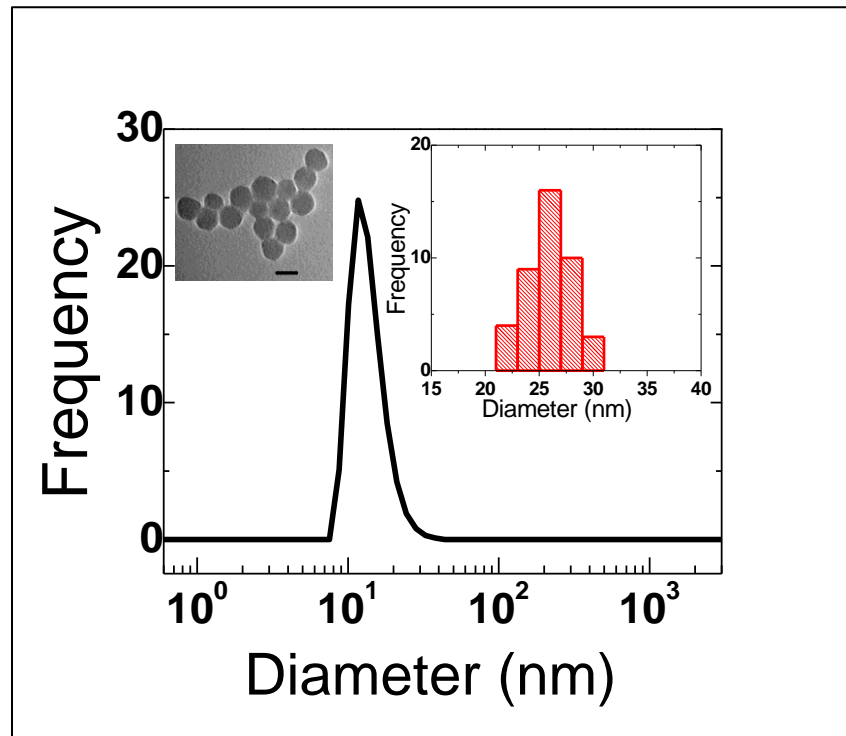
FIGURE 6.5.1: Size distribution of silica nanoparticle obtained from dynamic light scattering (DLS) measurement with a mean diameter 24 nm, and showed no sign of any agglomeration; Left inset: shows a representative TEM micrograph with 20 nm scale bar; Right inset: histogram of size distribution obtained from TEM with mean diameter of 26 ± 3 nm. The average size provided by the manufacturer was 22 nm.
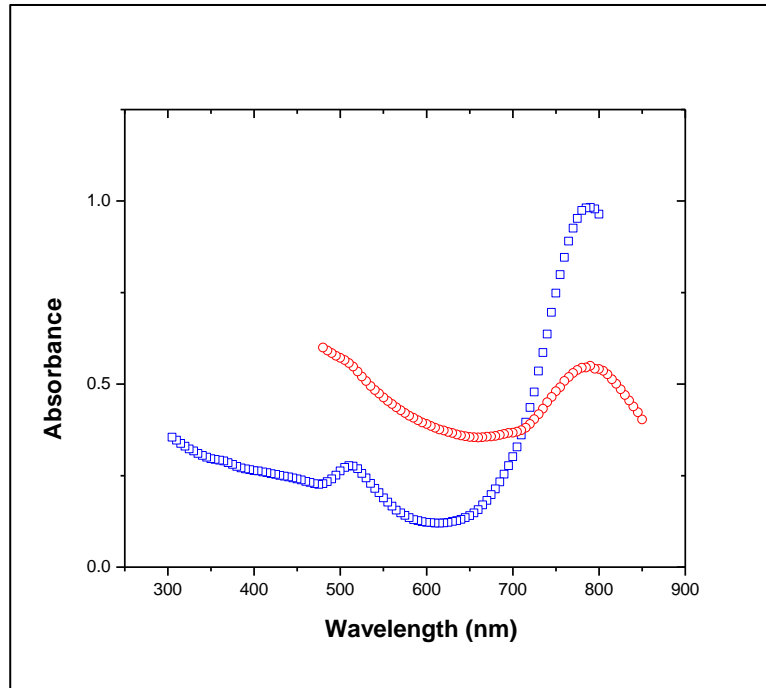
FIGURE 6.5.2: UV-vis spectra of AuNR in water (open square) with two distinct peaks at 790

nm and 510 nm. The peak at 790 nm depends upon the aspect ratio of the rod. UV-vis spectra for

AuNR in Ludox (open circle) for the highest volume fraction of silica spheres with peak at 787

nm.
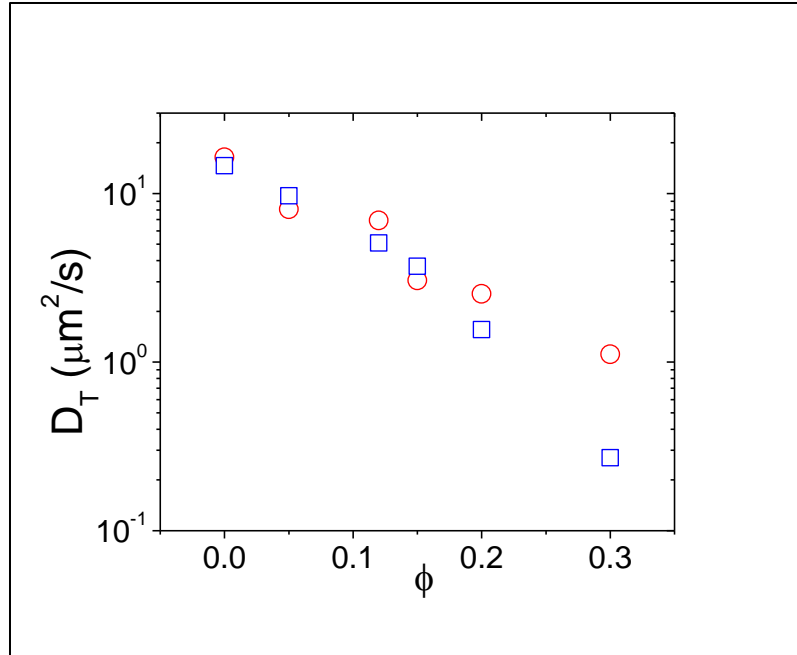
Figure 6.5.3: The theoretical translational diffusion coefficients using Stick theory (open circle) and the experimental value of translational diffusion coefficients (open square) from the CCF fitted with 2D Gaussian model are plotted as a function of Ludox concentrations.
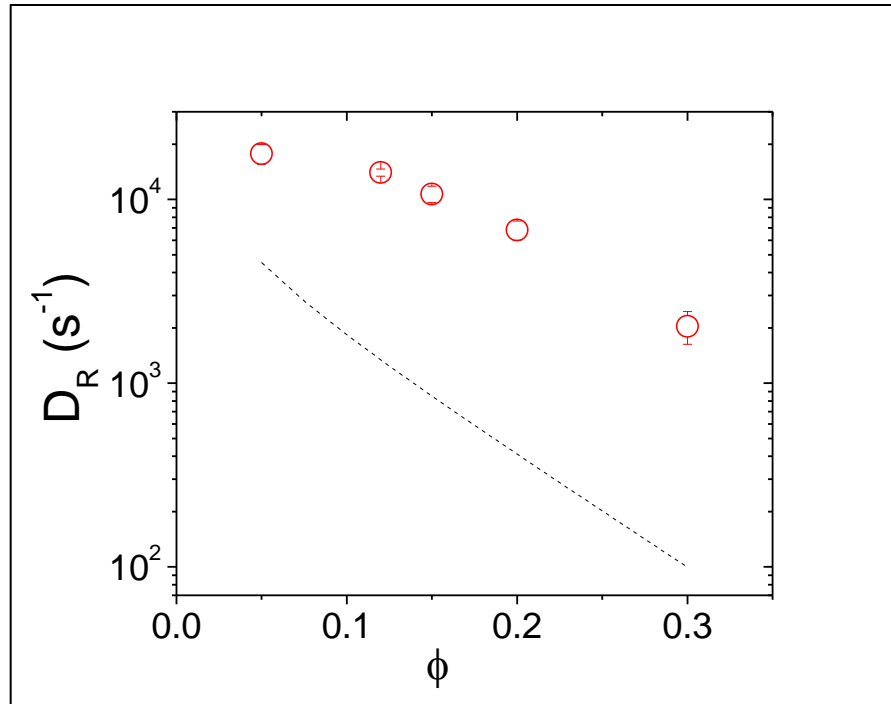
FIGURE 6.5.4: The rotational diffusion coefficients vs. volume fraction of Ludox. Experimental value of rotational diffusion coefficients were plotted as a function of ludox volume fractions (open circle). The dashed line (black) is fit using Pecora-Deutch theory with bulk viscosity η_b (ϕ), where we have considered that one monolayer of silica sphere will stick to rod surface due to electrostatic interaction i.e. L = 112 nm and d = 69 nm.

CHAPTER 7

DYNAMICS OF NANOSPHERES IN BIOPOLYER SOLUTIONS

7.1 INTERACTION AND DIFFUSION OF GOLD NANOPARTICLES IN BOVINE SERUM ALBUMIN SOLUTIONS

The following material was originally published in Applied Physics Letters (2013)[51] that I have co-authored.

The following is the summery of the research publication, that I have co-authored. Gold nanoparticles posses the potential for therapeutic and diagnostic applications[89,134,135] because of their non-toxicity, size-dependent properties, and their ability to be functionalized. The interaction of nanoparticles with biomolecules in complex biological fluids has attracted substantial attention.[34-36] It has been proved experimentally that nanoparticles when exposed to protein can become coated by the protein forming a 'corona' that surrounds that nanoparticles and shield their original surface properties.[37] As the affinity of a certain protein to bind to a nanoparticles surface is determined by the nanoparticles size, shape and surface chemistry,[52,136] it is important to study the interaction of protein with nanometer sized particles. For these research project bovine serum albumin (BSA) protein has been used as a model protein. Gold nanoparticles (AuNPs) with radius 2.5-10 nm were particularly chosen to study the interaction with BSA as the size range would be potentially useful in the areas ranging from biophysics and drug delivery.[37,135,137-139]

Fluorescence correlation spectroscopy measurements were conducted for tannic acid stabilized gold nanoparticles of radius 2.5, 5 and 10 nm in many different concentrations of BSA (0.1 μM to 10 mM) in a phosphate buffer (pH 7.0). A number of autocorrelation functions (ACF) were collected. Figure 7.1.1 shows a representative ACF's collected by FCS for AuNP (R=2.5

nm) diffusing in different concentrations of BSA and plotted versus logarithmic time lag. The ACF's were fitted with the following model:

$$G(\tau) = \frac{< \delta F(t).\delta F(t+\tau) >}{<F(t)>^2} \qquad 7.1.1$$

$$G(\tau) = \frac{G(0)}{1+(\frac{8D\tau}{\omega_0^2})\sqrt{1+(\frac{8D\tau}{z_0^2})}} \qquad 7.1.2$$

where G(0) is the magnitude of the autocorrelation function at short time which is inversely proportional to the number of particles within the laser focus ω_0 and z_0 are the half-width and half-height of the laser focus. The value of ω_0 and z_0 are determined by calibration experiments.
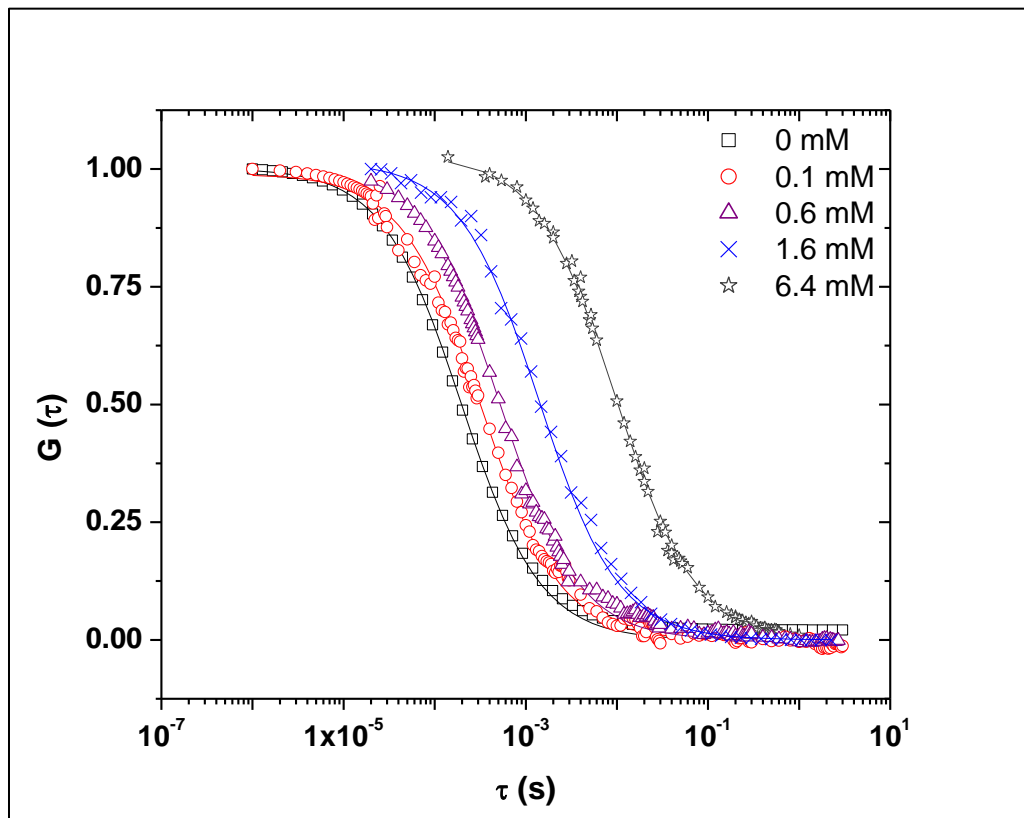
FIGURE 7.1.1: Normalized autocorrelation curves for AuNP (R= 2.5 nm) diffusing in BSA

solution in phosphate buffer at various protein concentrations. Solid lines are fit to the curves using Eq. 7.1.2.

Transmission electron microscopy (TEM) measurements was done to confirm size of the NPs (Fig. 7.1.2).
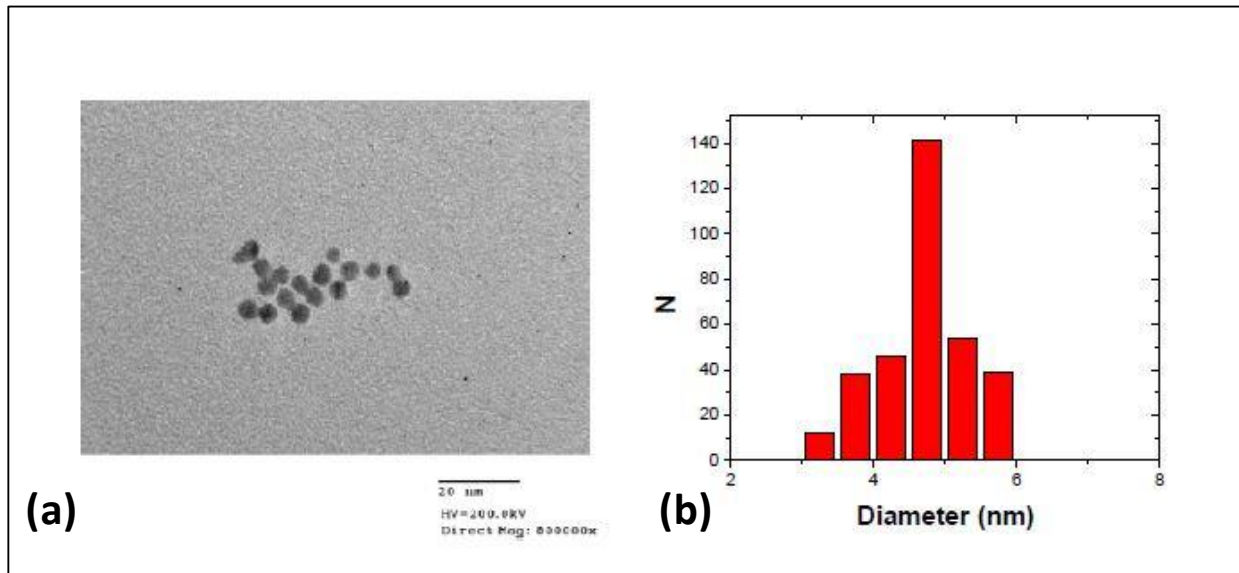
FIGURE 7.1.2: (a) TEM image of AuNPs deposited on carbon film magnified 800 000×. (b) A histogram obtained by measuring the diameters of AuNPs, where the average diameter measured is 4.7 ± 0.6 nm.

Diffusion co-efficient (D) can be calculated from the ACF by using Eq. (7.1.1). Figure 7.1.3 shows D as a function of protein concentration. The decrease in diffusion co-efficient for NPs with the increase in BSA concentration was observed which was expected form the theory. The diffusion data are fitted with Phillies equation of stretched exponential function: $D/D_0 = \exp(-\beta c^\nu)$, where D_0 is the diffusion co-efficient of the AuNP in the limit of low protein concentration, β and ν are adjustable parameters. The fitting was reasonably good and the value of exponent ν was close to 1 as expected.[23,100,114]

TABLE 7.1.1: Translational diffusion coefficient (D) of AuNPs obtained by autocorrelation analysis, and hydrodynamic radius (R_h) calculated using SE relation in absence and presence of BSA

AuNP Radius(nm)	DAuNP (µm2/s)	DAuNP+BSA (µm2/s)	Rh AuNP (nm)	RhAuNP+BSA (nm)
2.5	87±3.5	26.0±0.8	2.51±0.1	5.59±0.2
5	39±1.8	16.86±1.1	5.5±0.3	8.63±0.5
10	21±0.6	10.4±0.5	10.4±0.3	13.9±0.7
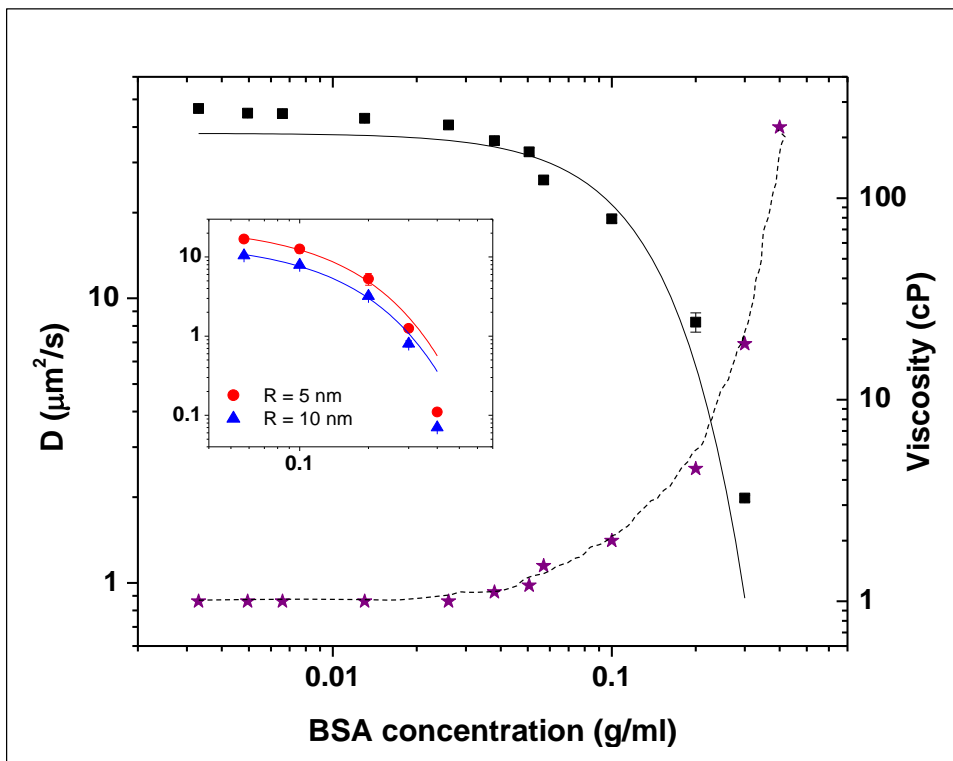
FIGURE 7.1.3: Diffusion coefficient of R = 2.5 nm AuNPs as a function of protein concentration. The inset shows the measured diffusion for 5 and 10 nm AuNPs at higher concentrations of BSA. Also shown (stars) viscosity as a function of BSA concentration.

The hydrodynamic radius of NPs were calculated from the measured diffusion co-efficient using SE equation. The change in hydrodynamic radius was observed in the absence and presence of BSA. The average change in NP hydrodynamic radius for all concentrations is $\Delta R = 3.8 \pm 0.5$ nm which corresponds to BSA monolayer formation. In order to check for multilayer formation FCS measurements were done for higher BSA concentrations (0.8 mM – 10 mM). But no multilayer formation was observed for three different size NPs which indicates that adsorption of BSA on AuNPs is size independent. The hydrodynamic radius of NP as a function of protein concentration can be expressed as follows from the concept of Rocker et al[49]:

$$R_h([BSA]) = R_h(0) \sqrt[3]{1 + \frac{c\, N_{max}}{1 + \left(\frac{K_D}{[BSA]}\right)^n}}$$ 7.1.3

where K_D is the dissociation constant which quantify the NP – protein interaction. N_{max} is the maximum number of protein molecules adsorbed to the NP and n is the Hill co-efficient. The best fit yields $K_D = 78.6 \pm 9.5$ µM, n = 0.63 ± 0.03. The value of Hill coefficient is < 1 indicates anticooperative binding which demonstrates the absence of multilayer formation. The data are also fitted with Langmuir binding isotherm (n = 1) which indicates multilayer formation and the dissociative co-efficient for Langmuir fit is $K_D = 14.6 \pm 4.3$. The maximum number of protein molecules adsorbed per 2.5 nm radius AuNP from the fit is $N_{max} = 8.4 \pm 1$ which is reasonably good agreement with the theoretical value of $N_{max} = 8.5$.
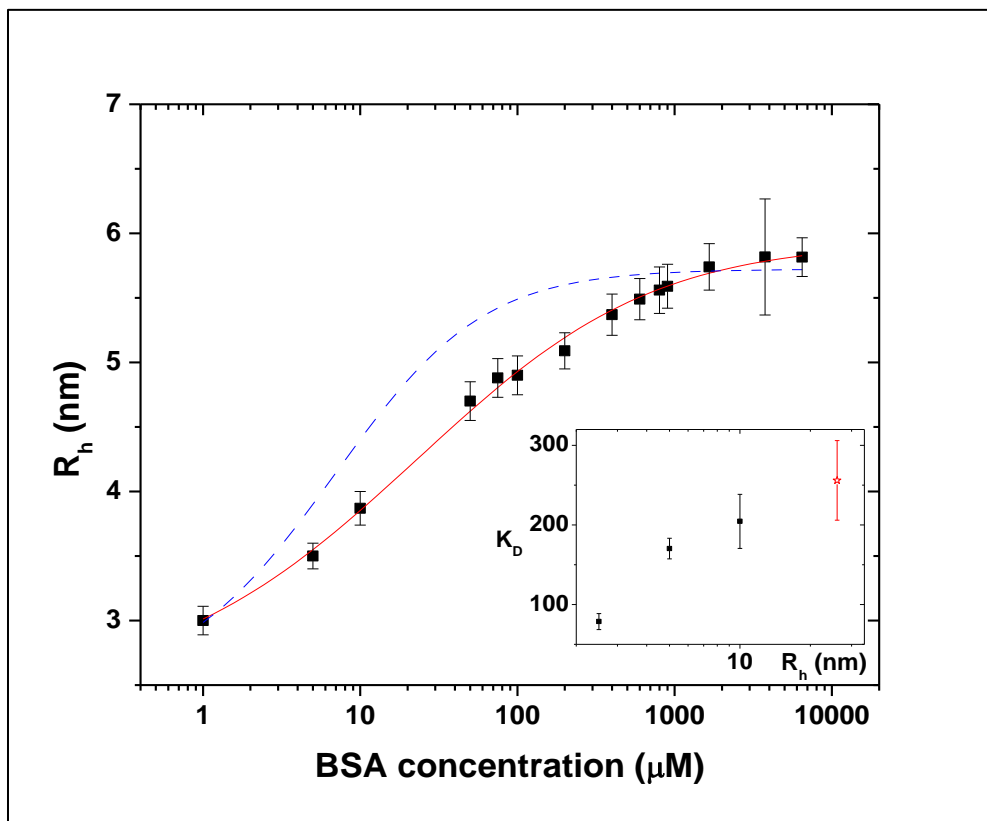
FIGURE 7.1.4: Hydrodynamic radii of NPs plotted as a function of BSA concentration. Red solid line represents fit of anti cooperative binding model, and blue dashed line shows comparison to Langmuir binding isotherm fitted to first and last 30 percent of data points. The conversion of concentration units is as follows $[BSA]_{g/ml} = [BSA]_{\mu M} * M_w * 10^{-9}$, where M_w is the molecular weight of BSA and is equal to 66,430 g/mol. The inset shows K_D as a function of the hydrodynamic radius R_h.

The value of dissociation constant, K_D increases with the increase in size of NPs implies stronger interaction between small NPs and BSA, which eventually indicates the adsorption of protein on NPS is due to Ligand exchange mechanism suggested by Tsai *et al.*[109] rather than electrostatic interaction suggested by other groups.[116,140]

The adsorption of BSA protein monolayer on the small sized AuNPs was demonstrated in this project by performing FCS. Multilayer protein formation was not observed even for significant higher concentration of BSA. The adsorption was described by the anticooperative binding model. These results will be important in understanding the nanoparticle motion in complex fluids which will be eventually helpful in the areas of bio diagnostic and drug delivery.

CHAPTER 8

CONCLUSIONS

The experiments comprising in my dissertation have focused on investigating the dynamics of anisotropic gold nanoparticles in polymeric and colloidal systems. Understanding the interaction of anisotropic nanoparticles with macromolecules (polymers, proteins, and colloids) has technological as well as biomedical interests such as developing high performance polymeric materials, nano-template surfaces, and effective drug delivery vehicles. For the investigations, fluorescence correlation spectroscopy (FCS) was performed, which can offer structural and dynamical information about these systems at shorter length scales. These experiments allowed us to report important observations in Chapters 4 – 6 and my collaborative work with Dr. Kohli in Chapter 7.

Nanoparticles are being widely used as drug carrier and therapeutic agents. In many cases, however, the particles have to cross the mucus gel, which can act as a formidable barrier to nanoparticles drug-delivery systems. Mucus is a slippery secretion produced from cells found in mucus glands, which act as a lubricant. This barrier is important for humans as well as animals as it protects vulnerable surfaces in the lung, intestinal, reproductive tissues, and eye from invasion by bacteria, viruses, allergens and irritants. However, the high viscoelasticity and adhesivity of mucus can cause problem for drug delivery. The mesh size of mucin fibers within mucus in ~ 1μm, i.e. larger particles will have difficulty in penetrating mucus. But the pore size can decrease much farther in the various disease states, such as asthma, cystic fibrosis, etc.

Our current research involved using gold NPs of differnt sizes and shapes to investigate their penetration through reconstituted mucus gel.

RERERENCES

1.   P.-G. de Gennes, Rev. Mod. Phys. **64** (3), 645 (1992).

2.   R. A. Jones, *Soft condensed matter*. (Oxford University Press, 2002).

3.   I. W. Hamley, *Introduction to soft matter: Synthetic and biological self-assembling materials*. (John Wiley & Sons, 2013).

4.   M. Rubinstein and R. H. Colby, *Polymer physics*. (OUP Oxford, 2003).

5.   R. Vasanthi, S. Bhattacharyya and B. Bagchi, J. Chem. Phys. **116** (3), 1092-1096 (2002).

6.   M. M. Tirado and J. G. de la Torre, J. Chem. Phys. **71** (6), 2581-2587 (1979).

7.   M. M. Tirado, C. L. Martinez and J. G. de la Torre, J. Chem. Phys. **81** (4), 2047-2052 (1984).

8.   J. G. De La Torre and C. LOPEZ, Biopolymers **23**, 611-615 (1984).

9.   S. Broersma, J. Chem. Phys. **32** (6), 1632-1635 (1960).

10.   S. Broersma, J. Chem. Phys. **32** (6), 1626-1631 (1960).

11.   J. Pérez-Juste, I. Pastoriza-Santos, L. M. Liz-Marzán and P. Mulvaney, Coordin. Chem. Rev. **249** (17), 1870-1901 (2005).

12.   H. Liao and J. H. Hafner, Chem. Mater. **17** (18), 4636-4641 (2005).

13.   T. B. Huff, L. Tong, Y. Zhao, M. N. Hansen, J.-X. Cheng and A. Wei, Nanomedicine **2** (1), 125-132 (2007).

14.   L. Wang, Y. Liu, W. Li, X. Jiang, Y. Ji, X. Wu, L. Xu, Y. Qiu, K. Zhao and T. Wei, Nano Lett. **11** (2), 772-780 (2010).

15.   M. J. Solomon and Q. Lu, Curr. Opin. Colloid In. **6** (5), 430-437 (2001).

16.   J. Liu, L. Zhang, D. Cao and W. Wang, Phys. Chem. Chem. Phys. **11** (48), 11365-11384 (2009).

17.   L.-H. Cai, S. Panyukov and M. Rubinstein, Macromolecules **44** (19), 7853 (2011).

18.   R. Cukier, Macromolecules **17** (2), 252-255 (1984).

19.   B. Amsden, Macromolecules **32** (3), 874-879 (1999).

20.   A. R. Altenberger and M. Tirrell, J. Chem. Phys. **80** (5), 2208-2213 (1984).

21.   A. Ogston, B. Preston and J. Wells, presented at the Proceedings of the Royal Society of London A: Mathematical, Physical and Engineering Sciences, 1973 (unpublished).

22.   F. B. Wyart and P. De Gennes, Eur. Phys. J. E **1** (1), 93-97 (2000).

23.   G. D. Phillies, Macromolecules **20** (3), 558-564 (1987).

24.   G. D. Phillies and D. Clomenil, Macromolecules **26** (1), 167-170 (1993).

25.   L.-H. Cai, S. Panyukov and M. Rubinstein, Macromolecules **48** (3), 847-862 (2015).

26.   J. Liu, D. Cao and L. Zhang, J. Phys. Chem. C **112** (17), 6653-6661 (2008).

27.   K. Kremer and G. S. Grest, J. Chem. Phys. **92** (8), 5057-5086 (1990).

28.   V. Ganesan, V. Pryamitsyn, M. Surve and B. Narayanan, J. Chem. Phys. **124** (22), 221102 (2006).

29.   R. Holyst, A. Bielejewska, J. Szymański, A. Wilk, A. Patkowski, J. Gapiński, A. Żywociński, T. Kalwarczyk, E. Kalwarczyk and M. Tabaka, Phys. Chem. Chem. Phys. **11** (40), 9025-9032 (2009).

30.   X. Ye, P. Tong and L. Fetters, Macromolecules **31** (19), 6534-6540 (1998).

31.   I. Kohli and A. Mukhopadhyay, Macromolecules **45** (15), 6143-6149 (2012).

32.   J. M. Tsay, S. Doose and S. Weiss, J. Am. Chem. Soc. **128** (5), 1639-1647 (2006).

33.   R. Cush, D. Dorman and P. S. Russo, Macromolecules **37** (25), 9577-9584 (2004).

34.   B. Wang, L. Zhang, S. C. Bae and S. Granick, P. Natl. A. Sci. **105** (47), 18171-18175 (2008).

35.   D. Zhang, O. Neumann, H. Wang, V. M. Yuwono, A. Barhoumi, M. Perham, J. D. Hartgerink, P. Wittung-Stafshede and N. J. Halas, Nano Lett. **9** (2), 666-671 (2009).

36.   M. Mahmoudi, I. Lynch, M. R. Ejtehadi, M. P. Monopoli, F. B. Bombelli and S. Laurent, Chem. Rev. **111** (9), 5610-5637 (2011).

37.   K. Vangala, F. Ameer, G. Salomon, V. Le, E. Lewis, L. Yu, D. Liu and D. Zhang, J. Phys. Chem. C **116** (5), 3645-3652 (2012).

38.   E. Casals and V. F. Puntes, Nanomedicine **7** (12), 1917-1930 (2012).

39.   L. Tong, Y. Zhao, T. B. Huff, M. N. Hansen, A. Wei and J. X. Cheng, Adv. Mater. **19** (20), 3136-3141 (2007).

40.   X. Huang, S. Neretina and M. A. El-Sayed, Adv. Mater. **21** (48), 4880 (2009).

41.   D. Solis Jr, W.-S. Chang, B. P. Khanal, K. Bao, P. Nordlander, E. R. Zubarev and S. Link, Nano Lett. **10** (9), 3482-3485 (2010).

42.   D. C. Carter and J. X. Ho, Adv. Protein Chem. **45** (45), 153-203 (1994).

43.   J. X. Ho, E. W. Holowachuk, E. J. Norton, P. D. Twigg and D. C. Carter, Eur. J. Biochem. **215** (1), 205-212 (1993).

44.   D. S. Goodman, J. Am. Chem. Soc. **80** (15), 3892-3898 (1958).

45.   J. Figge, T. Rossing and V. Fencl, J. Lab. Clin. Med. **117** (6), 453-467 (1991).

46.   T. Peters Jr, *The Plasma Proteins 2E V1: Structure, Function, and Genetic Control* **1**, 133 (2012).

47.   S. Era and M. Sogami, J. Pept. Res. **52** (6), 431-442 (1998).

48.   X. M. He and D. C. Carter, Nature **358**, 209-215 (1992).

49.   C. Röcker, M. Pötzl, F. Zhang, W. J. Parak and G. U. Nienhaus, Nat. Nanotechnol. **4** (9), 577-580 (2009).

50.   S. Dominguez-Medina, S. McDonough, P. Swanglap, C. F. Landes and S. Link, Langmuir **28** (24), 9131-9139 (2012).

51.   I. Kohli, S. Alam, B. Patel and A. Mukhopadhyay, Appl. Phys. Lett. **102** (20), 203705 (2013).

52.   S. Chakraborty, P. Joshi, V. Shanker, Z. Ansari, S. P. Singh and P. Chakrabarti, Langmuir **27** (12), 7722-7731 (2011).

53.   D. Langevin and F. Rondelez, Polymer **19** (8), 875-882 (1978).

54.   A. Ogston, T. Faraday Soc. **54**, 1754-1757 (1958).

55.   C. N. Onyenemezu, D. Gold, M. Roman and W. G. Miller, Macromolecules **26** (15), 3833-3837 (1993).

56.   M. Doi and S. F. Edwards, J. Chem. Soc. Farad. T. 2 **74**, 918-932 (1978).

57.   M. Doi and S. Edwards, J. Chem. Soc. Farad. T. 2 **74**, 560-570 (1978).

58.   T. Odijk, Macromolecules **16** (8), 1340-1344 (1983).

59.   T. Odijk, Macromolecules **17** (3), 502-503 (1984).

60.   G. Keep and R. Pecora, Macromolecules **18** (6), 1167-1173 (1985).

61.   M. Doi, I. Yamamoto and F. Kano, J. Phys. Soc. Jpn. **53** (9), 3000-3003 (1984).

62.   M. Doi, J. Phys.-Paris **36** (7-8), 607-611 (1975).

63.   M. Fixman, Phys. Rev. Lett. **55** (22), 2429 (1985).

64.   D. Frenkel and J. Maguire, Mol. Phys. **49** (3), 503-541 (1983).

65.   J. Odell, E. Atkins and A. Keller, J. Polym. Sci. Pol. Lett. **21** (4), 289-300 (1983).

66.   Z. Pu and W. Brown, Macromolecules **22** (2), 890-896 (1989).

67.   G. D. Phillies, Macromolecules **28** (24), 8198-8208 (1995).

68.   N. Nemoto, T. Inoue, Y. Makita, Y. Tsunashima and M. Kurata, Macromolecules **18** (12), 2516-2522 (1985).

69.   C. Lellig, J. Wagner, R. Hempelmann, S. Keller, D. Lumma and W. Härtl, J. Chem. Phys **121** (14), 7022-7029 (2004).

70.   R. Cush, P. S. Russo, Z. Kucukyavuz, Z. Bu, D. Neau, D. Shih, S. Kucukyavuz and H. Ricks, Macromolecules **30** (17), 4920-4926 (1997).

71.   G. H. Koenderink, D. Aarts and A. P. Philipse, J. Chem. Phys. **119** (8), 4490-4499 (2003).

72.   J. Phalakornkul, A. Gast and R. Pecora, J. Chem. Phys. **112** (14), 6487-6494 (2000).

73.   K. M. Berland, P. So and E. Gratton, Biophys. J. **68** (2), 694 (1995).

74.   O. Krichevsky and G. Bonnet, Rep. Prog. Phys. **65** (2), 251 (2002).

75.   D. Magde, E. Elson and W. W. Webb, Phys. Rev. Lett. **29** (11), 705 (1972).

76.   H.-X. Zhou, G. Rivas and A. P. Minton, Ann. Rev. Biophys. **37**, 375 (2008).

77.   B. J. Berne and R. Pecora, *Dynamic light scattering: with applications to chemistry, biology, and physics*. (Courier Corporation, 2000).

78.   P. T. Callaghan, *Principles of nuclear magnetic resonance microscopy*. (Oxford University Press, 1993).

79.   D. Harvey, *Modern analytical chemistry*. (McGraw-Hill New York, 2000).

80.   E. Haustein and P. Schwille, Annu. Rev. Biophys. Biom. **36**, 151-169 (2007).

81.   W. Denk, J. H. Strickler and W. W. Webb, Science **248** (4951), 73-76 (1990).

82.   S. Alam and A. Mukhopadhyay, Macromolecules **47** (19), 6919-6924 (2014).

83.   A. Tuteja, M. E. Mackay, S. Narayanan, S. Asokan and M. S. Wong, Nano Lett. **7** (5), 1276-1281 (2007).

84.   D. Chen, E. Weeks, J. C. Crocker, M. Islam, R. Verma, J. Gruber, A. Levine, T. C. Lubensky and A. Yodh, Phys. Rev. Lett. **90** (10), 108301 (2003).

85.   Y. Cu and W. M. Saltzman, Nat. Mater. **8** (1), 11 (2009).

86.   U. Yamamoto and K. S. Schweizer, J. Chem. Phys **135** (22), 224902 (2011).

87.   V. Pryamitsyn and V. Ganesan, Phys. Rev. Lett. **100** (12), 128302 (2008).

88.   K. Khanvilkar, M. D. Donovan and D. R. Flanagan, Adv. Drug Deliver. Rev. **48** (2), 173-193 (2001).

89.   N. J. Durr, T. Larson, D. K. Smith, B. A. Korgel, K. Sokolov and A. Ben-Yakar, Nano Lett. **7** (4), 941-945 (2007).

90.   N. N. Sanders, S. C. DE SMEDT, E. Van Rompaey, P. Simoens, F. De Baets and J. Demeester, Am. J. Resp. Crit. Care **162** (5), 1905-1911 (2000).

91.   E. E. Connor, J. Mwamuka, A. Gole, C. J. Murphy and M. D. Wyatt, Small **1** (3), 325-327 (2005).

92.   P. K. Jain, X. Huang, I. H. El-Sayed and M. A. El-Sayed, Accounts Chem. Res. **41** (12), 1578-1586 (2008).

93.   M. Haghighi, M. A. Plum, G. Gantzounis, H.-J. r. Butt, W. Steffen and G. Fytas, J. Phys. Chem. C **117** (16), 8411-8419 (2013).

94.   N. G. Khlebtsov, A. G. Melnikov, V. A. Bogatyrev, L. A. Dykman, A. V. Alekseeva, L. A. Trachuk and B. N. Khlebtsov, J. Phys. Chem. B **109** (28), 13578-13584 (2005).

95.   X. Ye, P. Tong and L. Fetters, Macromolecules **31** (17), 5785-5793 (1998).

96.   Z. Xiao, M. Gupta, G. Baltas, T. Liu, H. G. Chae and S. Kumar, Polymer **53** (22), 5069-5077 (2012).

97.   A. Tcherniak, S. Dominguez-Medina, W.-S. Chang, P. Swanglap, L. S. Slaughter, C. F. Landes and S. Link, J. Phys. Chem. C **115** (32), 15938-15949 (2011).

98.   B. Zhang, T. Lan, X. Huang, C. Dong and J. Ren, Anal. Chem. **85** (20), 9433-9438 (2013).

99.   S. Egorov, J. Chem. Phys. **134** (23), 234509 (2011).

100.   J. Won, C. Onyenemezu, W. G. Miller and T. P. Lodge, Macromolecules **27** (25), 7389-7396 (1994).

101.   P. De Gennes, *Scaling Concepts in Polymer Physics.* (Cornell University 1979).

102.   N. Ziębacz, S. A. Wieczorek, T. Kalwarczyk, M. Fiałkowski and R. Hołyst, Soft Matter **7** (16), 7181-7186 (2011).

103.   C. D. Chapman, K. Lee, D. Henze, D. E. Smith and R. M. Robertson-Anderson, Macromolecules **47** (3), 1181-1186 (2014).

104.   S. Alam and A. Mukhopadhyay, J. Phys. Chem. C **118** (47), 27459-27464 (2014).

105.   S. C. Glotzer and M. J. Solomon, Nat. Mater. **6** (8), 557-562 (2007).

106.   X. Huang, I. H. El-Sayed, W. Qian and M. A. El-Sayed, J. Am. Chem. Soc. **128** (6), 2115-2120 (2006).

107.   W. Jiang, B. Y. Kim, J. T. Rutka and W. C. Chan, Nat. Nanotechnol. **3** (3), 145-150 (2008).

108.   M. Mahmoudi, S. E. Lohse, C. J. Murphy, A. Fathizadeh, A. Montazeri and K. S. Suslick, Nano Lett. **14** (1), 6-12 (2013).

109.   D.-H. Tsai, F. W. DelRio, A. M. Keene, K. M. Tyner, R. I. MacCuspie, T. J. Cho, M. R. Zachariah and V. A. Hackley, Langmuir **27** (6), 2464-2477 (2011).

110. K. Niikura, T. Matsunaga, T. Suzuki, S. Kobayashi, H. Yamaguchi, Y. Orba, A. Kawaguchi, H. Hasegawa, K. Kajino and T. Ninomiya, ACS Nano **7** (5), 3926-3938 (2013).

111. B. D. Chithrani, A. A. Ghazani and W. C. Chan, Nano Lett. **6** (4), 662-668 (2006).

112. H. Herd, N. Daum, A. T. Jones, H. Huwer, H. Ghandehari and C.-M. Lehr, ACS Nano **7** (3), 1961-1973 (2013).

113. R. Rigler, Ü. Mets, J. Widengren and P. Kask, Eur. Biophys. J. **22** (3), 169-175 (1993).

114. A. Michelman-Ribeiro, F. Horkay, R. Nossal and H. Boukari, Biomacromolecules **8** (5), 1595-1600 (2007).

115. G. J. Brownsey, T. R. Noel, R. Parker and S. G. Ring, Biophys. J. **85** (6), 3943-3950 (2003).

116. S. H. Brewer, W. R. Glomm, M. C. Johnson, M. K. Knag and S. Franzen, Langmuir **21** (20), 9303-9307 (2005).

117. S. Alam and A. Mukhopadhyay, Langmuir (2015) (In print).

118. W. S. Kuo, C. N. Chang, Y. T. Chang, M. H. Yang, Y. H. Chien, S. J. Chen and C. S. Yeh, Angew. Chem.-Ger. Edit **122** (15), 2771-2775 (2010).

119. F. MacKintosh and C. Schmidt, Curr. Opin. Colloid In. **4** (4), 300-307 (1999).

120. G. D. Phillies and K. A. Streletzky, *Recent research developments in physical chemistry*, 269-285 (2001).

121. T. Gisler and D. A. Weitz, Curr. Opin. Colloid In. **3** (6), 586-592 (1998).

122. M. Doi and S. F. Edwards, *The theory of polymer dynamics*. (Oxford university press, 1988).

123. K. Zero and R. Pecora, Macromolecules **15** (1), 87-93 (1982).

124. Y. Mori, N. Ookubo, R. Hayakawa and Y. Wada, J. Polym. Sci. **20** (11), 2111-2124 (1982).

125. G. Szamel and K. S. Schweizer, J. Chem. Phys. **100** (4), 3127-3141 (1994).

126. M. Fixman, Phys. Rev. Lett. **54** (4), 337 (1985).

127. G. Marrucci and N. Grizzuti, J. Rheol. (1978-present) **27** (5), 433-450 (1983).

128. Y. Qiu, Y. Liu, L. Wang, L. Xu, R. Bai, Y. Ji, X. Wu, Y. Zhao, Y. Li and C. Chen, Biomaterials **31** (30), 7606-7619 (2010).

129. T. Liedl, S. Keller, F. C. Simmel, J. O. Rädler and W. J. Parak, Small **1** (10), 997-1003 (2005).

130. M. M. Tirado and J. G. de la Torre, J. Chem. Phys. **73** (4), 1986-1993 (1980).

131. I. Bitsanis, H. Davis and M. Tirrell, Macromolecules **21** (9), 2824-2835 (1988).

132. R. Pecora and J. Deutch, J. Chem. Phys. **83** (9), 4823-4824 (1985).

133. C. J. Orendorff, T. M. Alam, D. Y. Sasaki, B. C. Bunker and J. A. Voigt, ACS Nano **3** (4), 971-983 (2009).

134. R. A. Farrer, F. L. Butterfield, V. W. Chen and J. T. Fourkas, Nano Lett. **5** (6), 1139-1142 (2005).

135. P. K. Jain, I. H. El-Sayed and M. A. El-Sayed, Nano Today **2** (1), 18-29 (2007).

136. M. Lundqvist, J. Stigler, G. Elia, I. Lynch, T. Cedervall and K. A. Dawson, P. Natl. A. Sci. **105** (38), 14265-14270 (2008).

137. X. Shi, D. Li, J. Xie, S. Wang, Z. Wu and H. Chen, Chinese Sci. Bull. **57** (10), 1109-1115 (2012).

138. M. A. Dobrovolskaia, A. K. Patri, J. Zheng, J. D. Clogston, N. Ayub, P. Aggarwal, B. W. Neun, J. B. Hall and S. E. McNeil, Nanomed. Nanotechnol. **5** (2), 106-117 (2009).

139.   P. Aggarwal, J. B. Hall, C. B. McLeland, M. A. Dobrovolskaia and S. E. McNeil, Adv. Drug Deliver. Rev. **61** (6), 428-437 (2009).

140.   E. Casals, T. Pfaller, A. Duschl, G. J. Oostingh and V. Puntes, ACS Nano **4** (7), 3623-3632 (2010).

ABSTRACT

DYNAMICS OF ANISOTROPIC GOLD NANOPARTICLES IN SYNTHETIC AND BIOPOLYMER SOLUTIONS

by

SHARMINE ALAM

August 2015

Advisor: Dr. Ashis Mukhopadhyay

Major: Physics

Degree: Doctor of Philosophy

Soft matter is a subfield of condensed matter physics including systems such as polymers, colloids, amphiphiles and liquid crystals. Understanding their interaction and dynamics is essential for many interdisciplinary fields of study as well as important for technological advancements. We used gold nanorods (AuNRs) to investigate the length-scale dependent dynamics in semidilute polymer solutions, their conjugation and interaction with a protein bovine serum albumin (BSA), and the effect of shape anisotropy on the dynamics within a crowded solution of spheres. Multiphoton fluctuation correlation spectroscopy (MP-FCS) technique was used to investigate the translation and rotational diffusion of AuNRs. For polymer solutions, we determined the nanoviscosity experienced by the rods from the measured diffusion coefficient. Our results showed the importance of microscopic friction in determing the particle dynamics. In BSA solutions, we observed a submonolayer formation at the AuNRs surface, which indicates loss of protein native conformation. For rod – sphere mixture, our results

indicated significant diffusional anisotropy for translational motion, whereas the rotation of the rods closely followed the 'caging theory'.

AUTOBIOGRAPHICAL STATEMENT
SHARMINE ALAM

Education:

- 2010-2015, Wayne State University, Detroit, MI: Ph.D. in Condensed Matter Physics

- 2010-2013, Wayne State University, Detroit, MI: MS in Physics

- 2003-2008, University of Dhaka, Dhaka, Bangladesh: BS in Physics

Publications:

1. Sharmine Alam and Ashis Mukhopadhayay "Translational Anisotropy and Rotational Diffusion of Gold Nanorods in Colloidal Sphere Solutions", Langmuir, DOI: 10.1021/acs.langmuir.5b01682, (2015).

2. Sharmine Alam and Ashis Mukhopadhyay, "Conjugation of Gold Nanorods with Bovine Serum Albumin Protein", The Journal of Physical Chemistry C, 118 (47), 27459–27464 (2014).

3. Sharmine Alam and Ashis Mukhopadhyay, "Translational and Rotational Diffusions of Nanorods within Semidilute and Entangled Polymer Solutions", Macromolecules, 47 (19), 6919–6924 (2014).

4. Indermeet Kohli, Sharmine Alam, Bhavdeep Patel and Ashis Mukhopadhyay, "Interaction and Diffusion of Gold Nanoparticles in Bovine Serum Albumin Solutions", Applied Physics Letters, 102 (20), 203705 (2013).

Presentations:

1. Sharmine Alam, Indermeet Kohli and Ashis Mukhopadhyay "Dynamics of Nanoparticles in Semidilute Solution of Spheres/Polymers", 2015 Condensed Matter and Biophysics Seminar, Wayne State University, Detroit, Michigan (USA).

2. Sharmine Alam, Indermeet Kohli and Ashis Mukhopadhyay, "Contrasting Nanoparticles Diffusion in Synthetic and Biopolymer Solutions", 2015 American Physical Society (APS) Annual Meeting, San Antonio, Texas (USA).

3. Sharmine Alam, Christopher Grabowski, Rami Omari and Ashis Mukhopadhyay, "Critical Adsorption and Colloidal Interaction in Binary Liquid Mixtures", 2015 American Physical Society (APS) Annual Meeting, San Antonio, Texas (USA).

4. Sharmine Alam and Ashis Mukhopadhyay, "Diffusion of Gold Nanorods in Polymer Solutions", 2014 American Physical Society (APS) Ohio Section Meeting, Youngstown, Ohio (USA).

5. Sharmine Alam, Indermeet Kohli, Bhavdeep Patel and Ashis Mukhopadhyay, "Adsorption of Gold Nanoparticles from a Crowded Solution on Solid/Liquid Interface", 2012 American Physical Society (APS) Ohio Section Meeting, Detroit, Michigan (USA).